



**UCGE Reports
Number 20314**

Department of Geomatics Engineering

**Performance Evaluation of GPS L1/L2 Positioning
with Partial Availability of the L2C Signals**

(URL: <http://www.geomatics.ucalgary.ca/graduatetheses>)

by

Da Wang

September 2010



THE UNIVERSITY OF CALGARY

**Performance Evaluation of GPS L1/L2 Positioning with
Partial Availability of the L2C Signals**

by

Da Wang

A THESIS

**SUBMITTED TO THE FACULTY OF GRADUATE STUDIES
IN PARTIAL FULFILLMENT OF THE REQUIREMENTS FOR THE
DEGREE OF MASTER OF SCIENCE**

DEPARTMENT OF GEOMATICS ENGINEERING

CALGARY, ALBERTA

September, 2010

© Da Wang 2010

PREFACE

This is an unaltered version of the authors Master of Science thesis. The thesis was accepted by the Faculty of Graduate Studies in September, 2010. The faculty supervisor for this work was Dr. Kyle O'Keefe. Other members of the examining committee were Dr. Gerard Lachapelle, Dr. Susan Skone, and Dr. Michel Fattouche.

ABSTRACT

The ongoing Global Positioning System (GPS) modernization program has seen the deployment of a partial constellation of Block IIR-M or Block IIF satellites capable of transmitting the new L2C signal. There is great benefit for the low-cost civil receivers to generate L2C measurements on a second frequency in addition to the full availability of L1 C/A signals, without the need to rely on the complicated and expensive tracking techniques to get access to the L2P measurements. The L2C signal is targeted to serve the current and future increasing demand of dual-frequency civil users, not only in the highly professional but also in the low-cost commercial electronic applications. Moreover, once the full deployment of the L2C signal is achieved in the future, it tends to serve the single-frequency GPS applications with the designed advantages over the L1 C/A signal.

This research investigated the feasibility of utilizing the partial availability of new L2C signals during its deployment phase for the single-point dual-frequency code positioning and differential GPS (DGPS) dual-frequency precise positioning with single baseline scenarios . For the single-point positioning scenario, an ionospheric delay estimation method using partial availability of L2C signals is proposed to provide ionospheric correction for the other L1 C/A single-frequency satellites. The resulted position accuracy is of the same order of magnitude as that obtained using the broadcast Klobuchar ionosphere model. For the DGPS dual-frequency precise positioning scenario, the L2C code and phase measurements are incorporated into the positioning filter and a single

state is added to account for the ionospheric residual using limited number of 1, 2, or 3 L2C measurements. The impact of the introduction of the L2C DD ambiguity on the ambiguity resolution (AR) performance is evaluated. The effectiveness of the proposed ionospheric residual estimation method as well as its impact of on the position accuracy and AR performance is also evaluated. The results show that partially available dual-frequency AR outperforms the L1 single-frequency AR. Moreover, a general conclusion is drawn that the more L2C satellites the better AR performance and better ionospheric residual estimate which leads to better position accuracy.

ACKNOWLEDGEMENTS

I would like to thank and express my gratitude firstly to my supervisor, Dr. Kyle O’Keefe, for his teaching, guidance, and support in my research study to make this work possible, and for his kind help in my life on campus. I would like also thank Dr. Gerard Lachapelle for him to give me the life-changing opportunity to further my study in the University of Calgary and enjoy the two years life in Calgary.

The acknowledge also goes to the other two examining committee members, Dr. Susan Skone and Dr. Michel Fattouche for their time to review the work.

Great thank goes to Tao Li for leading me into the GNSS positioning and navigation world and being my best friend with kind-hearted support anytime. I also appreciate Dr. Mark Petovello, Dr. Danielle Borio, Dr. Cillian O’Driscoll, Debo Sun, Tao Lin, Peng Xie, Zhe He, and Ping Luo for the help with discussions and problem solving, and Martin Ma for his review and grammar revising work of my thesis. My landlord Winnie Liu and her family are greatly acknowledged for helping me go through the first severe winter with a broken ankle.

Most importantly, the sincere gratitude and thanks go to my beloved parents and dear little sister. Their unselfish support, understanding, and love are my priceless life fortune.

Finally, the financial support from General Motors of Canada is acknowledged.

TABLE OF CONTENTS

PREFACE	ii
ABSTRACT	iii
ACKNOWLEDGEMENTS	v
TABLE OF CONTENTS	vi
LIST OF TABLES	ix
LIST OF FIGURES	x
NOTATIONS	xii
CHAPTER ONE: INTRODUCTION	1
1.1 MODERNIZATION BACKGROUND	2
1.2 RELATED RESEARCH	3
1.3 OBJECTIVES	6
1.4 THESIS OUTLINE.....	7
CHAPTER TWO: GPS L1 AND L2 SIGNALS, OBSERVATIONS, AND ERRORS	9
2.1 L1 AND L2 SIGNALS	9
2.1.1 <i>Signal Structures</i>	9
2.1.2 <i>Signal Processing and L2C Signal Performance</i>	12
2.2 OBSERVATION MODELS.....	14
2.2.1 <i>Principal Observation Models</i>	14
2.2.2 <i>Differencing Observations</i>	16
2.3 OBSERVATION ERRORS AND MODELING	18

2.3.1 Satellite Orbital Error	19
2.3.2 Satellite Clock Error and IFBs	20
2.3.3 Ionospheric Delay.....	22
2.3.4 Tropospheric Delay	30
2.3.5 Multipath.....	32
2.3.6 Receiver clock error and IFB.....	33
2.3.7 Receiver Noise	33
2.4 SUMMARY	34
CHAPTER THREE: L1 AND L2C SINGLE-POINT POSITIONING AND DGPS DUAL-	
FREQUENCY PRECISE POSITIONING	35
3.1 POSITION ESTIMATORS	35
3.1.1 Least Squares Adjustment	35
3.1.2 Kalman Filter.....	39
3.1.3 Applications in GPS Positioning.....	43
3.2 SINGLE-POINT CODE POSITIONING	44
3.3 DIFFERENTIAL CARRIER PHASE POSITIONING	46
3.3.1 Functional Models	46
3.3.2 Dynamic Models	47
3.3.3 Sequential EKF Implementation	51
3.3.4 Float DD Solution from Differencing the SD Solution	52
3.4 AMBIGUITY RESOLUTION	53
3.4.1 Ambiguity Estimation.....	54
3.4.2 Ambiguity Validation	55
3.4.3 Fixed Solution.....	57
3.4.4 L1 and L2 Dual-frequency Ambiguity Resolution.....	58
3.5 IONOSPHERIC DELAY ESTIMATION WITH PARTIAL AVAILABILITY OF L2C MEASUREMENTS	59
3.5.1 Smoothing and IFB Determination.....	61

3.5.2 <i>Single-point ZID Method</i>	64
3.5.3 <i>Differential ZID Method</i>	65
3.6 SUMMARY	69
CHAPTER FOUR: TESTING RESULTS AND ANALYSIS OF SINGLE-POINT CODE	
POSITIONING	71
4.1 DATA COLLECTION	71
4.2 IONOSPHERIC DELAY ESTIMATION RESULTS	73
4.3 SINGLE-POINT L1 C/A CODE POSITIONING RESULTS	78
4.4 SUMMARY	89
CHAPTER FIVE: TESTING RESULTS AND ANALYSIS OF CARRIER PHASE DGPS PRECISE	
POSITIONING	90
5.1 DATA COLLECTION	90
5.2 DATA PROCESSING AND RESULTS INTERPRETATION STRATEGIES	92
5.3 RESULTS AND ANALYSIS	95
5.3.1 <i>Scenario with L1 Only</i>	95
5.3.2 <i>Scenario with L2P Measurements</i>	102
5.3.3 <i>Scenarios with partial availability of L2C satellites</i>	111
5.4 SUMMARY	129
CHAPTER 6: CONCLUSIONS AND RECOMMENDATIONS	130
REFERENCES	135

LIST OF TABLES

Table 2.1: Basic L1 and L2 Linear Phase Combinations	18
Table 4.1: RMS position errors for post-processing of the first data set.....	82
Table 4.2: RMS position errors for real-time processing of the first data set.....	85
Table 4.3: RMS position errors for real-time processing of the second data set	89
Table 5.1: Selected baselines.....	91
Table 5.2: The whole dataset position error RMS and AR performance for L1 Only Strategy, short baseline	98
Table 5.3: Data batches AR performance, short baseline.....	98
Table 5.4: The whole data set position error RMS and AR performance, long baseline.....	101
Table 5.5: Data batches AR performance, long baseline.....	102
Table 5.6: The whole data set position error RMS and AR performance for Strategy A and Strategy C using L2P measurements, short baseline	106
Table 5.7: Data batches AR performance with Strategy A using L2P measurements, short baseline.....	106
Table 5.8: The whole data set position error RMS and AR performance for Strategy A and Strategy C using L2P measurements, long baseline.....	110
Table 5.9: Data batches AR performance with Strategy A using L2P measurements, long baseline.....	110
Table 5.10: The whole dataset position error RMS and AR performance with 1 L2C satellite available, short baseline	116
Table 5.11: The whole dataset position error RMS and AR performance with 1 L2C satellite available, long baseline	119
Table 5.12: The whole dataset position error RMS and AR performance with 2 L2C satellites available, short baseline	120
Table 5.13: Data batches AR performance with 2 L2C satellites (PRN 29 & 05) available, short baseline	121
Table 5.14: The whole dataset position error RMS and AR performance with 2 L2C satellites available, long baseline	123
Table 5.15: Data batches AR performance with 2 L2C satellites (PRN 29 & 05) available, long baseline	123
Table 5.16: The whole dataset position error RMS and AR performance with 3 L2C satellites available, short baseline	124
Table 5.17: Data batches AR performance with 3 L2C satellites available, short baseline	125
Table 5.18: The whole dataset position error RMS and AR performance with 3 L2C satellites available, long baseline	128
Table 5.19: Data batches AR performance with 3 L2C satellites available, long baseline	128

LIST OF FIGURES

Figure 2.1: Ionosphere single-layer model	27
Figure 3.1: SLM based differential ZID estimation method	68
Figure 4.1: Satellites sky plot for the first data set	72
Figure 4.2: Elevation angle for the three available L2C satellites	72
Figure 4.3: Example of the ionospheric group delay and ambiguous phase advance.....	74
Figure 4.4: Batch smoothed L1 slant ionospheric delay without inter-frequency bias compensated	75
Figure 4.5: Mapped zenith ionospheric delay from batch smoothed slant ionospheric delay without inter-frequency biases corrected.....	76
Figure 4.6: Batch smoothed slant ionospheric delays with inter-frequency biases corrected.....	77
Figure 4.7: Mapped zenith ionospheric delay from inter-frequency biases corrected slant ionospheric delays, with the zenith delays from the batch least-square estimate and the Klobuchar ionosphere model	77
Figure 4.8: Positioning errors using L1 C/A pseudoranges without ionospheric delay being corrected.....	79
Figure 4.9: Positioning errors using ionospheric corrections from Klobuchar model.....	80
Figure 4.10: Position errors using a zenith value obtained from averaging of the ZID estimates from 3 L2C satellite (PRN 7, 15 , and 17).....	80
Figure 4.11: Position errors using a zenith value obtained from averaging 2 L2C satellite (PRN 7 and 17) estimated zenith values	81
Figure 4.12: Position errors using the estimated zenith delay obtained from 1 L2C satellite (PRN 7).....	81
Figure 4.13: Recursive smoothed slant ionospheric delays with the inter-frequency biases corrected for the first data set.....	84
Figure 4.14: Mapped zenith ionospheric delays from the slant ionospheric delays shown in Figure 4.13....	85
Figure 4.15: The elevation angles of the 3 L2C satellites in the second data set	86
Figure 4.16: Recursive carrier smoothed slant ionospheric delays for the second dataset corrected with the inter-frequency biases obtained from the first dataset	87
Figure 4.17: Mapped zenith ionospheric delays from the slant ionospheric delays shown in Figure 4.16....	87
Figure 5.1: The geography locations of the three selected stations as part of the Western Canada Deformation Array (NRCan 2010)	91
Figure 5.2: Sky plot for BAMF station.....	92
Figure 5.3: Estimated L1 float DD ambiguity of PRN 29 – PRN 30 for L1 Only Strategy, short baseline ..	96
Figure 5.4: Ambiguity validation test values for L1 Only Strategy, short baseline	96
Figure 5.5: Position errors for L1 Only Strategy, short baseline	97
Figure 5.6: Estimated L1 float DD ambiguity of PRN 29 – PRN 30 for L1 Only Strategy, long baseline .	100
Figure 5.7: Ambiguity validation test values for L1 Only Strategy, long baseline	100
Figure 5.8: Position errors for L1 Only Strategy with and without Klobuchar model, long baseline	101

Figure 5.9: Estimated L1 float DD ambiguity of PRN 29 – PRN 30 for Strategy A and Strategy C using L2P measurements, short baseline	104
Figure 5.10: Ambiguity validation test values for Strategy A and Strategy C using L2P measurements, short baseline	104
Figure 5.11: Position errors for Strategy A and Strategy C using L2P measurements, short baseline	105
Figure 5.12: Estimated L1 float DD ambiguity of PRN 29 – PRN 30 for Strategy A and Strategy C using L2P measurements, long baseline	108
Figure 5.13: Ambiguity validation test values for Strategy A and Strategy C using L2P measurements, long baseline	108
Figure 5.14: Position errors for Strategy A and Strategy C using L2P measurements, long baseline	109
Figure 5.15: Estimated differential ZID from IONEX map and Strategy B with 1, 2, or 3 L2C satellites available, short baseline	112
Figure 5.16: Estimated differential ZID from IONEX map and Strategy B with 1, 2, or 3 L2C satellites available, long baseline	112
Figure 5.17: Estimated L1 float DD ambiguity of PRN 29 – PRN 30 for Strategy A and B with 1 L2C satellite (PRN 29) available, short baseline	114
Figure 5.18: Ambiguity validation test values for Strategy A and Strategy B with 1 L2C satellite (PRN 29) available, short baseline	114
Figure 5.19: Position errors for Strategy A and B with 1 L2C satellite (PRN 29) available, short baseline	115
Figure 5.20: Estimated L1 float DD ambiguity of PRN 29 – PRN 30 for Strategy A and B with 1 L2C satellite (PRN 29) available, long baseline	117
Figure 5.21: Ambiguity validation test values for Strategy A and Strategy B with 1 L2C satellite (PRN 29) available, long baseline	117
Figure 5.22: Position errors and number of fixed ambiguities, Strategy A and B with 1 L2C satellite (PRN 29) available, long baseline	118
Figure 5.23: Ambiguity validation test values for Strategy A and Strategy B with 2 L2C satellite (PRN 29 & 5) available, long baseline	121
Figure 5.24: Position errors and number of fixed ambiguities, Strategy A and B with 2 L2C satellites (PRN 29 & 5) available, long baseline	122
Figure 5.25: Ambiguity validation test values for Strategy A and Strategy B with 3 L2C satellites available, long baseline	127
Figure 5.26: Position errors, Strategy A and B with 3 L2C satellites available, long baseline	127

NOTATIONS

List of Symbols

$\hat{\mathbf{a}}$	float ambiguities vector
$\tilde{\mathbf{a}}$	fixed ambiguities vector
\mathbf{A}	LSQ design matrix
$\hat{\mathbf{b}}$	float solution vector for the non-ambiguity states
$\tilde{\mathbf{b}}$	fixed solution vector for the non-ambiguity states
b	baseline length
b_{ρ}^R	receiver IFB in the code measurements
b_{ϕ}^R	receiver IFB in the carrier phase measurements
b_{ρ}^S	satellite IFB in the code measurements
b_{ϕ}^S	satellite IFB in the carrier phase measurements
c	speed of light
dt	satellite clock error
dT	receiver clock error
$d\tau$	time delay
e	satellite elevation angle
\mathbf{F}	system dynamic matrix
f_1	L1 carrier frequency
f_2	L2 carrier frequency
\mathbf{G}	shaping matrix
\mathbf{h}	row vector of the KF design matrix
\mathbf{H}	KF design matrix
h_I	the height of the ionosphere shell
I_{ρ}^s	slant ionospheric code delay on L1
I_{ϕ}^s	slant ionospheric phase advance on L1
\mathbf{K}	Kalman gain matrix
\mathbf{l}	LSQ observation vector
l	signal path
m	ionosphere mapping function
m_{ρ}	code multipath
m_{ϕ}	carrier phase multipath
n	refractive index
N_1	L1 DD ambiguity
N_2	L2 DD ambiguity
\mathbf{P}	covariance matrix
\mathbf{Q}	process noise matrix

q	system state spectral density
\mathbf{r}	LSQ residual vector
\mathbf{R}	measurements covariance matrix
r_E	Earth's radius
t	GPS time
t_{sv}	signal transmission time in the satellite clock
T_{GD}	group delay
T_s	tropospheric delay
\mathbf{v}	KF residual vector
v	velocity
\mathbf{x}	states nominal vector
$\hat{\mathbf{x}}$	states estimate vector
x, y, z	ECEF coordinates
x^s, y^s, z^s	ECEF coordinates of the satellite
\mathbf{z}	KF observation vector
\mathbf{w}	white Gaussian noise vector
ρ	pseudorange measurement
ρ_0	geometrical range between receiver and satellite
$\bar{\rho}_0$	the mean geometrical range between receiver and satellite
ϕ	carrier phase measurement
λ	carrier wavelength
σ	measurement standard deviation
ω	misclosure vector
Φ	transition matrix
Ψ	normal distribution cumulative function
Γ	noise driven matrix
ε_ρ	code noise
ε_ϕ	carrier phase noise
γ	frequency squared ratio
θ	receiver's zenith angle
θ'	satellite's zenith angle
δb	baseline error
δt	time difference between observation epochs
$\delta \mathbf{x}$	states estimation error
$\delta \rho_0$	satellite orbital error
Δ	between-receiver differencing operator
∇	between-satellite differencing operator
$\Delta \nabla$	double differencing operator
$\ \cdot\ $	Euclidean vector norm

List of Abbreviations and Acronyms

AR	Ambiguity Resolution
BPSK	Binary Phase Shift Keying
Coarse/Acquisition	C/A
C/N_0	Carrier-to-Noise density
CDMA	Code Division Multiple Access
CNAV	Civil NAVigation data
DD	Double Difference
DGPS	Differential GPS
GIM	Global Ionosphere Map
GNSS	Global Navigation Satellite System
GPS	Global Positioning System
IEEE	Institute of Electrical and Electronics Engineers
IFB	Inter-Frequency Bias
ISC	inter-signal correction
LAMBDA	Least-squares AMbiguity Decorrelation Adjustment
LSQ	Least-squares
NL	Narrowlane
KF	Kalman Filter
LOS	Line-Of-Sight
PCF	Percentage of Correct Fixing
PIF	Percentage of incorrect Fixing
PNT	Positioning, Navigation, and Timing
ppm	parts-per-million
PRN	Pseudo-Random Noise
QPSK	Quadrature Phase Shift Keying
RF	Radio Frequency
RMS	root-mean-square
SD	Single Difference
SID	Slant Ionospheric Delay
SLM	Single-Layer Model
SNR	Signal-to-Noise Ratio
SPS	Standard Positioning Service
SR	Success Rate
STEC	Slant TEC
TEC	Total Electron Content
TECU	TEC Unit
UD	Un-Differenced
UHF	Ultra-High Frequency
VTEC	Vertical TEC
WL	Widelane
ZID	Zenith Ionospheric Delay

CHAPTER ONE: INTRODUCTION

As the first passive, one-way ranging Global Navigation Satellite Systems (GNSS) to become operational, the GPS is an all-weather positioning and navigation system developed and maintained by the U.S. Department of Defense primarily for military applications. However, it has been serving worldwide civilian users since its fully operational capability was declared after its civil signals are open to the public and the later removal of the selective availability by the U.S. government. Everyone in the world with a civil GPS receiver can determine accurate time and location, in any weather, any time, and anywhere.

A constellation of 24 satellites for the GPS system design are in six orbital planes inclined at 55 degrees relative to the equatorial plane at an altitude of about 20,200 km from the earth. This configuration ensures a global coverage with at least 4 satellites simultaneously observable. Usually six to eight satellites are available for a user anywhere on the earth. A key part of the GPS satellites is a very stable atomic clock from which all the satellites are synchronized and all ranging measurements are obtained. GPS provides standard positioning service (SPS) consisting of space-based positioning, navigation, and timing (PNT) signals (only refers to L1 C/A signal until now) delivered free of user fees for peaceful civil, commercial and scientific uses worldwide. As to 2007, with the signal-in-space accuracy, well-designed GPS civil receivers can achieve horizontal accuracy of 3 metres or better and vertical accuracy of 5 metres or better 95% of the time (Department of Defense 2008).

At present, for example, the GPS chip is planting into most of the handheld electronic devices for location service and is becoming a necessary part of an automobile for navigation purposes. The continuously developing semi-conductor and computing technologies enable the GPS into everyone's daily life which will substantially benefit from the GPS modernization for civil applications.

1.1 Modernization Background

Based on the benefit from the civil GPS applications with L1 only SPS, the civilian users are requiring more from this system to meet for high-value professional and commercial applications, e.g. dual-frequency applications for precise positioning on machine guidance, infrastructure monitoring, and land surveying, and so on. However, these applications are limited by the only present single civil signal on frequency L1, although the civilian users turn to the encrypted signal on the second frequency using certain advanced tracking techniques. Thus, there is a growing demand to place a civil signal on the second frequency. The GPS modernization is therefore focusing on adding new frequency carriers and civil signals to the GPS constellation. Besides, another drive to motivate the modernization is that the competition from other developing GNSS, i.e. GLONASS in Russia, Galileo in Europe, and Compass/Beidou in China. These systems emphasize civilian services with multiple signals at their very early design stages to meet the requirements in a growing world. Finally, there is inherent limitation of the legacy civil signal on L1 frequency, i.e. L1 Coarse/Acquisition (C/A) signal, has substantial degraded performance during particular harsh environments, such as signal attenuation

under foliage or in urban canyons, signal interference, and multipath sensitive location.

The design of the new civil signals is expected to overcome these shortcomings.

There are three announced modernized signals designed for civilian use: a) L2C signal on L2 frequency, for commercial dual-frequency applications enabling ionospheric correction along with L1 C/A signal in a low-cost civil receiver, and for delivery of faster signal acquisition, enhanced availability and reliability in single-frequency applications; b) L5 civil signal, located in the frequency band reserved for aviation safety applications; c) L1C signal on L1 frequency, the fourth civil signal designed to enable interoperability between GPS and other GNSS systems expected to provide better performance. The new signals are phasing in gradually as new GPS satellites are launched to replace the older ones. As the time of writing, the first GPS Block IIF satellite with full L5 capability has been launched on May 28, 2010. The eighth GPS Block IIR-M satellite (referring to the L2C satellite in this thesis) with full L2C capability was launched on August 17, 2009 and was set operational ten days later, which is known by its pseudorandom noise number (PRN) as PRN 05. Starting with the first Block IIR-M satellite, PRN 17, with full L2C capability launched on September 26, 2005, there are currently another six satellites transmitting L2C signals, i.e. PRN 01 (also with testing L5 capability), PRN 07, PRN 12, PRN 15, PRN 29, and PRN 31, seven L2C satellites in all.

1.2 Related Research

There are convincing advantages of having GPS measurements generated on a second frequency in addition to the legacy L1 frequency. With the availability of dual-frequency

measurements, there comes the great opportunity to explore the ionosphere property and to model the ionosphere effect on positioning. Moreover, dual-frequency AR plays an important role in relative precise positioning, e.g. for survey applications.

A user can essentially eliminate the ionosphere as a source of GPS measurement error with a dual-frequency (e.g. L1 and L2) receiver estimating the ionospheric group delay and phase advance (Misra & Enge 2001). However, the estimate of the ionospheric delay using the coding measurements is noisy, which subjects to the relatively large code multipath and noise, and the derived estimate using the phase measurements alone is precise but inherent ambiguous with the presence of the unknown integer ambiguities. Therefore, data smoothing techniques are employed to take advantage of both the code and phase estimates in order to account for the ionospheric delay with better accuracy (Hatch 1982, Lachapelle et al 1986, Skone 1998). Liu et al (2005) compared the performance of two smoothing approaches and derived closed-form ionospheric delay estimation formulas, which provides guidance for the selection of the smoothing approach for different scenarios.

In addition, the ionospheric delay estimate obtained from dual-frequency measurements is subject to the inter-frequency bias (IFB) at both the receiver and satellite ends as well. The determination of the IFB is important for precise ionosphere modeling, and currently this has been fulfilled mostly using the ionosphere single-layer model (SLM) assumption. (Gao et al 1994). A new and efficient algorithm is proposed in Hong (2007) using the geometry conditions between the satellites and the receivers without the need for the

ionosphere SLM assumption, which makes the IFB estimation independent on the ionosphere model.

The carrier phase based DGPS precise positioning relies on the correct resolution of the double difference (DD) integer ambiguities in the DD phase measurements to achieve centimetre or millimetre level of accuracy. The Least-square AMbiguity Decorrelation Adjustment (LAMBDA) method is a very well-known mechanization of the integer least-square (LSQ) ambiguity estimation (Teunissen, 1995) and is being well documented and widely used. This method proposed an efficient algorithm that is independent of the GNSS systems, frequencies, and the number of carriers, comparing to the other integer ambiguity estimation approaches. The accuracy of the carrier phase based DGPS precise positioning is affected by primarily the differential tropospheric delay and differential ionospheric error which is difficult to be well modelled (Klobuchar 1996).

With the L1 and L2 dual-frequency measurements, measurement combinations are used to either mitigate, e.g. forming ionosphere-free observable, or to account for, e.g. forming widelane (WL) observable, the ionospheric errors (Hatch 1982, Blewitt 1989). Alternatively, however of particular interest is the stochastic modeling of the differential ionospheric residual, which is proposed in Teunissen (1997). Further, depends on the a-priori knowledge of the ionospheric error, Odijk (2002, 2000) summarized a class of three models, i.e. the ionosphere-fixed, float, and weighted model, to estimate the differential ionospheric error explicitly. Note that external ionospheric error information is indispensable for the ionosphere-fixed and ionosphere-weighted models. In Liu et al

(2003), a thorough investigation of the carrier phase combination strategies using L1 and L2 dual-frequency measurements was performed. The “0” values are adopted as the pseudo-observations of the DD ionospheric residuals which are usually bounded around zero. These strategies are assessed and compared using real world data from short, medium, long baselines.

1.3 Objectives

Having so much work been done in the literature for GPS civil applications using L1 C/A and L2P dual-frequency measurements, this research work is to demonstrate the feasibility of employing the partial constellation of L2C signals to replace the full constellation of L2P signals for dual-frequency processing on ionospheric error estimation and AR. The following specific objectives are set up to guide this thesis work:

- a) To design an ionospheric delay estimation algorithm for the single-point L1 C/A code positioning with full constellation of L1 C/A signals and only partial constellation of L2C signals.
- b) To design and implement a strategy to estimate the differential ionospheric errors for all the involved L1 C/A and L2C code and phase measurements utilizing the limited number of L2C measurements from the available L2C satellites in a single difference (SD) observation model based carrier phase processor.
- c) To test the AR performance of the scenarios L1 C/A only single-frequency, L1 C/A and L2P dual-frequency, and L1 C/A and L2C dual-frequency.

- d) To evaluate the effectiveness of the designed ionospheric error estimation algorithms and to test their impact on positioning accuracy and single- or dual-frequency AR performance using real world data.

1.4 Thesis Outline

This thesis includes six chapters in all. The organization of the content of the remaining part is briefed for each chapter.

Chapter Two reviews the L1 C/A and the L2P signals and corresponding performance. The L2C signal is introduced in terms of the design motivation and features, the signal characteristics, and the advantage over the L2P signal for civil applications. The L1 and L2 observation models used in this work are reviewed. An overview of the measurement and observable error sources is provided with brief discussions of the countermeasures.

Chapter Three reviews concepts on the single-point code positioning and carrier phase DGPS precise positioning, including the functional models, system dynamic models, and the LAMBDA method for AR. The LSQ and Kalman filter (KF) estimators are reviewed along with the positioning concepts. Two algorithms are proposed to estimate the L1 C/A ionospheric code delay for single-point code positioning, and the differential L1 C/A and L2C ionospheric code and phase advance for DGPS precise positioning utilizing the partial constellation of L2C signals.

Chapter Four tests the proposed single zenith ionospheric delay (ZID) algorithm for ionospheric delay estimation in a single-point code positioning scenario using real data. Two tests are performed on two data sets with three L2C satellites available. One is a post-processing test with batch smoothing approach to estimate the ionospheric delays as well as the receiver IFB. The other is a real-time processing test with recursive smoothing approach to estimate the ionospheric delays. Performance evaluation is fulfilled in terms of single-point positioning accuracy.

Chapter Five tests the proposed differential ZID method is tested using real data in a relative positioning scenario with short and long baselines. A SD observation model based carrier phase positioning KF is implemented estimating the differential ionospheric errors along with the position states, the SD clock bias state, and the SD ambiguity states. The positioning accuracy and AR performance are compared among different scenarios for evaluation.

Chapter Six draws principle conclusions based on the presented results and makes recommendations for future work development and evaluation.

CHAPTER TWO: GPS L1 AND L2 SIGNALS, OBSERVATIONS, AND ERRORS

This chapter briefly reviews the GPS L1 and L2 signal structures, their signal performances, and their derived observations. The design motivation and technical characteristics of the L2C signal are especially of interest. The observation models for L1 and L2 dual-frequency processing used in this work are presented as well as the observation errors and the corresponding methods to account for them.

2.1 L1 and L2 Signals

The GPS satellites are transmitting the signals with the radio frequency (RF) located in the L-band which is a subset of the ultra-high frequency (UHF) band that covers the frequencies between 1 GHz and 2GHz. The Link 1 (L1) and Link 2 (L2) are known as the legacy GPS signal carrier frequencies that have been in use since the system was deployed. Actually, the GPS satellites transmit additional RF signals referred to as Link 3 (L3) and Link 4 (L4), which are generated by classified payloads aboard the satellites, for classified or military purposes serving the U.S. Department of Defense (Misra & Enge 2001). The ongoing GPS modernization introduces the additional Link 5 (L5) signal for civil and especially safety-of-life applications. In the remaining part of this section, only the L1 and L2 signals will be reviewed and discussed for the purpose of this work.

2.1.1 Signal Structures

The GPS is a Code Division Multiple Access (CDMA) system. Generally, each GPS signal is comprised of three components: the RF carrier, the PRN code, and the

navigation data bits carrying the navigation messages. The satellites share the same frequencies but their signals can be discriminated from each other with different PRN codes modulated on the carrier with various modulation techniques, e.g. binary phase shift keying (BPSK) and Quadrature phase shift keying (QPSK).

The L1 signal is centered at the RF frequency of 1575.42 MHz (f_1) carrying the coarse/acquisition (C/A) code, the precision (P) code, and the navigation message using the BPSK modulation technique, as well as the navigation data message. The P code is classified for military use and has been encrypted by the Y-code since 1994. The encrypted code is therefore referred to as the P(Y) code in general. The P(Y) code is designed as the principle code for precise ranging with a code period of 7 days at a chipping rate of 10.23 Mbps. The much shorter C/A code is designed to aid the acquisition of the long P(Y) code with a code period of only 1 millisecond (ms) at a chipping rate of 1.023 MHz. Each satellite is assigned with a unique C/A code selected from the Gold code family, and the Gold code is generated by the modulo-2 addition of two maximum-length sequence (m-sequence) with the same period. The C/A code is open to the public but the precision of the C/A code ranging is limited. Positioning using only the C/A code pseudoranges is referred to as SPS. A binary data bit rate of 50 bps is used to carry the navigation message, which is modulated with the C/A code and then with the carrier. Due to the alignment of the C/A code and navigation data bit boundaries, there are exactly 20 C/A code periods during one data bit.

The L2 signal is centered at the frequency of 1227.60 MHz (f_2). Before GPS modernization, L2 carried only the P(Y) code. In addition to single-frequency (L1) applications, however the dual-frequency applications require phase tracking and measurements on L2. Since the spreading code is not known, the codeless tracking and the semi-codeless tracking techniques are used to generate measurements on L2, e.g. squaring method and cross-correlation method, are used to generate measurements on L2; however, are usually subject to loss of signal-to-noise ratio (SNR) and non-robust tracking (Woo 1999).

In order to eliminate the need to track the L2 P(Y) signal to obtain measurements on L2, and instead of having a replica of the C/A code on L2 for civilian use, a modern signal structure designed to meet the requirements and capabilities in the 21st century, was introduced to serve not only the dual-frequency applications but also the single-frequency applications which are currently using the L1 C/A signal (Fontana et. al. 2001).

Similar to the C/A code and the P(Y) code on L1, the civil code on L2 (L2C) is modulated on the in-phase carrier and is synchronized to the satellite clock, while the L2 P(Y) code is modulated on the quadrature carrier, which has a 90° phase shift to its in-phase counterpart. The modern L2C signal structure incorporates a dataless channel (the pilot channel) in addition to the data channel carrying navigation message in binary data bits. The two channels carry two different types of codes, i.e. the L2 civil-moderate (L2CM) code on the data channel and the L2 civil-long (L2CL) code on the pilot channel. The L2CM code is different for each satellite with a chipping rate of 511.5 kbps and a

period of 20 ms, i.e. 10230 chips, while the L2CL code is much longer than the L2CM code with 767250 chips at the same chipping rate and a period of 1.5 seconds. The two codes are transmitted in the same single frequency carrier in a chip-by-chip, time-multiplex manner. Thus the actual chipping rate of the time multiplexed code is 1.023 MHz, which is the same as the L1 C/A code. Besides, the L2CM code is aligned with the data bit, which eliminates the need to perform the data bit synchronization once the signal is acquired. A newly updated civil navigation (CNAV) data is modulated on the L2CM code. The CNAV data is intended for the GPS modernized civil signals and has a flexible structure for frames, which was not available for the navigation (NAV) data modulated on the L1 C/A signal. The CNAV data has a bit rate of 25 bps but is coded by a rate $\frac{1}{2}$ convolution encoder that provides a 50 symbol-per-second symbol rate. The convolution coding method is adopted to reduce the bit error rate when extracting the data bit. The CNAV data has been uploaded to the modernized Block IIR-M (also for the future modern GPS satellites) satellites since September 2009.

2.1.2 Signal Processing and L2C Signal Performance

Driving by the requirements of dual-frequency and more robust single-frequency applications, the L2C signal has a modern two channels design. As a result, the available transmission power is equally distributed between the data and pilot channels, which lead to a 3 dB signal power reduction for each individual channel. However, the tracking of a dataless channel provides a 6 dB threshold advantage, which overall mitigates the above mentioned 3 dB signal power loss and gains a 3 dB carrier phase tracking improvement when compared to the single-channel L1 C/A signal tracking. This advantage is very

useful for weak signal tracking in signal degraded environments. Besides, there is an unacceptable 21 dB (Doppler effects included) cross-correlation inherent to the C/A code that allows a strong GPS signal to interfere with the weak GPS signals. The L2C signal theoretically achieves this by having a worst-case cross-correlation performance of 45 dB (Fontana et al 2001). Moreover, the L2C signal design lowers the data modulation threshold and makes it possible to decode the message with even barely tracked signals. These advantages benefit the single-frequency signal processing and enhance the robustness of its applications. However, there are still limitations for a single-frequency L2C receiver. The minimum received signal power of the L2C signal on modern Block IIR-M or IIF satellites is -160.0 dBW, which is 1.5 dB lower than the L1 C/A signal transmitting from the same satellite (ICD-GPS-200D 2006). Fortunately, with the assistance of the pilot channel and the long L2C code, the processing signal power can be compensated to some extent. In addition, the dispersive ionosphere causes the ionospheric error proportional to the square of the carrier frequency. The L2 frequency is lower than the L1 frequency, which results in greater ionospheric error in the L2 measurements than those in the L1 measurements. This is a disadvantage for the single-frequency L2C receivers. Therefore, it is recommended to use a L1/L2 dual-frequency receiver to effectively remove the ionospheric errors, which has been demonstrated in experiments using real data.

Several real data experiments have been conducted to investigate the L2C signal performance using different receivers from different vendors after the first Block IIR-M satellite became operational. In summary, the L2C signal has similar code noise and

multipath level as those of the L1 C/A signal, but the inclusion of the pilot channel of the L2C signal surely helps the signal acquisition and phase tracking under signal degraded environments. Besides, the L2C signal outperforms the L2P(Y) signal in terms of carrier-to-noise density (C/N_0) and the carrier phase measurements quality (Simsky et al 2006, al-Fanek et al 2007, Sukeova et al 2007).

2.2 Observation Models

The principle GPS observations are the measurements of the line-of-sight (LOS) signal path between the satellites and the receiver. Three types of observables can be generated from each channel of the receiver, i.e. code pseudorange, carrier phase cycles, and Doppler, which are referred to as un-differenced (UD) observations. Based on the UD observations, the SD and DD observations can be formed either to reduce or eliminate some biases or errors.

2.2.1 Principal Observation Models

The principle observation models for the GPS L1 and L2 code and phase observables are defined as follows:

$$\begin{aligned}\rho_1 &= \rho_0 + \delta\rho_0 + c(dt - dT) + T_s + I_\rho^s - b_{\rho,1}^R + b_{\rho,1}^S + m_{\rho,1} + \varepsilon_{\rho,1} \\ \rho_2 &= \rho_0 + \delta\rho_0 + c(dt - dT) + T_s + \gamma I_\rho^s - b_{\rho,2}^R + b_{\rho,2}^S + m_{\rho,2} + \varepsilon_{\rho,2}\end{aligned}\quad (2.1)$$

and

$$\begin{aligned}\phi_1 &= \rho_0 + \delta\rho_0 + c(dt - dT) + \lambda_1 N_1 + T_s - I_\phi^s - b_{\phi,1}^R + b_{\phi,1}^S + m_{\phi,1} + \varepsilon_{\phi,1} \\ \phi_2 &= \rho_0 + \delta\rho_0 + c(dt - dT) + \lambda_2 N_2 + T_s - \gamma I_\phi^s - b_{\phi,2}^R + b_{\phi,2}^S + m_{\phi,2} + \varepsilon_{\phi,2}\end{aligned}\quad (2.2)$$

with

$$\gamma = (f_1/f_2)^2 \quad (2.3)$$

where the subscript 1 and 2 represent the frequencies f_1 and f_2 respectively and the superscripts R and S represent receiver and satellite respectively,

ρ_0 is the geometrical range between the receiver and satellite

$\delta\rho_0$ is the satellite orbital error,

c is the speed of light (299792458.0 m/s),

dt is the satellite clock error,

dT is the receiver clock error,

λ is the wavelength of the carrier,

N is the integer phase ambiguity,

T_s is the tropospheric error,

I_s^ρ is the slant ionospheric delay on L1,

I_s^ϕ is the slant ionospheric phase advance on L1,

b with subscript or superscript is the instrumental hardware delay,

m represents the multipath, and

ε represents the noise.

Note that these observation equations are defined specifically for L1 and L2 dual-frequency processing, which account for the IFBs (referring to section 2.3.6) between the L1 and L2 measurements. For single-frequency processing, the IFBs are not accounted

for and should be eliminated from the above observation equations. The principle observations are also referred to as UD observations.

2.2.2 Differencing Observations

Single-differenced (SD) Observation Models

The SD observations can be formed either from between-receiver differencing or from between-satellite differencing. The between-receiver L1 and L2 code and phase SD observations are of interest of this work and are obtained as follows by introducing a between receivers SD operator Δ

$$\begin{aligned}\Delta\rho_1 &= \Delta\rho_0 - c\Delta dT + \Delta T_s + \Delta I_\rho^s - \Delta b_{\rho,1}^R + \Delta\epsilon_{\rho,1} \\ \Delta\rho_2 &= \Delta\rho_0 - c\Delta dT + \Delta T_s + \gamma I_\rho^s - \Delta b_{\rho,2}^R + \Delta\epsilon_{\rho,2}\end{aligned}\tag{2.4}$$

and

$$\begin{aligned}\Delta\phi_1 &= \Delta\rho_0 - c\Delta dT + \lambda_1\Delta N_1 + \Delta T_s - \Delta I_\phi^s - \Delta b_{\phi,1}^R + \epsilon_{\Delta\phi,1} \\ \Delta\phi_2 &= \Delta\rho_0 - c\Delta dT + \lambda_2\Delta N_2 + \Delta T_s - \gamma\Delta I_\phi^s - \Delta b_{\phi,2}^R + \epsilon_{\Delta\phi,2}\end{aligned}\tag{2.5}$$

Note that the satellite clock error is eliminated as well as the IFB at the satellite end. The multipath and the satellite orbital error are omitted for simplicity since these errors are not modeled in the scope of this work. There are several advantages of the SD observation: a) mathematically uncorrelated, b) suitable for sequential update which is computationally efficient, c) innovation testing can be performed using an ordered strategy from the highest elevation satellite, and d) simple implementation compared to that for the DD observations.

Double-difference Observation Models

Based on the above SD observations, the DD observations can be formed through between-satellite differencing the between-receiver SD observations, which are described as follows by introducing the between-satellite SD operator ∇

$$\begin{aligned}\Delta\nabla\rho_1 &= \Delta\nabla\rho_0 + \Delta\nabla T_s + \Delta\nabla I_\rho^s + \varepsilon_{\Delta\nabla\rho} \\ \Delta\nabla\rho_2 &= \Delta\nabla\rho_0 + \Delta\nabla T_s + \gamma\Delta\nabla I_\rho^s + \varepsilon_{\Delta\nabla\rho}\end{aligned}\quad (2.6)$$

and

$$\begin{aligned}\Delta\nabla\phi_1 &= \Delta\nabla\rho_0 + \lambda_1\Delta\nabla N_1 + \Delta\nabla T_s - \Delta\nabla I_\phi^s + \varepsilon_{\Delta\nabla\phi} \\ \Delta\nabla\phi_2 &= \Delta\nabla\rho_0 + \lambda_2\Delta\nabla N_2 + \Delta\nabla T_s - \gamma\Delta\nabla I_\phi^s + \varepsilon_{\Delta\nabla\phi}\end{aligned}\quad (2.7)$$

Note that the satellite and receiver clock errors as well as the IFBs in the satellites and receivers are eliminated.

Observation Combinations

The L1 and L2 phase measurements can be linearly combined to obtain new measurements in a way described by the following equation (Lachapelle 2008)

$$\phi_{j,k} = j\phi_1 + k\phi_2 \quad (2.8)$$

The resulting wavelength is

$$\lambda_{j,k} = \frac{1}{j/\lambda_1 + k/\lambda_2} \quad (2.9)$$

Depending on the requirements of the GPS applications, e.g. time to fix ambiguity and positioning accuracy, different combinations of j and k are selected to form the phase combinations with different wavelengths and noise characteristics. There are significant advantages and disadvantages for each phase combination, which is chosen to

compromise the application requirements. Several typical phase combinations and associated characteristics are shown in Table 2.1 (Lachapelle 2008).

Table 2.1: Basic L1 and L2 Linear Phase Combinations

Measurement	j	k	λ (m)	DD Ambiguity (cycles)
<i>Widelane (WL)</i>	1	-1	0.8619	$\Delta\nabla N_{WL} = \Delta\nabla N_1 - \Delta\nabla N_2$
<i>Narrowlane (NL)</i>	1	1	0.1070	$\Delta\nabla N_{NL} = \Delta\nabla N_1 + \Delta\nabla N_2$
<i>Ionosphere-free</i>	1	$-f_1/f_2$	0.4844	$\Delta\nabla N_{IF} = \Delta\nabla N_1 - (f_1/f_2)\Delta\nabla N_2$
<i>L1 Only</i>	1	0	0.1903	$\Delta\nabla N_1$
<i>L2 Only</i>	0	1	0.2442	$\Delta\nabla N_2$

For the linear phase combinations, the longer the wavelength of the derived ambiguities, the easier to fix the integer values. Thus, among all combinations, the WL ambiguity is the easiest ambiguity to fix; however the errors, e.g. ionospheric error, noise, and multipath, are amplified. The positioning accuracy is affected by these errors after the fixing of the WL ambiguity.

2.3 Observation Errors and Modeling

The observation models described by Equations (2.1) and (2.2) contain several measurement errors. According to Lachapelle (2008), there are three classes of errors in the GPS observations, namely

- a) Satellite-based errors: the satellite orbital errors, the satellite clock errors, and the IFBs due to the satellite hardware are included in this category;

- b) Propagation errors: the ionospheric error, the tropospheric error, multipath, and interference are included in this category;
- c) Receiver-based errors: the antenna errors, the receiver clock errors, the receiver IFBs, and the receiver noise are included in this category.

The two primary characteristics of the given error are the magnitude and the variability. The magnitude of the error depends on the observation model used since some of the errors will be reduced or even eliminated through differencing. The variability of the error needs to be theoretically and experimentally investigated to determine the temporal correlation and, if differenced errors are of concern, the spatial correlation. Depends on the characteristic of the error sources, the errors are determined through calibration, modeling and estimation, or are eliminated through differencing.

2.3.1 Satellite Orbital Error

As a trilateration positioning system, GPS needs to provide the user with the satellite position (in specified coordinate frame) and velocity information, which is actually transmitted as broadcast ephemeris in the navigation message. However, the uncertainty in the broadcast ephemeris results in the satellite orbital errors. The ephemeris information is predicted from the previous measurements of satellite motion and knowledge of the Earth's gravity field, and this prediction happens once every several hours and has low accuracy. The resulted orbital error is generally in the metres level and can reach tens of metres if the prediction is weakened. Note that the new CNAV data includes new satellite ephemeris parameters to improve the satellite position accuracy.

An effective way to account for the orbital error is to use the post-processed precise orbit parameters provided by the agencies, e.g. the International GNSS Service (IGS) provides a final precise ephemeris with accuracy in centimetres but latency of 13-20 days. The limitation of the precise orbit parameters is that it can not be applied in real-time. Alternatively, the orbital error can be largely reduced through differencing between receivers for DGPS applications. The typical baseline error due to orbital uncertainty can be expressed as (Lachapelle 2008)

$$\delta b = b \frac{\delta \rho_0}{\bar{\rho}_0} \quad (2.10)$$

where

δb is the typical baseline error,

b is the length of the baseline, and

$\bar{\rho}_0$ is the mean distance between a satellite and a receiver.

Given a satellite orbital error of 2 m, the baseline estimation error is about 1 cm over a 100 km baseline with an average 20000 km satellite-receiver distance. The orbital error is considered negligible over shorter baselines.

2.3.2 Satellite Clock Error and IFBs

The satellite clock error is defined as (IS-GPS-200D 2006)

$$dt = t_{sv} - t \quad (2.11)$$

where t_{sv} is the effective signal transmission time and t is the actual GPS time of the signal transmission. Similar to the satellite orbital error, the satellite clock error is also predicted from previous measurements and is broadcasted in the ephemeris. Besides, the

onboard oscillators have a direct impact on the accuracy of this prediction. The broadcast satellite clock error has an accuracy of several nanoseconds but is broadcasted in real time. IGS also provide post-processed precise clock error estimation with accuracy better than 0.1 nanoseconds and a latency of 13-20 days. For DGPS applications, the satellite clock error is eliminated through between-receiver single differencing or double differencing.

Due to the different delay that the RF module applied to the different signal frequencies, the L1 and L2 signals are not necessarily synchronized as they leave the satellite. The L1 and L2 observations from the same satellite-receiver pair are biased by different amounts which is called the IFB. The broadcast ephemeris contains a parameter, the group delay between L1 P(Y) and L2 P(Y), to account for the effect (IS-GPS-200D 2006)

$$T_{GD} = (t_{L1P(Y)} - t_{L2P(Y)}) / (1 - \gamma) \quad (2.12)$$

where $t_{LiP(Y)}$ is a specific epoch GPS time of the i^{th} frequency P(Y) signal transmitted from the satellite's antenna phase centre. For the IFBs between the civil legacy L1 C/A signal or the modernized civil L2C signal and the L1 P(Y) and L2 P(Y) signal, there is inter-signal correction (ISC) provided by the new CNAV data. For maximum accuracy, the single-frequency L1 C/A user must use this correction as shown below (IS-GPS-200D 2006)

$$dt_{L1CA} = dt - T_{GD} + ISC_{L1C/A} \quad (2.13)$$

Similarly for the single-frequency L2C user, the modification is (IS-GPS-200D 2006)

$$dt_{L2C} = dt - T_{GD} + ISC_{L2C} \quad (2.14)$$

The values of ISC_{L1CA} and ISC_{L2C} are measurements respectively representing the mean satellite differential bias between the L1 P(Y) code and the L1 and L2 civilian codes. Their mathematical relationships are shown below (IS-GPS-200D 2006)

$$\begin{aligned} ISC_{L1CA} &= t_{L1P(Y)} - t_{L1CA} \\ ISC_{L2C} &= t_{L1P(Y)} - t_{L2C} \end{aligned} \quad (2.15)$$

where t_{Lix} is the transmit GPS time of one specific epoch of the i^{th} frequency of x signal.

2.3.3 Ionospheric Delay

The ionosphere extends from a height of about 500 km to about 1000 km above the earth, which is a region of ionized gases with an abundance of free electrons and ions. The ionization is caused by the sun's radiation, and the state of the ionosphere (the density of the ionized gases) is determined primarily by the intensity of the solar activity that varies from day to day and changes with seasons and the phases of the eleven-year solar cycle. There are also unpredictable short-term effects and localized anomalies due to geomagnetic disturbances. The state of the ionosphere changes widely between day and night with an electron density (number of electron/m³) peak around 2 p.m. local time.

Phase Advance and Group Delay

The atmosphere (ionosphere and troposphere in the context of this work) that the GPS signal travels through from the satellite to the receiver is a different medium from the vacuum and thus the changes the velocity (speed and direction included) of propagation of the GPS radio signals is different from those of the velocity in vacuum. This phenomenon is called refraction. The refractive index is thus defined by Equation (2.16)

to mathematically relates the speed of the propagation of the signals in other mediums (v) to the speed in the vacuum

$$n = \frac{c}{v} \quad (2.16)$$

Due to the inconsistent distribution of the atmosphere composition, the refractive index changes along the path of the signals and results in the bending of the path of the signals. Signals actually travel longer path than the geometrical Line-of-Sight (LOS) path (Snell's Law). However, the propagation time along this bent path is shorter than that for the LOS path (Fermat's principle of least time). This additional delay in signal propagation due to refraction is described by (Misra & Enge 2001)

$$d\tau = \frac{1}{c} \int_R^S (n(l) - 1) dl \quad (2.17)$$

where l represents the signal path and $n(l)$ represents the changing refractive index profile along the signal path in the medium.

In addition, if the refractive index of a medium depends on the frequency of the signal, the medium is referred to as dispersive. For the GPS radio frequency signals, the ionosphere is dispersive while the troposphere is not. As a result, there exists a phenomenon for the signals travelled through the ionosphere, called code-carrier divergence, where the code phase measurement is measured too long while the carrier phase measurement is measured too short. This phenomenon is due to the fact that the modulation code signal travels at a different speed than the carrier in the dispersive

ionosphere medium. This difference can be described by the relationship between the phase refractive index (n_p) and the group refractive index (n_g) (Misra & Enge 2001)

$$n_g = n_p + f \frac{dn_p}{df} \quad (2.18)$$

The ionospheric refraction index changes with the varying density of the electrons along the signal path. Instead of accurately determine the refraction index profile in Equation (2.17), the ionospheric refraction index is approximated by a Taylor-series expansion up to the third order in the literature. The three expansion orders are referred to as the first-, second-, and third-order ionospheric delays (Odiijk 2002).

The first-order ionospheric delay is a function of the total electron content (TEC) that is defined as the number of electrons in a tube of 1 m² cross section extending from the receiver to the satellite (Misra & Enge 2001)

$$TEC = \int_R^S n_e(l) dl \quad (2.19)$$

where $n_e(l)$ denotes the changing electron density along the signal path. Note that TEC is measured in units of TEC Units (TECU), which is defined as 10¹⁶ electrons/m². One TECU results in approximately 0.16 m and 0.26 m of ionospheric delay on GPS L1 and L2 measurements, respectively. The signal from the zenith satellite passes the ionosphere in the shortest way, and thus the TEC is the smallest and is referred as to vertical TEC (VTEC). In this work, the TEC along the slant paths is referred as to slant TEC (STEC). Note that the TEC is not a constant due to the variable electron density. Moreover, the

TEC has a strong dependence on the elevation of the satellite since the signal path through the ionosphere gets longer with a lower elevation angle.

The phase refractive index (to the first order) of a radio signal of frequency f is (Misra & Enge 2001)

$$n_p \approx 1 - \frac{40.3n_e}{f^2} \quad (2.20)$$

Thus, the phase delay due to the refraction as the signal pass through the ionosphere is calculated as (Misra & Enge 2001)

$$\begin{aligned} d\tau_p &= \frac{1}{c} \int_R^S (n_p(l) - 1) \\ &= -\frac{1}{c} \int \frac{40.3 \cdot n_e(l)}{f^2} dl \\ &= -\frac{40.3 \cdot STEC}{cf^2} \end{aligned} \quad (2.21)$$

It is shown that, however, the phase delay is negative, i.e. the phase is advanced. And the magnitude of the phase advance depends on the TEC along the signal path, which can be represented in metres as

$$I_\phi^s = c \cdot d\tau_p = -\frac{40.3 \cdot STEC}{f^2} \quad (2.22)$$

where the superscript s denotes the slant ionospheric delay or advance. According to Equation(2.18), the ionospheric group delay is calculated in metres as

$$I_\rho^s = -I_\phi^s = \frac{40.3 \cdot STEC}{f^2} \quad (2.23)$$

It is found that the ionospheric group delay calculated from the pseudorange measurements has the same magnitude but opposite sign as the ionospheric phase advance calculated from the carrier phase measurements. This is a very important conclusion that is useful in estimating the ionospheric delay when processing dual-frequency pseudorange and carrier phase measurements. Note that the second- and third-order phase ionospheric delays are also of opposite sign to their group delay counterparts while the magnitudes do not hold the same relationship (Odijk 2002), if the higher-order ionospheric delays other than only the first-order delay are accounted.

Fundamental Ionosphere Models

Many models are proposed to account for the ionospheric delay or advance in the GPS measurements. If the 3-dimensional structure and characteristic of the ionosphere are expressed in terms of the refraction index variability and the electron density variability in Equation (2.21), a 3-dimensional ionosphere model can be derived. However, under some assumptions, a 2-dimensional ionosphere model can be derived with the estimation of the STEC in Equations (2.22) and (2.23), which is less complicated but also less accurate than the 3-dimensional model. In the following section, in the context of this work, several fundamental concepts for 2-dimensional ionosphere modeling are discussed.

The basic ionosphere model in the literature is the so called single-layer model (SLM), which ignores the electron density variability and lateral electron gradients and considering the ionosphere as a single-layer thin shell surrounding the earth. By

exploring the geometrical relationship between the STEC and the VTEC as shown in Figure 2.1, a standard mapping function is derived for the easy utilization of the SLM.

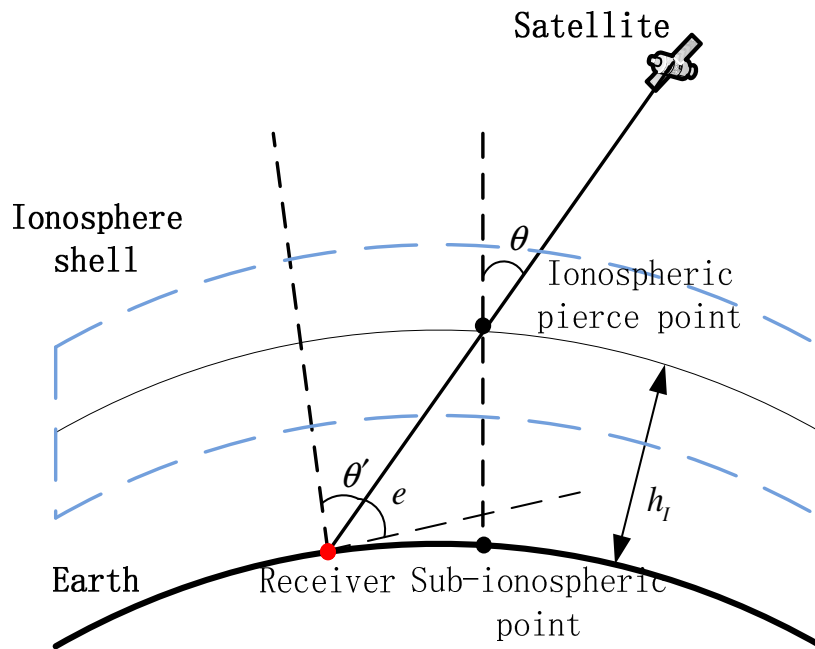


Figure 2.1: Ionosphere single-layer model

A mean height (h_i) of the ionosphere shell has to be firstly determined for this shell height typically varies in the range of 300-400 km in the mid-latitude area during the minimum phase of the solar cycle. The ionospheric pierce point (IPP) is then defined as the point of the intersection of the slant signal path and the single-layer ionospheric shell at height h_i . The STEC refers to the TEC along the slant signal path in the ionosphere shell, and the VTEC refers to the TEC along the path that is normal to both the earth's surface and the assumed shell and passes the IPP in the ionospheric shell. Obviously, the STEC is always greater than or equal to the VTEC counterpart and are only the same for

the zenith satellite. Using geometry, the VTEC is mapped from STEC through the zenith angle θ at the IPP as

$$STEC = VTEC \cdot \frac{1}{\cos(\theta)} \quad (2.24)$$

Further, according to the law of sines, it is shown that

$$\frac{\sin \theta'}{r_E + h_I} = \frac{\sin \theta}{r_E} \quad (2.25)$$

where θ' represents the satellite's zenith angle at the receiver position and r_E represents the radius of the earth. Finally, the mapping function between the STEC and the VTEC in terms of elevation angle e is defined as

$$\begin{aligned} m(e) &= \frac{1}{\cos(\theta)} = \left(\sqrt{1 - \sin^2(\theta)} \right)^{-1} \\ &= \left(\sqrt{1 - \left(\frac{r_E \cdot \cos(e)}{r_E + h_I} \right)^2} \right)^{-1} \end{aligned} \quad (2.26)$$

The ionosphere SLM is a simplification and an approximation based on some assumptions. However, this model will introduce errors if those assumptions are not true. While there are other mapping functions as discussed in Schaer (1999), they provide similar performance for the scenario with most of the observations above 15° , but generally the SLM mapping function provides a satisfactory performance in terms of complexity and computation burden.

The well-known Klobuchar model, also known as the broadcast model for the parameters are broadcasted by the satellites in the navigation message, utilizes another mapping

function described by Equation (2.27) that can be considered as an approximation of Equation (2.26) (Klobuchar 1987)

$$m(e) = 1.0 + 16.0(0.53 - e)^3 \quad (2.27)$$

where e still represents the satellite elevation angle at the receiver position but in units of semi-circles (180 degrees). In order to correct the ionospheric delays for all the available receiver-satellite pair, the Klobuchar model represents the diurnal variation of the VTEC with a half cosine function. The VTEC in units of metres is represented by (Misra & Enge 2001)

$$\frac{VTEC}{c} = \begin{cases} A_1 + A_2 \cos\left(\frac{2\pi(t - A_3)}{A_4}\right), & \text{if } (t - A_3) < \frac{A_4}{4} \\ A_1 & , \text{otherwise} \end{cases} \quad (2.28)$$

where

A_1 is the night-time constant offset of 5 ns,

A_2 is the amplitude of the cosine function,

A_3 is the phase of the daily maximum TEC which is 14:00, local time, and

A_4 is the period of the cosine function.

A_2 and A_4 are fit by cubic polynomials using the eight parameters broadcasted in the navigation message, and four for each parameter calculation. Besides, the receiver's latitude, longitude, satellite elevation and azimuth angles, and local time are necessary information for calculating the ZID. The detailed procedures have been presented in Klobuchar (1987) and IS-GPS-200D (2004). Having the mapping function and the

VTEC, one can compensate the STEC for each receiver-satellite pair with single-frequency receivers.

The Klobuchar model is empirically derived from a large amount of data and is intended for single-frequency receivers with low complexity and computational requirements. The performance of this model is demonstrated using real data, from which it is observed that 50% of the root-mean-square (RMS) range errors due to ionospheric delay are compensated (Klobuchar 1987).

Currently, there is another emerging technique using local or global GPS receiver station networks to model the ionosphere error. For the user surrounded by a local GPS receiver station network, a local ionosphere model or map can be estimated to assist the positioning. Besides, there is also global ionosphere maps (GIM) produced by some research institutes, e.g. Centre for Orbit Determination in Europe (Schaer 1999), to be adopted for post-processing. These GIM provide instantaneous “snapshots” of the global TEC distribution by interpolating, in both space and time, using data provided by more than 100 continuously operating GPS receivers worldwide.

2.3.4 Tropospheric Delay

The troposphere extends 9 km over the pole and 16 km over the equator and is the region where most of the water vapor is located. In GNSS literature the troposphere is often defined as the region up to about 40 or 50 km, where the neutral atmosphere is dense enough to significantly delay signals. It is non-dispersive for the GPS frequencies and has

refraction effects on the GPS signals causing group and phase delays. The index of refraction for the GPS signals passing through the troposphere is referred to as refractivity, which is usually divided into dry (hydrostatic) and wet parts. Thus the tropospheric delay is subdivided into dry (hydrostatic) and wet components with the former accounts for 80-90% of the total errors and is a function of the surface temperature and pressure and the latter accounts for 10-20% of the total errors and is a function of the partial pressure of water vapor and the surface temperature (Lachapelle 2008).

The dry component can be predicted very accurately while the wet component is difficult to predict due to the variability of the water vapor. There are several ways to compensate the tropospheric delay: a) apply a tropospheric model, e.g. Hopfield (1970) and UNB3 model (Leandro et al 2006), b) estimate a residual zenith delay along with the other parameters, and c) use a water vapor radiometer for a better accuracy but this method is expensive. Both the troposphere model and the estimation methods model the zenith delay maps it to the slant delays using typical mapping function. In these ways, the typical accuracy is better than 1% for the dry component but only 10-20% accuracy for the wet component.

The tropospheric delay is strongly correlated over short baseline for DGPS applications only when the height difference of the rover and reference receivers is small and thus can be neglected. However, with long baseline or the height difference is large, the spatial correlation is weakened and the tropospheric delay is not negligible. With the

tropospheric models that account for the height dependence, the resulting typical differential error is rarely larger than 3 parts-per-million (ppm) (Lachapelle 2008). In addition to the use of the expensive water vapor radiometer for better accuracy, the growing GPS networks are also used to predict the relative tropospheric wet component (Zhang 1999).

2.3.5 Multipath

Multipath occurs when a signal reaches the receiver antenna via multiple paths in addition to the LOS path, which causes systematic error in the code and phase measurements. The magnitude of the resulting multipath error depends on the reflector, the antenna gain pattern, and the correlator used in the receiver. Multipath interferes with the LOS signal in the GPS receiver correlator and results in error when determining the arrival time of the LOS signal. It affects the code and phase measurements and the code multipath error (typically smaller than 1/2 chip length of the PRN code) is larger than the phase multipath error (typically 1/4 phase cycles). The multipath error is non-Gaussian and decorrelates spatially quickly but correlates from day-to-day for a given location. In high-end GPS receivers, advanced correlators are employed to reduce or mitigate the code multipath error. However, the phase multipath is still one major error source for precise positioning since it decorrelates between receivers at the two ends of the long baseline and cannot be eliminated through differencing.

2.3.6 Receiver clock error and IFB

The receiver clock error is defined as the difference of the effective transmission time in the frame of the receiver's clock with respect to the actual transmission GPS time of that signal. The receiver IFBs are similar to the satellite counterpart but received few attentions. In fact, the receiver clock error and IFBs do not affect the general GPS positioning applications, since they are eliminated in the DD observations or estimated if other types of observations are employed. However, the receiver IFBs play an important role in time-transfer applications and the determination of the absolute ionospheric delays using dual-frequency measurements. Liu (2004) employed the SD model to cancel the satellite IFB to investigate the receiver clock error and the receiver IFB. The behavior of them is analyzed in a relative manner (the differential SD IFB between two receivers). The research results indicate that the receiver clock error itself is likely a white noise process, i.e. a new unknown for each epoch, but the receiver IFB can be captured adequately by a simple constant rate-of-change (velocity) model. Gao et al (1994) studied the behavior of the L1/L2 IFB using data from a GPS network and showed that the IFB is constant at ± 0.1 ns can be estimated with the accuracy of ± 0.5 ns.

2.3.7 Receiver Noise

The receiver noise arises from the receiver tracking loop and is related to the thermal noise, the dynamic stress, and the quality of the oscillator. The L1 C/A code noise ranges from 5 to 200 cm for LOS measurements while it is only 10 cm level for the P(Y) code measurements. With advanced correlator and tracking loop structures, the code noise can be reduced to 10 cm level. The carrier phase noise is only in the level of millimetre or

sub-millimetre (Lachapelle 2008), which does not affect the DGPS precise positioning much.

2.4 Summary

This chapter reviewed the principle GPS L1 and L2 signals, measurements, and the errors. The L1 and L2 observation models for dual-frequency processing are presented with the corresponding error terms and their effect on positioning. The fundamental ionosphere modeling method is shown. Further discussion on the ionosphere estimation using dual-frequency measurements is in the following chapter.

CHAPTER THREE: L1 AND L2C SINGLE-POINT POSITIONING AND DGPS DUAL-FREQUENCY PRECISE POSITIONING

The L2C signal is partially available and its signal performance has been discussed in the previous chapter. This chapter describes the problems involved in incorporating the L2C measurements into the dual-frequency positioning scenario along with the L1 C/A measurements for civil receivers.

3.1 Position Estimators

GPS is a trilateration system that allows the users to obtain their positions by observing their distances from the signal transmitters with known positions. These observed distances in GPS are referred to as the code pseudoranges and carrier phase cycles. The code pseudorange is noisy and subjects to relatively more multipath while and the carrier phase cycle observations having less noise but also have an unknown integer ambiguity bias. With established mathematical measurement models for code pseudoranges or the carrier phase cycle observations, the user's position can be estimated by the GPS positioning estimators, e.g. the LSQ estimator and the KF, using certain number of measurements.

3.1.1 Least Squares Adjustment

The LSQ adjustment is the standard method to obtain a unique set of values for a set of unknown parameters from a redundant set of observables through a known mathematical

model (Krakiwsky 1990). The redundancy is necessary for improved precision and quality control.

Linear Mathematical Model

Assuming the n -dimensional vector \mathbf{l} of observations is related to the u -dimensional vector of unknown parameters \mathbf{x} by a linear model by the following observation equation

$$\mathbf{l} = \mathbf{A}\mathbf{x} + \mathbf{r} \quad (3.1)$$

where \mathbf{A} is $n \times u$ -dimensional matrix representing the linear relationship between the observations and the unknowns and \mathbf{r} is a vector of random noise errors (residual). The LSQ estimate for x is obtained from minimizing the sum of the squared residuals

$$\begin{aligned} \hat{\mathbf{x}} &= \arg \min_{\mathbf{x}} \|\mathbf{l} - \mathbf{A}\mathbf{x}\|^2 \\ &= (\mathbf{A}^T \mathbf{A})^{-1} \mathbf{A}^T \mathbf{l} \end{aligned} \quad (3.2)$$

where $\hat{\cdot}$ denotes the estimate and $\|\cdot\|$ denotes the Euclidean vector norm. Note that there is no a-priori statistical knowledge about the observation, and this LSQ estimator works for Gaussian and non-Gaussian noise situations. The optimality of this LSQ estimator depends on the properties of the corrupting noise as well as any modeling error (Kay, 1993).

Assuming the residual \mathbf{r} is a noise with zero mean and covariance \mathbf{P} (while the probability of density can be arbitrary), the statistical model of the observations is

$$E(\mathbf{l}) = \mathbf{A}\mathbf{x} \quad (3.3)$$

$$D(\mathbf{l}) = \mathbf{P} \quad (3.4)$$

where $E(\bullet)$ and $D(\bullet)$ are respectively the expectation and covariance functions.

Finally, if the covariance matrix of the observations is used as a weighting matrix, then the LSQ problem becomes a weighted LSQ problem of which the estimate is obtained as a best linear unbiased estimate (BLUE) in the following form (Kay 1993)

$$\hat{\mathbf{x}} = (\mathbf{A}^T \mathbf{P}^{-1} \mathbf{A})^{-1} \mathbf{A}^T \mathbf{P}^{-1} \mathbf{l} \quad (3.5)$$

where it is assumed that $\mathbf{A}^T \mathbf{P}^{-1} \mathbf{A}$ is not singular, which means that there is observation redundancy ($n > u$). The BLUE estimate yields the minimum variance of all unbiased estimators with linear model. Further, if the noise \mathbf{r} conforms to a Gaussian distribution, the BLUE is the optimal minimum variance unbiased estimate for all linear and non-linear models (Kay 1993).

Nonlinear Mathematical Model

Consider the general case where the mathematical model is implicit and non-linear, the observation equation is defined as

$$\mathbf{l} = f(\mathbf{x}) + \mathbf{r} \quad (3.6)$$

where $f(\bullet)$ is a general non-linear function. The linear LSQ method cannot be applied here directly. There are actually two ways to solve this non-linear LSQ problem and both ways involve iteration. One is to attempt to directly resolve the minimization problem described by Equation (3.2) through the linearization of the derivative of the objective function at each iteration about the current estimate, which is the Newton-Raphson method. The other way is to linearize the model about some nominal value of x and then apply the linear LSQ procedure, which is the Gauss-Newton method (Kay 1993).

Assuming that the LSQ estimates $\hat{\mathbf{x}}$ and the resulting adjusted observation $\hat{\mathbf{l}}$ are correct, the following is obtained (Krakiwsky 1990)

$$f(\hat{\mathbf{x}}, \hat{\mathbf{l}}) = 0 \quad (3.7)$$

Then the mathematical model can be approximated by a linear Taylor series as follows (Krakiwsky 1990)

$$f(\hat{\mathbf{x}}, \hat{\mathbf{l}}) = f(\mathbf{x}, \mathbf{l}) + \frac{\partial f}{\partial \mathbf{x}}|_{\mathbf{x}, \mathbf{l}} (\hat{\mathbf{x}} - \mathbf{x}) + \frac{\partial f}{\partial \mathbf{l}}|_{\mathbf{x}, \mathbf{l}} (\hat{\mathbf{l}} - \mathbf{l}) = 0 \quad (3.8)$$

with the estimate correction

$$\delta \hat{\mathbf{x}} = \hat{\mathbf{x}} - \mathbf{x} \quad (3.9)$$

The linearized mathematical model is (Krakiwsky 1990)

$$f(\mathbf{x}, \mathbf{l}) + \frac{\partial f}{\partial \mathbf{x}}|_{\mathbf{x}, \mathbf{l}} \delta \hat{\mathbf{x}} + \frac{\partial f}{\partial \mathbf{l}}|_{\mathbf{x}, \mathbf{l}} \hat{\mathbf{r}} = 0 \quad (3.10)$$

When f is evaluated with the nominal estimate values \mathbf{x} at each iteration, the misclosure is obtained as

$$\boldsymbol{\omega} = f(\mathbf{x}, \hat{\mathbf{l}}) \quad (3.11)$$

If only the unknown parameters in vector \mathbf{x} is parameterized and with the following design matrix definition

$$\mathbf{A} = \frac{\partial f}{\partial \mathbf{x}}|_{\mathbf{x}, \mathbf{l}} \quad (3.12)$$

The linearized mathematical model becomes similar to Equation (3.1) in the following form

$$\boldsymbol{\omega} = \mathbf{A}\hat{\mathbf{x}} + \mathbf{r} \quad (3.13)$$

3.1.2 Kalman Filter

Compared to the LSQ adjustment, the KF considers the unknown parameters as varying with time and provides a solution for the system with linear dynamics. The state space conception is introduced to provide a convenient mathematical description of the system dynamics and the statistical system errors (Gelb 1974). The unknown parameter vector is now referred to as the state vector, therefore, the measurement model can be described by the following equation in the linear case in the continuous-time domain

$$\mathbf{z}(t) = \mathbf{H}(t)\mathbf{x}(t) + \mathbf{v}(t) \quad (3.14)$$

where

\mathbf{z} is the measurement vector,

\mathbf{H} is the design matrix representing the linear relationship between the observations and the states, and

\mathbf{v} is the residual vector describing the effect of random measurement noise.

KF abstracts the characteristics of the linear dynamic system through a system dynamic model (Gelb 1974)

$$\dot{\mathbf{x}}(t) = \mathbf{F}(t)\mathbf{x}(t) + \mathbf{G}(t)\mathbf{w}(t) \quad (3.15)$$

where

\mathbf{x} is the time varying state vector and a dot represents the time derivative,

\mathbf{F} is the dynamic matrix with coefficients representing the system dynamic,

\mathbf{G} is the shaping matrix with coefficients shaping white noise, and

\mathbf{w} is the driving noise vector with random errors assumed to be zero mean white Gaussian noise.

The details of the solution for the differential equations can be found in Gelb (1974). In reality, most of the applications use discrete-time system states and measurements derived from sampling. As such, the discrete forms of the measurement model and dynamic model are defined as (Gelb 1974)

$$\mathbf{z}_k = \mathbf{H}_k \mathbf{x}_k + \mathbf{v}_k \quad (3.16)$$

$$\mathbf{x}_k = \Phi_{k,k-1} \mathbf{x}_{k-1} + \Gamma_{k,k-1} \mathbf{w}_{k-1} \quad (3.17)$$

with the discrete-time transition matrix $\Phi_{k,k-1}$ calculated from the continuous-time transition matrix Φ as (Gelb 1974)

$$\Phi_{k,k-1} = \Phi(t_k, t_{k-1}) \quad (3.18)$$

and the random noise driven vector

$$\Gamma_{k-1} \mathbf{w}_{k-1} = \int_{t_{k-1}}^{t_k} \Phi(t_k, \tau) \mathbf{G}(\tau) \mathbf{w}(\tau) d\tau \quad (3.19)$$

where the subscript denotes the discrete time point and the symbols without subscript indicate the continuous-time form.

Assuming that the driving noise and measurement noise are both white Gaussian noise with zero mean and there is no correlation between these two, then, according to Gauss-Markov Theorem and Orthogonal Projection Theorem, KF derives a recursive algorithm to estimate the states described by Equations (3.16) and (3.17) without taking account of the past measurements for the current estimation. The algorithm is comprised of a series of state predictions and measurement update. The state and its corresponding covariance predictions are fulfilled by Equations (3.20) and (3.21)

$$\hat{\mathbf{x}}_k^- = \Phi_{k,k-1} \hat{\mathbf{x}}_{k-1}^+ \quad (3.20)$$

$$\mathbf{P}_k^- = \Phi_{k,k-1} \mathbf{P}_{k-1}^+ \Phi_{k,k-1}^T + \mathbf{Q}_{k-1} \quad (3.21)$$

where

the superscript ‘-’ denotes the predicted term before measurement update and ‘+’ denotes the updated term,

\mathbf{P} is the covariance matrix of the states, and

\mathbf{Q} is the covariance matrix of the driving noise referring to as the process noise matrix which accounts for the uncertainty of the system dynamic model.

For a stationary system, the dynamic matrix \mathbf{F} is time-invariant and thus the continuous-time transition matrix depends only on the time interval and could be calculated as (Gelb 1974)

$$\Phi(t_k, t_{k-1}) = e^{\mathbf{F}(t_k - t_{k-1})} \quad (3.22)$$

The process noise matrix can be computed as (Gelb 1974)

$$\mathbf{Q}_{k-1} = \int_{t_{k-1}}^{t_k} \Phi(t_k, \tau) \mathbf{G}(\tau) \mathbf{Q}(\tau) \mathbf{G}^T(\tau) \Phi^T(t_k, \tau) d\tau \quad (3.23)$$

where $\mathbf{Q}(t)$ is the continuous-time spectral density matrix of the random driving noise.

With the measurement model defined by Equation (3.16), the measurement update procedure is described by Equation (3.24) to Equation (3.26)

$$\mathbf{K}_k = \mathbf{P}_k^- \mathbf{H}_k^T (\mathbf{H}_k \mathbf{P}_k^- \mathbf{H}_k^T + \mathbf{R}_k)^{-1} \quad (3.24)$$

$$\hat{\mathbf{x}}_k^+ = \hat{\mathbf{x}}_k^- + \mathbf{K}_k (\mathbf{z}_k - \mathbf{H}_k \hat{\mathbf{x}}_k^-) \quad (3.25)$$

$$\mathbf{P}_k^+ = (\mathbf{I} - \mathbf{K}_k \mathbf{H}_k) \mathbf{P}_k^- \quad (3.26)$$

where

\mathbf{K} is the Kalman gain matrix representing the optimality of the KF, and

\mathbf{R} is the covariance matrix of the measurements.

The innovation sequence is defined as

$$\mathbf{v}_k = \mathbf{z}_k - \mathbf{H}_k \hat{\mathbf{x}}_k^- \quad (3.27)$$

which can be considered as the new information being introduced into the system by the measurements. Then it is weighted by the Kalman gain matrix to update the states where the Kalman gain matrix acts as a weighting factor that indicates the amount of new information accepted by the system when compared against the amount of current knowledge of the states being inherited and propagated. Note that there are other sets of formulations for the measurement update procedure, which can be found in Gelb (1974).

The presented KF is an optimal, linear minimum-mean-square-error estimator with the system model and measurement models conforming to the Bayesian linear model. Further, the KF is an optimal minimum-mean-square-error estimator if the measurement noise and system uncertainty are jointly Gaussian distributed. The KF, which is referred to as the standard KF in the following section, is not a general solution to all the estimation and filtering problems, although it can be used to solve many of the problems (Kay 1993). In practice, there are many non-linear applications, and, similar to non-linear LSQ problems, they need a linearization step which brings this discussion to the extended KF (EKF). The EKF is not optimal and its optimality depends on the accuracy of the linearization (Kay 1993). Generally, the non-linear system dynamic and the measurement model in discrete form are described as follows

$$\mathbf{x}_k = f(\mathbf{x}_{k-1}) + \mathbf{w}_{k-1} \quad (3.28)$$

$$\mathbf{z}_k = h(\mathbf{x}_k) + \mathbf{v}_k \quad (3.29)$$

where $f(\bullet)$ and $h(\bullet)$ are non-linear functions. The firstly linearization step is going to expand the first order Taylor series of Equations (3.28) and (3.29) at a nominal states point, and, similar to the non-linear LSQ problem, the following are obtained as

$$\delta \hat{\mathbf{x}}_k = \Phi_{k,k-1} \delta \hat{\mathbf{x}}_{k-1} + \mathbf{w}_{k-1} \quad (3.30)$$

$$\delta \mathbf{z}_k = \mathbf{H}_k \delta \hat{\mathbf{x}}_k + \mathbf{v}_k \quad (3.31)$$

where $\delta(\bullet)$ denotes the perturbation. Then the standard KF algorithm is performed with the states perturbation being estimated and the observations misclosure being used as new observations.

3.1.3 Applications in GPS Positioning

GPS positioning is fulfilled by estimating the coordinates of the receiver from the range measurements available in certain coordinate frames (e.g. the Cartesian earth-centered earth-fixed (ECEF) system). The range between the satellite and the receiver is a Euclidean distance, which is defined in the ECEF coordinate system as

$$\rho_0 = \sqrt{(x - x^s)^2 + (y - y^s)^2 + (z - z^s)^2} \quad (3.32)$$

where

x, y, z is the receiver's position parameters in a earth-centered earth-fixed (ECEF) coordinate system, and

x^s, y^s, z^s is the ECEF coordinates of the satellite.

This range is non-linear with respect to the ECEF coordinates, therefore, the measurement from the GPS receiver is non-linear with respect to the user's position in GPS positioning. As shown in Equation (3.8), usually a Taylor series expansion is performed about some nominal trajectory to fulfill the linearization. The nominal trajectory refers to the time series of estimated parameters herein and can be determined before any observation is available. The practical way is to use the state estimate from the last epoch as the nominal trajectory. The states perturbation is actually estimated each epoch and then reset to zero for next epoch. For the EKF case, the innovation sequence is the same as the misclosure.

In this work, the static single-point positioning is performed with the LSQ estimator, while the carrier phase DGPS static positioning is performed with the EKF estimator using a parallel LSQ estimator to obtain a single-point position of the rover.

3.2 Single-point Code Positioning

In the following, the linearized measurement functional models are derived for the single-point positioning with UD measurements as indicated by Equation (2.1).

The non-linearity comes from the relationship between the geometrical ranges in those measurements with respect to the position parameters in certain coordinate system. It follows that the non-linear UD pseudorange functional model in the ECEF coordinate system for single-point LSQ positioning is

$$\rho = \rho_0 + cdT \quad (3.33)$$

The linearized model is derived using the Taylor's series expansion about the nominal trajectory as

$$\rho = \hat{\rho}_0 + \frac{\partial \rho}{\partial x}(x - \hat{x}) + \frac{\partial \rho}{\partial y}(y - \hat{y}) + \frac{\partial \rho}{\partial z}(z - \hat{z}) + \frac{\partial \rho}{\partial cdT}(cdT - cd\hat{T}) \quad (3.34)$$

With the definition by Equation (3.12), one row of the design matrix for one satellite is

$$\mathbf{h} = \begin{bmatrix} \frac{\partial \rho}{\partial x} & \frac{\partial \rho}{\partial y} & \frac{\partial \rho}{\partial z} & \frac{\partial \rho}{\partial cdT} \end{bmatrix} = \begin{bmatrix} \frac{(\hat{x} - x^s)}{\hat{\rho}} & \frac{(\hat{y} - y^s)}{\hat{\rho}} & \frac{(\hat{z} - z^s)}{\hat{\rho}} & 1 \end{bmatrix} \quad (3.35)$$

The state vector can be extracted from Equation (3.34) as

$$\delta \hat{\mathbf{x}} = \begin{bmatrix} x - \hat{x} & y - \hat{y} & z - \hat{z} & cdT - cd\hat{T} \end{bmatrix}^T \quad (3.36)$$

Finally, the misclosure for one measurement, representing the linear model, is described by

$$\hat{r} = \rho - \hat{\rho} = \mathbf{h} \delta \hat{\mathbf{x}} \quad (3.37)$$

Most low cost civil applications of single-point code positioning uses the L1 C/A pseudorange, though there are some applications where L1 code and phase is used, while presently dual-frequency observations require semi-codeless receivers that are generally only available in surveying and geodetic applications. Low cost civil applications can still benefit from the available dual-frequency measurements in estimating ionospheric delay, which will be discussed in Section 3.5 and evaluated in Chapter 4.

3.3 Differential Carrier Phase Positioning

There are three steps for differential carrier phase positioning: a) a float filter designed to obtain a float solution; b) integer ambiguity resolution; c) fixed solution with correctly resolved integer ambiguities, which are discussed in detail in the following.

3.3.1 Functional Models

With the addition of unknown integer ambiguity N and ionospheric delay I (for the interest of this work), the non-linear functional model for the carrier phase measurement is

$$\phi = \rho_0 + cdT + \lambda N - I \quad (3.38)$$

As stated, the carrier phase DGPS precise positioning relies on the resolution of the DD integer ambiguities, and the DD functional model is usually adopted for this purpose, which can be found in Liu (2002) in detail. In this work, however the SD functional model is used for its ability to incorporating a single L2C measurement to estimate the differential ionospheric error, while no DD ambiguity can be formed. The linearized SD functional model for one observation can be described by the following equation

$$\Delta\phi - \Delta\hat{\phi} = \mathbf{h} \cdot \delta\hat{\mathbf{x}}$$

$$= \begin{bmatrix} \frac{x - \hat{x}}{\hat{\rho}} & \frac{y - \hat{y}}{\hat{\rho}} & \frac{z - \hat{z}}{\hat{\rho}} & 1 & 1 & -1 \end{bmatrix} \begin{bmatrix} x - \hat{x} \\ y - \hat{y} \\ z - \hat{z} \\ c\Delta dT - c\Delta d\hat{T} \\ \lambda\Delta N - \lambda\Delta\hat{N} \\ \Delta I - \Delta\hat{I} \end{bmatrix} \quad (3.39)$$

Note that the linearized SD pseudorange model is similar to Equation (3.39) except that the ambiguity term does not exist and the design matrix coefficients of the differential ionospheric error states have an opposite sign. Moreover, it is not necessary to add the pseudorange observation into the estimation process, however in most cases it does to help fast convergence of the filter and becomes necessary while estimating the ionospheric delay using dual-frequency pseudorange and carrier phase measurements.

3.3.2 Dynamic Models

For single-point positioning, no dynamic assumptions are needed if the LSQ adjustment method is used. For precise carrier phase DGPS applications, this section describes the estimated states and their corresponding dynamic models chosen for an EKF solution.

In the linearized model, the estimated states in a SD positioning filter contain three position states (x, y, z) and one SD receiver clock offset ($c\Delta dT$) in metres. There are also one SD ambiguity (ΔN) state, and one SD ionospheric delay (ΔI) state if the differential ionospheric error is estimated explicitly, e.g. the DD ionospheric residual estimated in Liu (2002), for each satellite. As such, the state vector is described by

$$\hat{\mathbf{x}} = [x \quad y \quad z \quad c\Delta dT \quad \Delta N_1 \quad \Delta N_2 \quad \cdots \quad \Delta N_n \quad \Delta I_1 \quad \Delta I_2 \quad \cdots \quad \Delta I_n]^T \quad (3.40)$$

The dynamic models are selected to match the specific application scenarios, which ultimately determine the state transition matrix and the process noise matrix.

For near-stationary positioning applications, such as static positioning or surveying, the position states are adequately modeled as random walk processes described by (both continuous-time and discrete-time form) Equation (3.41)

$$\begin{aligned}\dot{\mathbf{x}} &= \mathbf{w} \\ \mathbf{x}_k &= \mathbf{x}_{k-1} + \mathbf{w}_{k-1}\end{aligned}\tag{3.41}$$

where \mathbf{w} describes the system dynamic (velocity) as a white noise process with a power spectral density amplitude q in units of $\text{m}^2/\text{s}^2/\text{Hz}$. The values of q_x, q_y, q_z (for the $x, y,$ and z dimensions respectively) are chosen specifically according to the receiver's dynamic. Besides, an enhancement can be adopted if the GPS Doppler measurements are available to the receiver. A coarse GPS velocity estimate can be obtained from the Doppler measurements using the LSQ adjustment that could be implemented in parallel with the positioning filter solution (Macgougan 2009).

It is not an easy problem to precisely model the stochastic behavior of the SD receiver clock offset, since there are many factors, e.g. oscillator quality, temperature, receiver dynamic, and vibration, all affecting the modeling. One option is to fully re-estimate the clock offset state epoch-by-epoch. In other words, the clock bias is not modeled but simply reset. This maintains the equivalence between hyperbolic positioning (as found in double differencing technique) and pseudorange (between receiver single difference). If a valid clock model can be employed, then the single differencing technique should outperform the DD functional model in which the clock biases are cancelled out (Macgougan 2009). Liu et al (2004) demonstrated the receiver clock offset is most likely a white noise process (i.e. completely new at each epoch) using data collected from high-

end receivers in practical circumstances. Thus, the SD receiver clock offset is also modeled as a random walk process with large process noise (spectral density $q_{c\Delta T}$ in units of $\text{m}^2/\text{s}^2/\text{Hz}$) to have it fully estimated at each update epoch.

The sub-matrix representing the process noise of the position and SD receiver clock offset states is derived as

$$\mathbf{Q}_1 = \begin{bmatrix} q_x \delta t & 0 & 0 & 0 \\ 0 & q_y \delta t & 0 & 0 \\ 0 & 0 & q_z \delta t & 0 \\ 0 & 0 & 0 & q_{c\Delta T} \delta t \end{bmatrix} \quad (3.42)$$

where δt is the time difference between two continuous epochs.

The SD carrier phase ambiguity states are modeled as random constants with no process noise, which is described by

$$\begin{aligned} \dot{\mathbf{x}} &= 0 \\ \mathbf{x}_k &= \mathbf{x}_{k-1} \end{aligned} \quad (3.43)$$

They are constant values only if the phase tracking is maintained continuously and correctly during the observation time span. The corresponding process noise sub-matrix \mathbf{Q}_2 has only zeroes as its elements.

The ionospheric error is shown to have temporal correlation and the TEC is modeled as a first-order of Gauss-Markov process by Skone (1998). The discrete form of a first-order Gauss-Markov dynamic equation with a correlation time T_c is given by

$$\begin{aligned}\dot{\mathbf{x}} &= -\frac{1}{T_c} \mathbf{x} + \mathbf{w} \\ \mathbf{x}_k &= e^{-\frac{\delta t}{T_c}} \mathbf{x}_{k-1} + \mathbf{w}_{k-1}\end{aligned}\quad (3.44)$$

Liu et al (2003) also modeled the DD ionospheric error as a first-order of Gauss-Markov process to have it estimated along with the carrier phase ambiguities and the position parameters. In this development, the SD ionospheric error states are also modeled as a first-order of Gauss-Markov process with the process noise sub-matrix derived as

$$\mathbf{Q}_3 = \begin{bmatrix} \frac{q_{I,1}T_c}{2} (1 - e^{-\frac{2}{T_c}\delta t}) & 0 & 0 & 0 \\ 0 & \frac{q_{I,2}T_c}{2} (1 - e^{-\frac{2}{T_c}\delta t}) & 0 & 0 \\ \vdots & \vdots & \ddots & \vdots \\ 0 & 0 & \dots & \frac{q_{I,n}T_c}{2} (1 - e^{-\frac{2}{T_c}\delta t}) \end{bmatrix} \quad (3.45)$$

, where q_i is the spectral density of the SD ionospheric error states in units of $\text{m}^2/\text{s}^2/\text{Hz}$.

Note that the velocity states are not included in the estimation for the interest of this work. Namely, the velocity information is not used to predict the position, but the parallel LSQ velocity solution is used to adjust the process noise of the position states. To sum up, for the selected system dynamic models, the state transition matrix is simply an identity matrix, while the process noise matrix is diagonal and is shown as follows

$$\mathbf{Q} = \begin{bmatrix} \mathbf{Q}_1 & 0 & 0 \\ 0 & \mathbf{Q}_2 & 0 \\ 0 & 0 & \mathbf{Q}_3 \end{bmatrix} \quad (3.46)$$

3.3.3 Sequential EKF Implementation

It is indicated in Grewal & Andrews (2001) that updating the vector-valued observations sequentially will improve the computational efficiency by using error decorrelation algorithms that avoids the matrix inversion computation, which is a proper KF implementation on low-performance processors with lower cost and power consumption than the current powerful PC. Besides, the SD observations are mathematically uncorrelated and are suitable for sequential update without the need of the decorrelation procedure. The implementation of the sequential update is described as follows. First of all, the design vector for the i^{th} observation is computed as \mathbf{h}_i . The next step is to form the innovation (\mathbf{v}_i) of this observation based on the states prediction according to Equations (3.20) and (3.21) before update. If necessary, the innovation testing can then be conducted for reliability verification. The Kalman gain for the i^{th} observation is computed as

$$\mathbf{k}_i = \frac{\mathbf{P}_k \mathbf{h}_i^T}{\mathbf{h}_i \mathbf{P}_k \mathbf{h}_i^T + \sigma_i^2} \quad (3.47)$$

where the matrix inversion presented in the standard implementation is avoided. Then the state variance-covariance matrix is updated as

$$\mathbf{P}_k^+ = (\mathbf{I} - \mathbf{k}_i \mathbf{h}_i) \mathbf{P}_k^- \quad (3.48)$$

For an EKF implementation, the error states are actually not predicted but updated only, the unknown parameters are then updated accordingly at each epoch, which means the following

$$\begin{aligned}
\delta \hat{\mathbf{x}}_k^- &= 0 \\
\delta \hat{\mathbf{x}}_k^+ &= \mathbf{k}_i \mathbf{v}_i \\
\hat{\mathbf{x}}_k^+ &= \hat{\mathbf{x}}_k^- + \delta \hat{\mathbf{x}}_k^+
\end{aligned} \tag{3.49}$$

3.3.4 Float DD Solution from Differencing the SD Solution

The SD observation model is chosen as the mathematical positioning model in this work; however, the SD ambiguities are not easily separable from the SD receiver clock offset errors as both appear as biases in the observation equation and DGPS precise positioning requires the resolution of the integer ambiguities. Fortunately, the DD ambiguities and corresponding variance-covariance information can be obtained from double differencing the SD solution, which is equivalent to extracting from the DD observation model, where DD ambiguities insure integer values. The unknown state vector in Equation (3.40) is denoted as $\hat{\mathbf{x}}_{SD}$ which can be transformed to the DD solution through the following operation (MacGougan 2009)

$$\hat{\mathbf{x}}_{DD} = \mathbf{D} \hat{\mathbf{x}}_{SD} \tag{3.50}$$

, where

$$\mathbf{D} = \begin{bmatrix} 1 & 0 & 0 & 0 & \cdots & \cdots \\ 0 & 1 & 0 & 0 & \cdots & \cdots \\ 0 & 0 & 1 & 0 & \cdots & \cdots \\ 0 & 0 & 0 & 0 & \cdots & \cdots \\ 0 & 0 & 0 & 0 & \mathbf{B}_{\Delta N} & \cdots \\ 0 & 0 & 0 & 0 & \cdots & \mathbf{B}_{\Delta I} \end{bmatrix} \tag{3.51}$$

where $\mathbf{B}_{\Delta N}$ and $\mathbf{B}_{\Delta I}$ are block transformation matrix for double differencing the SD ambiguity and the SD ionospheric error states, respectively. If the first satellite is selected

as the reference satellite for further between-satellite differencing, these two block transformation matrices are described by

$$\mathbf{B}_{\Delta N} = \mathbf{B}_{\Delta I} = \begin{bmatrix} -1 & 1 & 0 & \cdots & 0 \\ -1 & 0 & 1 & \cdots & 0 \\ \vdots & \vdots & \vdots & \ddots & \vdots \\ -1 & 0 & 0 & \cdots & 1 \end{bmatrix} \quad (3.52)$$

These operations eliminate the receiver clock offset error and form the DD ambiguity and the DD ionospheric error states, while keeping the position states unchanged. The covariance matrix of the SD solution \mathbf{P}_{SD} , namely \mathbf{P}_k^+ , is transformed accordingly to obtain the covariance matrix of the DD solution (MacGougan 2009)

$$\mathbf{P}_{DD} = \mathbf{D}\mathbf{P}_{SD}\mathbf{D}^T \quad (3.53)$$

Finally, an initial float DD solution containing all the information needed for ambiguity resolution is available and ambiguity fixed position solution can be obtained through the further simple transformation operations.

3.4 Ambiguity Resolution

The GPS carrier phase ambiguity resolution contains two distinct parts: a) the ambiguity estimation problem, i.e. finding the integer candidates out of the float ambiguities from the float solution and b) the ambiguity validation problem, i.e. verifying integer candidates are the correct integers for unambiguous precise carrier phase measurements. Thereafter, a precise fixed position solution is obtained with the ambiguities are correctly resolved.

3.4.1 Ambiguity Estimation

From the float solution obtained in Section 3.3, real-valued estimates for the baseline parameters, ambiguities, and their corresponding variance-covariance matrices are available as

$$\begin{bmatrix} \hat{\mathbf{b}} \\ \hat{\mathbf{a}} \end{bmatrix}, \begin{bmatrix} \mathbf{Q}_{\hat{b}} & \mathbf{Q}_{\hat{b}\hat{a}} \\ \mathbf{Q}_{\hat{a}\hat{b}} & \mathbf{Q}_{\hat{a}} \end{bmatrix} \quad (3.54)$$

where

$\hat{\mathbf{b}}$ is the non-ambiguity states vector obtained in the float solution,

$\hat{\mathbf{a}}$ is the float DD ambiguity vector, and

\mathbf{Q} denotes the covariance matrix.

The ambiguity estimation problem is a non-standard minimization problem described by

$$\tilde{\mathbf{a}} = \arg \min_{\mathbf{a} \in \mathbf{Z}^n} \|\hat{\mathbf{a}} - \mathbf{a}\|_{\mathbf{Q}_{\hat{a}}}^2 \quad (3.55)$$

In fulfilling the criteria presented in Teunissen (1999), there are three admissible integer estimators, namely integer rounding, integer bootstrapping, and integer least-square estimators (Odijk 2002).

The integer least-square estimator is mechanized in the Least-squares AMBiguity Decorrelation Adjustment (LAMBDA) method (Teunissen 1994 and De Jonge & Tiberius 1996), which is deployed as the ambiguity estimator in this research. A main feature of the LAMBDA method is that it provides a decorrelation procedure to transform the original real-value ambiguity estimates $\hat{\mathbf{a}}$ to a new set of ambiguity through a \mathbf{Z} transformation while preserving the integer nature of the DD ambiguities. The

transformations (including the variance transformation) are given by the following equation

$$\begin{aligned}\hat{\mathbf{z}} &= \mathbf{Z}\hat{\mathbf{a}} \\ \mathbf{Q}_{\hat{\mathbf{z}}} &= \mathbf{Z}\mathbf{Q}_{\hat{\mathbf{a}}}\mathbf{Z}^T\end{aligned}\tag{3.56}$$

The volume of the search space is preserved, and is thereby defined as

$$\chi^2 \geq (\hat{\mathbf{z}} - \bar{\mathbf{z}})^T \mathbf{Q}_{\hat{\mathbf{z}}}^{-1} (\hat{\mathbf{z}} - \bar{\mathbf{z}})\tag{3.57}$$

This volume of the search space yields an n-dimensional ellipsoid, and the search is performed at the grid points that are nearest to the true integer estimates, with the distance measured by the information derived from the covariance matrix. Note that the decorrelation procedure is not a prerequisite for the integer search, which can also be performed with the original ambiguities, $\hat{\mathbf{a}}$. However, the decorrelation procedure substantially benefits the computational efficiency as well as the correlation and precision of the DD ambiguities (Teunissen 1994). The detailed implementation can be found in De Jonge & Tiberius (1996).

3.4.2 Ambiguity Validation

The purpose of ambiguity resolution is to obtain a substantial improvement in baseline estimation accuracy by eliminating the ambiguity states to make the carrier phase measurements precise pseudorange measurements. Thus, it is crucial to have the integer estimates to be the true values. A method of validating the integer ambiguity estimates is required, since wrong integer estimates can deteriorate the position solution even worse than the float solution obtained before ambiguity resolution.

Teunissen & Verhagen (2008) discussed the problem of when and how to fix or not to fix the ambiguity, and divided the ambiguity resolution problem to model-driven and data-driven approaches.

The integer least-squares estimator is proved to be optimal for the model-driven approach in maximizing the probability of correct integer estimation, i.e. the success rate (SR) (Teunissen 1999). Unfortunately, the direct calculation of the SR is not an easy work. Thus, approximations have to be applied, and one usual approximation is the lower bound based on integer bootstrapping since the integer bootstrapping estimator has a close-to-optimal performance after applying the LAMBDA decorrelation procedure on the ambiguities. The bootstrapped SR is calculated as (Verhagen 2004a)

$$P_{s,B} = \prod_{i=1}^n \left(2\Phi\left(\frac{1}{2\sigma_{i|I}}\right) - 1 \right) \quad (3.58)$$

with $\Phi(\bullet)$ as the cumulative normal distribution given by

$$\Phi(x) = \int_{-\infty}^x \frac{1}{\sqrt{2\pi}} \exp\left\{-\frac{1}{2}u^2\right\} du \quad (3.59)$$

, and $\sigma_{i|I}$ the conditional standard deviation of the i^{th} ambiguity with the previous $i-1$ ambiguities are sequentially fixed to integer values, which are the by-products of the LAMBDA decorrelation thus assure easy calculation of the success rate. The disadvantages of this method are that the real-value ambiguities, $\hat{\mathbf{a}}$, have no influence on the SR and that the failure rate is not controllable (Teunissen & Verhagen 2008).

A typical method to decide whether or not fix the integer ambiguities is the ratio test given by (Teunissen & Verhagen 2008)

$$\frac{\|\hat{\mathbf{a}} - \check{\mathbf{a}}\|_{\mathbf{Q}_i}^2}{\|\hat{\mathbf{a}} - \check{\mathbf{a}}_2\|_{\mathbf{Q}_i}^2} \begin{cases} \leq \delta, & use \check{\mathbf{a}} \\ > \delta, & use \hat{\mathbf{a}} \end{cases} \quad (3.60)$$

, where $\check{\mathbf{a}}_2$ is the second-best integer candidate from the integer least-squares estimation.

This method is data-driven but often empirical based on testing experience in selection of the threshold value δ . In the literature, a fixed value of 1/2 or 1/3 is used. The ratio test is one kind of the discrimination tests reviewed and tested in Verhagen (2004a, b). Their common problem is the choice of the threshold values. Values, either empirically determined or based on incorrect assumption that the fixed ambiguity estimator $\check{\mathbf{a}}$ is deterministic, are in principle not true (Verhagen 2004a). In addition, the model-driven failure rate is not applicable due to the implicit introduction of a probability of not fixing, and also the quality of the fixed solution cannot be evaluated if the ratio test is applied (Teunissen & Verhagen 2008).

In this work, the combination of the discussed bootstrapping SR evaluation and the ratio test is adopted as the integer ambiguity validation strategy.

3.4.3 Fixed Solution

Having obtained the valid integer ambiguities, the fixed position solution and corresponding covariance information is calculated by the following (De Jonge & Tiberius 1996)

$$\begin{aligned}
\tilde{\mathbf{b}} &= \hat{\mathbf{b}} - \mathbf{Q}_{\hat{b}\hat{a}} \mathbf{Q}_{\hat{a}}^{-1} (\hat{\mathbf{a}} - \tilde{\mathbf{a}}) \\
\mathbf{Q}_{\tilde{b}} &= \mathbf{Q}_{\hat{b}} - \mathbf{Q}_{\hat{b}\hat{a}} \mathbf{Q}_{\hat{a}}^{-1} \mathbf{Q}_{\hat{a}\hat{b}} + \mathbf{Q}_{\hat{b}\hat{a}} \mathbf{Q}_{\hat{a}}^{-1} \mathbf{Q}_{\hat{a}} \mathbf{Q}_{\hat{a}}^{-1} \mathbf{Q}_{\hat{a}\hat{b}} \\
&\approx \mathbf{Q}_{\hat{b}} - \mathbf{Q}_{\hat{b}\hat{a}} \mathbf{Q}_{\hat{a}}^{-1} \mathbf{Q}_{\hat{a}\hat{b}}
\end{aligned} \tag{3.61}$$

Note that \mathbf{b} represents the vector of all non-ambiguity states of the DD state vector, the DD ionospheric error states are included in case the ionospheric errors are estimated.

3.4.4 L1 and L2 Dual-frequency Ambiguity Resolution

For L1 and L2 dual-frequency phase ambiguity resolution, a directly useful way is to make use of the WL technique. The WL is a useful linear phase combination that results in a long wavelength, low noise behavior, and small ionospheric delay in a relative sense. Teunissen (1997) investigated the relative merits of the WL technique by putting it into the framework of the LAMBDA method. The relative higher efficiency of the integer least-squares search of the LAMBDA method derives from the higher precision and lower correlation of the transformed ambiguities. Teunissen (1997) reached the conclusion that the L1 and L2 ambiguities are extremely correlated for the whole range of ionospheric spatial decorrelation, and by replacing either the L1 or L2 ambiguity with the WL ambiguity (not the widelane observable), the WL technique is proved to be useful with the fact that the WL ambiguity has better precision than the original L1 and L2 ambiguities, i.e. the WL ambiguity decorrelates with the original L1 or L2 ambiguity, for the ionosphere-float, ionosphere-fixed, and ionosphere-weighted cases. Further, the LAMBDA decorrelation procedure automatically achieves the WL transformation at the initialization stage of the decorrelating transformation. Moreover, the decorrelating

transformation can go beyond the widelane ambiguity to obtain maximally decorrelated ambiguities to greatly reduce the integer search space.

The numerical results from Teunissen (1994) showed that the volumes of the search space and also the number of the integer candidates decrease more rapidly as a function of the observation time span for the L1 and L2 case, in which the L1 and L2 ambiguities are taken together in a single integer least-squares estimator than the L1 only case. This observation is expected to be the advantage of dual-frequency AR over the L1 only case when the dual-frequency measurements are available.

3.5 Ionospheric Delay Estimation with Partial Availability of L2C Measurements

Described by Equations (2.22) and (2.23), the first-order of ionospheric group delay and phase advance can be determined by the STEC along the signal path. It is not a trivial work to directly calculate the STEC, however, having the dual-frequency measurements with the first-order group delay, referring to as the slant ionospheric delay (SID) on L1 caused by the ionosphere along the signal path from the satellite to the receiver, can be calculated using the pseudorange measurements as follows

$$I_{\rho}^s = -\frac{1}{\gamma-1}(\rho_1 - \rho_2) \quad (3.62)$$

where the superscript s denotes the slant delay and the superscript ρ denotes the code estimate. In other words, the ionospheric delay on L1 is proportional to the differential delay between the L1 and L2 pseudorange. However, the ionospheric delay estimates are expected to be much noisier than the individual pseudorange measurements because of

the differencing between originally two noisy pseudoranges. The dual-frequency carrier phase measurements are much less noisy and an estimate of the ionospheric phase advance on L1 can be obtained as

$$I_{\phi}^s = \frac{1}{\gamma-1} [\lambda_1(\phi_1 - N_1) - \lambda_2(\phi_2 - N_2)] \quad (3.63)$$

It is shown that the ionospheric delay estimate is ambiguous without the attempt to fix the integer ambiguities N_1 and N_2 . However, as long as no occurrence of cycle slip and continuous carrier phase tracking, N_1 and N_2 remain fixed, the changes of ionospheric delay between continuous epochs can be estimated in real time, called time differential delay, which benefit from the precise carrier phase measurements and thus have good precision up to centimetre level (Misra & Enge 2001). Note that we have to account for the IFBs caused by the satellite and receiver hardware when using dual-frequency measurements. Then, Equations (3.62) and (3.63) become

$$\begin{aligned} I_{\rho}^s &= -\frac{1}{\gamma-1}(\rho_1 - \rho_2) + \frac{1}{\gamma-1}(db_{\rho}^R - db_{\rho}^S) \\ I_{\phi}^s &= \frac{1}{\gamma-1}[\lambda_1(\phi_1 - N_1) - \lambda_2(\phi_2 - N_2)] + \frac{1}{\gamma-1}(db_{\phi}^R - db_{\phi}^S) \end{aligned} \quad (3.64)$$

where db represents the IFB. The subscript 1 is omitted in the remaining of this thesis for simplicity and I is then referring to ionospheric delay on L1 otherwise by explicit denotation. It is then shown that the ionospheric delay and phase advance estimates calculated from the raw dual-frequency code and phase measurements are biased by the IFBs. In sum, there are two major problems in estimating the ionospheric error using dual-frequency measurements: a) only noisy estimate from code measurements or precise

but ambiguous estimate from carrier phase measurements; b) estimates interrupted by the IFBs.

3.5.1 Smoothing and IFB Determination

For the first problem, one approach is to smooth the originally noisy code measurements with the original carrier phase measurements as the algorithm described in Hatch (1982)

$$\tilde{\rho}(t_k) = w_k \rho(t_k) + (1 - w_k) [\tilde{\rho}(t_{k-1}) + (\phi(t_k) - \phi(t_{k-1}))] \quad (3.65)$$

with (assuming M epochs in all)

$$w_k = \frac{1}{k}, k = 1, 2, \dots, M \quad (3.66)$$

and $\tilde{\rho}$ the phase-smoothed pseudorange. Having the phase-smoothed pseudoranges with better precision than the original ones, more precise ionospheric error estimates are expected. Alternatively, another approach can be performed in the raw ionospheric error estimates domain with the noisy code-based estimates of the ionospheric delay smoothed by phase-based estimates of the differential delay using the same algorithm shown in Equation (3.65), namely

$$\tilde{I}_\rho^s(t_k) = w_k I_\rho^s(t_k) + (1 - w_k) [\tilde{I}_\rho^s(t_{k-1}) + (I_\phi^s(t_k) - I_\phi^s(t_{k-1}))] \quad (3.67)$$

The two approaches have the same idea to utilize time-differenced phase measurements or phase-based ionospheric estimates to eliminate the ambiguities and then smooth the noisy code measurements or code-based ionospheric estimates. There is another idea of utilizing the difference between the code measurements and the phase measurements, or the difference between the code-based ionospheric estimates and the phase-based ionospheric estimates, as coarse estimates of the phase ambiguities. The following is an

algorithm developed according to this idea in the ionospheric estimates domain (Skone 1998).

$$\begin{aligned}\Delta\tilde{I}(t_k) &= (1-w_k)\Delta\tilde{I}(t_{k-1}) + w_k(I_\rho(t_k) - I_\phi(t_k)) \\ \tilde{I}(t_k) &= I_\phi(t_k) + \Delta\tilde{I}(t_k)\end{aligned}\tag{3.68}$$

These three smoothing approaches stated above are referring to as recursive smoothing approaches herein, which are useful in real-time implementations where a reasonable number of code observations are used to average through any multipath while the relative weight of the phase measurements is slowly increasing. On the contrary, there is also another approach referred to as batch smoothing described by

$$\tilde{I}(t_k) = I_\phi(t_k) - \frac{1}{M} \sum_{k=1}^M [I_\rho(t_k) - I_\phi(t_k)]\tag{3.69}$$

, which is based on the same idea as that in Equation (3.68). In fact, this batch smoothing approach is derived from that recursive smoothing approach, and is useful in post-processing to provide the best absolute ionosphere estimate by averaging through the maximum number of available pseudorange observations (thus averaging out the pseudorange errors).

For the second problem, the IFBs have to be calibrated before estimating the ionospheric error otherwise the estimates will be biased. The disrupting IFBs have two parts come from both the satellite and the receiver ends. With the newly issued CNAV data, the calibration values of these IFBs are included in the broadcast message. Thus, the IFBs in the satellite end will not be a major problem, it is only in the level of $10^{-1} \sim 10^{-2}$ nanoseconds and will be largely reduced with the corrections mentioned. However, the

IFBs from the receiver end needs calibration procedure by the user. In this work, the receiver IFBs are estimated by post processing dual-frequency measurements with a proposed zenith ionospheric delay (ZID) method.

In Figure 2.1, assuming the ionosphere is isotropic which means that the ionospheric delay is only proportional to the length of the signal path no matter where the pierce point is, and given that dual-frequency observations from one satellite can be used to compute a slant ionospheric delay, an simplified algorithm is proposed to map all simultaneously observable slant ionospheric delays to zenith and then use the averaged zenith delay to map down to obtain the slant ionospheric corrections for all available measurements. The essential is to admit that there is the same single ZID for all the satellites in view which covers certain range of ionosphere shell. With the ionosphere SLM and the proposed method, Equation (3.64) is rewritten as the following in terms of the ZID I^z

$$\begin{aligned}\frac{I_\rho^z}{m(e)} &= -\frac{1}{\gamma-1}(\rho_1 - \rho_2) + \frac{1}{\gamma-1}(db_\rho^R - db_\rho^S) \\ \frac{I_\phi^z}{m(e)} &= \frac{1}{\gamma-1}[\lambda_1(\phi_1 - N_1) - \lambda_2(\phi_2 - N_2)] + \frac{1}{\gamma-1}(db_\phi^R - db_\phi^S)\end{aligned}\quad (3.70)$$

Then, the smoothed ionospheric delay is derived as follows through the batch smoothing approach applied on M epochs

$$\tilde{I}^s = -\frac{I^z}{m(e)} + \frac{1}{\gamma-1} \sum_{k=1}^M \frac{(db_\rho^R - db_\rho^S)}{M}\quad (3.71)$$

The above equation is applied as the observation equation for a LSQ adjustment, with observations from p satellites, $p \leq n$ (n is the number of observable satellites), with dual-frequency measurements. The unknown parameters vector is thus defines as

$$\hat{\mathbf{x}} = \begin{bmatrix} I^z & b_1 & b_2 & \cdots & b_p \end{bmatrix}^T \quad (3.72)$$

where b_1, b_2, \dots, b_p are the estimated scaled average of the difference between the receiver and satellite code IFBs as indicated in Equation (3.71). For redundancy requirement, a batch LSQ adjustment is deployed as

$$\begin{bmatrix} \tilde{\mathbf{I}}_1^s & \tilde{\mathbf{I}}_2^s & \cdots & \tilde{\mathbf{I}}_p^s \end{bmatrix}^T = \begin{bmatrix} \mathbf{H}_1 & \mathbf{H}_2 & \cdots & \mathbf{H}_p \end{bmatrix}^T \hat{\mathbf{x}} \quad (3.73)$$

3.5.2 Single-point ZID Method

For single-point positioning, the civil receiver users can only make use of the limited number of L2C measurements at this stage. As such, the simplified ZID method is proposed to provide ionospheric correction for all available L1 C/A code measurements even from those satellites without L2C signal capability, using the ionospheric error estimates obtained from those satellites with L2C signal capability. Based on the previous presentation in this Sub-section 3.5, the proposed algorithm follows as

- a) Determine the IFBs for those satellites with L2C measurements using the method described in Section 3.5.1;
- b) Compensate the SIDs using the IFBs obtained in last step and then map them to corresponding ZID epoch-by-epoch, this step can be represented by this equation

$$I_j^z(t_k) = [I_j^s(t_k) - b_j] \cdot m(e_j(t_k)), \quad j = 1, 2, \dots, p \quad (3.74)$$

- c) Use 1, 2, 3, or all the available p ZID estimates to calculate one single ZID estimate (e.g. simply averaging) which is then mapped to all the measurements from observable satellites to correct the ionospheric delay, this step is summarized in the following

$$\begin{aligned}\hat{I}^z(t_k) &= \sum_j I_j^z(t_k) \\ \hat{I}_i^s(t_k) &= \hat{I}^z(t_k) \cdot m(e_i(t_k)), \quad i = 1, 2, \dots, n\end{aligned}\tag{3.75}$$

In sum, this method is intended for civil receivers to utilize the benefit of the newly modernized L2C signals from a limited number of satellites to compensate the ionospheric error based on the simplified ionosphere SLM model and mapping function. This method is limited by the underlying assumptions and simplifications. The real data testing results will be shown in Chapter 4 under the scenario of single-point positioning to discuss its usage and effectiveness. Besides, the determination of the ionospheric error under this scenario is independent with the positioning filter, however it is worth of investigation to estimate the ionospheric error along with the other parameters in one positioning filter, which is left to the next section for the differential phase positioning.

3.5.3 Differential ZID Method

Not only the advantages on AR will be introduced by the addition of the L2 phase measurements as discussed in Section 3.4.4, but also the ionospheric error can thus be measured and removed by combining the L1 and L2 code and phase measurements as discussed in the previous contents of this Section. For differential phase positioning application, the ionospheric error, in most cases, is the major remaining error source for medium and long baseline scenarios. Many approaches have been proposed to either mitigate or estimate the ionospheric delay using GPS dual-frequency code and phase observations.

The direct way to mitigate the ionospheric delay is to form ionosphere-free linear phase combination which however eliminates the integer property of the DD phase ambiguities, without the attempt to resolve ambiguities into integers. Alternatively, of particular interest are the models proposed by Odijk (2000) where for each DD phase observation, a DD differential ionospheric delay (SID) state is also estimated. This additional state can either be augmented by pseudo-observations of the ionospheric delay (ionosphere-weighted model) or simply estimated using dual-frequency data along with phase ambiguities (ionosphere-float model, which is closely related to the ionosphere-free combination method). With proper stochastic modeling, a weighting of the external ionospheric delay correction, the ionosphere-weighted model is a rigorous technique for fast successful ambiguity resolution and precise baseline estimation, while the ionosphere-float model needs long time to estimate the SID state with significant geometry change (Odijk 2000). It is shown in Liu et al (2003) that the ionosphere-weighted model with simply “0” as the pseudo-observations for all the DD ionospheric delay estimation provides the best positioning accuracy for the dataset used, while the IF combination method provides more noisy position estimate and also needs significant time to converge. In this work, the SID estimation method is also investigated and implemented but with SD observation model and the state vector is defined as Equation (3.40).

For the civil receivers, in order to make use of the available limited number of L2C measurements to estimate ionospheric delay for all the observable satellites, a differential ZID method is proposed based on the ionosphere SLM and where electron density varies

over the projection of a GPS baseline on the shell, compared to the widely documented and tested SID method which estimates the SID along with the signal path from the satellite to the receiver for each satellite pair if DD observations adopted. Due to the partial availability of satellites with L2C signal capability, only 1, 2, or 3 L2C measurements are often available simultaneously, albeit for some short time intervals. A civil-signal receiver capable of tracking only L1 C/A and L2C could attempt to estimate the SID for one or two double differences. However SID states would not be observable for the other satellites. A possible alternative is to estimate a general ionospheric state that is observed by all of the L1 C/A and L2C measurements. As such, the differential ZID method is proposed to estimate only one differential ZID using few numbers of SID calculated from the L1 C/A and L2C code measurements. As shown in Figure 3.1, if PRN i and PRN j are transmitting L2C signal and are in the common view of the rover and base receivers with L1C/A and L2C signal tracking capability, one SID could be calculated for each satellite-receiver path, which is then could be mapped to as ZID using the standard mapping function.

the float filter. Therefore, the unknown parameter vector is changed from Equation (3.40) as

$$\hat{\mathbf{x}} = [x \quad y \quad z \quad c\Delta dT \quad \Delta I^z \quad \Delta N_1 \quad \Delta N_2 \quad \cdots \quad \Delta N_n]^T \quad (3.77)$$

In the design matrix, the standard mapping function is used to map the single SD ZID to obtain SD SID estimates to compensate all the L1 and L2 SD code and phase measurements.

It should be noted that the single differential ZID state approximately represents the difference of the zenith ionosphere in a weighted mean sense between the rover and base receivers, however it is not the best possible estimate since the samples that are located at the various ionosphere pierce points are not necessarily well distributed around each receiver. While much work has been done to develop sophisticated ionospheric models using networks of reference receivers, the purpose of this method is to demonstrate the feasibility of the proposed simple method for a single baseline. The effectiveness of this method is tested using real data in Chapter 5.

3.6 Summary

This chapter reviews the basic principles of GPS L1 and L2 positioning, including L1 single-frequency single-point positioning and L1 and L2C dual-frequency differential phase positioning involving AR. The ionospheric error estimation using dual-frequency L1 and L2C measurements are investigated to help single-point and differential phase positioning applications. Of particular interest is that new methods are proposed with

zenith ionospheric error estimation to compensate ionospheric error as well as help with dual-frequency L1 and L2C AR.

CHAPTER FOUR: TESTING RESULTS AND ANALYSIS OF SINGLE-POINT CODE POSITIONING

With the proposed single ZID method described in Section 3.5.2, this chapter will test the feasibility and effectiveness of the proposed algorithm using real data. The content is organized as follows: first of all, a description of the data collection is presented; then, the single ZID method for ionospheric delay estimation is demonstrated with the generation of interested IFB estimates; finally the single ZID method and the obtained IFBs are applied to a single-point L1 C/A code positioning scenario to evaluate the benefit from the partial availability of L2C measurements in the position domain.

4.1 Data Collection

In order to test the benefit of the partial availability of the L2C signals for a single-point positioning scenario, two data sets were collected at time periods when multiple Block IIR-M satellites transmitting L2C signals were available. The first data was collected over a twenty-two minutes interval on August 14, 2009 beginning at 21:08 UTC time (15:08 local time) on the roof of the CCIT building at the University of Calgary (approximately 51 N, 114 W). Three Block IIR-M satellites, PRN 7, PRN 15, and PRN 17, are in view during this test as well as five other satellites without L2C signals. A sky plot is shown in Figure 4.1 and the elevation angles of the three Block IIR-M satellites as a function of time are shown in Figure 4.2. IF samples were collected with a National Instruments (NI) RF-front end configured such that the L1 and L2 RF modules were driven by a common oscillator and the dual-frequency samples were collected synchronously. The second data set was collected over a nine minutes time period

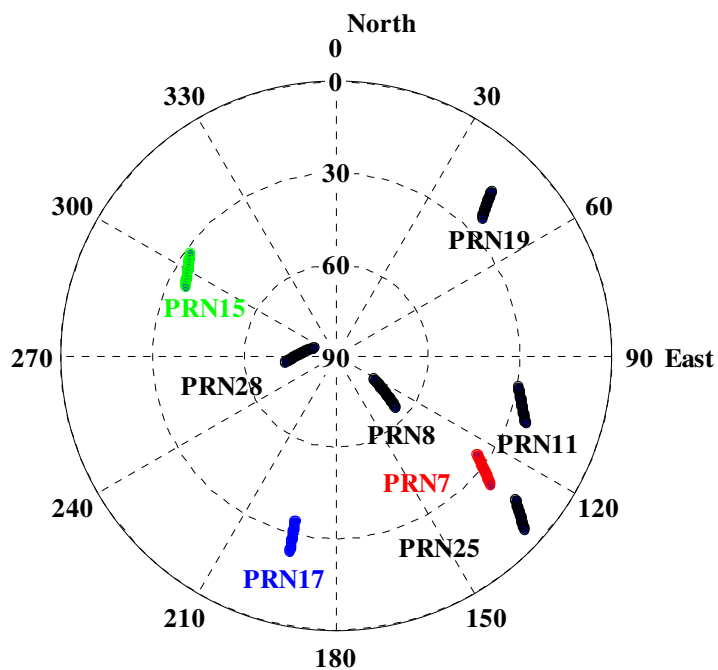


Figure 4.1: Satellites sky plot for the first data set

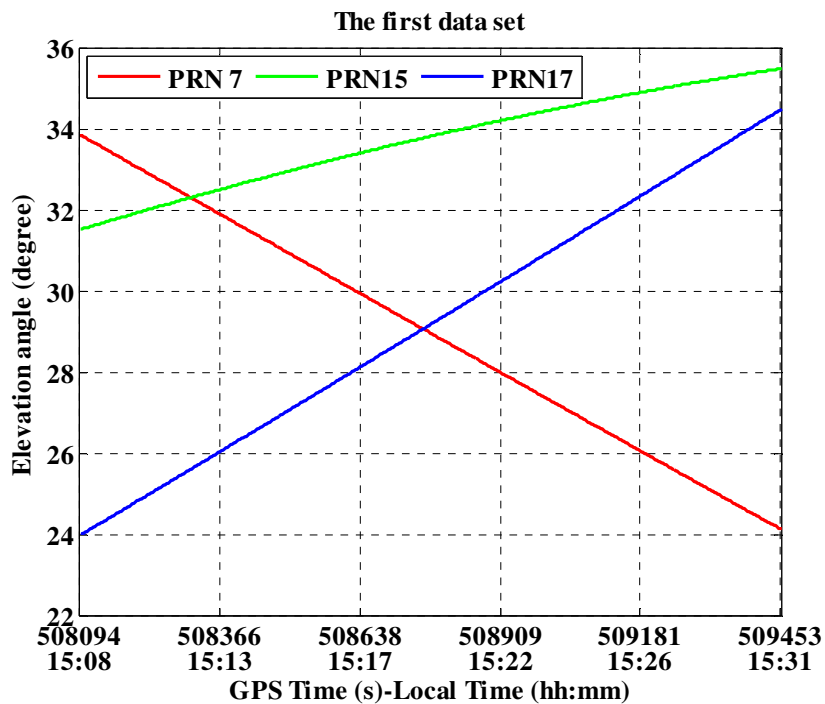


Figure 4.2: Elevation angle for the three available L2C satellites

using the same front-end and configuration as the first data set on August 28, 2009, also on the same antenna on the CCIT building roof. Three Block IIR-M satellites, PRN 12, PRN 15, and PRN 17, are available and during this test. Note that the two data sets are collected allowing for the priority that up to three L2C satellites can be observed and used for the performance evaluation.

The collected IF samples were then processed using GSNRxTM, a highly configurable multi-system, multi-frequency software receiver developed by the Position, Location And Navigation (PLAN) group at the University of Calgary to obtain 1 Hz L1 C/A and L2C code and phase measurements (Petovello et al 2008). Corresponding tracking parameters are set to achieve performance only targets for low-cost civil receivers.

4.2 Ionospheric Delay Estimation Results

The L1 ionospheric group delay and phase advance is calculated using Equation (3.62) and Equation (3.63) using L1 C/A and L2C code and phase measurements respectively. The following ionospheric group delay and phase advance refer to the delay and advance on L1 without explicit indication. An example of the ionospheric group delay and the ambiguous phase advance is shown in Figure 4.3 with measurements from the satellite of PRN 15 during the first data set. It is shown that the ionospheric group delay is corrupted by multipath and noise, which is not surprising since the ionospheric error should have more than two times the standard deviation of the L1 C/A pseudorange if the L2C pseudorange is assumed to be equally noisy. The ambiguous phase advance shown in the

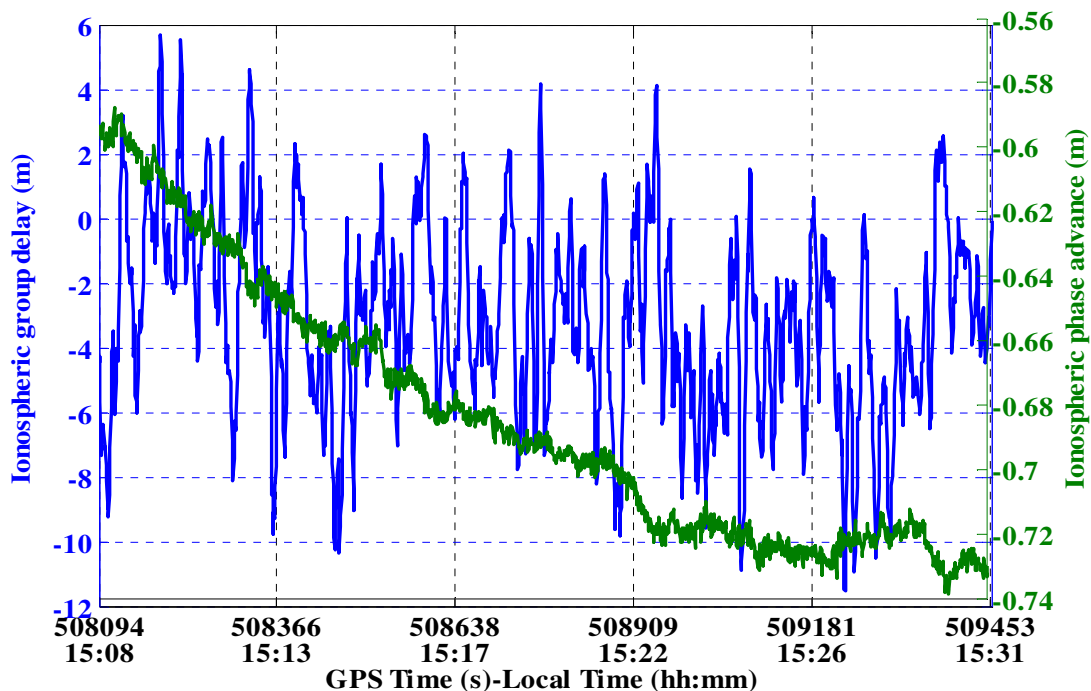


Figure 4.3: Example of the ionospheric group delay and ambiguous phase advance

figure is subtracted by a certain value to align the scale with the group delay, which is still ambiguous but precise. When the batch smoothing approach is applied to this data set, the smoothed L1 SID estimates from each PRN are shown in Figure 4.4. The first thing to note in this figure is that all the SIDs for all the satellites is negative. However, it is expected that all the SIDs are positive and the magnitudes of them decrease as the elevation decreases and increase as the elevation increases. Further more, under the assumption of an isotropic ionosphere, it is also expected that the SIDs for similar satellite elevations be similar, which would imply that the lines in Figure 4.4 should cross at roughly the same locations as those in Figure 4.2. Finally, one would also expect that mapping these SID's to zenith will result in similar zenith values for each satellite with

the isotropic assumption. These zenith values are shown in Figure 4.5 and are clearly not what was expected.

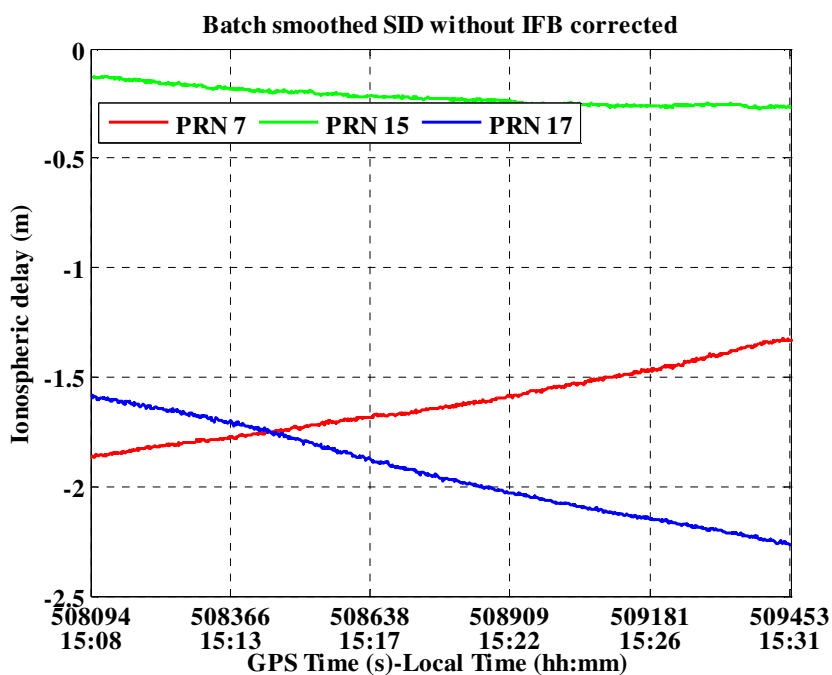


Figure 4.4: Batch smoothed L1 slant ionospheric delay without IFB compensated

The reason for these unexpected results is that the IFBs between the L1 and L2 channels in the receiver have not been accounted for. There is also the possibility of a satellite-dependent IFB, either due to actual satellite biases that are not accounted for in the total group delay parameter broadcast by the navigation message, or due to the large multipath in the pseudorange measurements results in a biased estimate of the mean code delay when averaging many pseudorange measurements. Any bias between the measurements made on the two frequency signals on a given satellite will result in a bias in the L1 SID estimate that is proportional to the IFB.

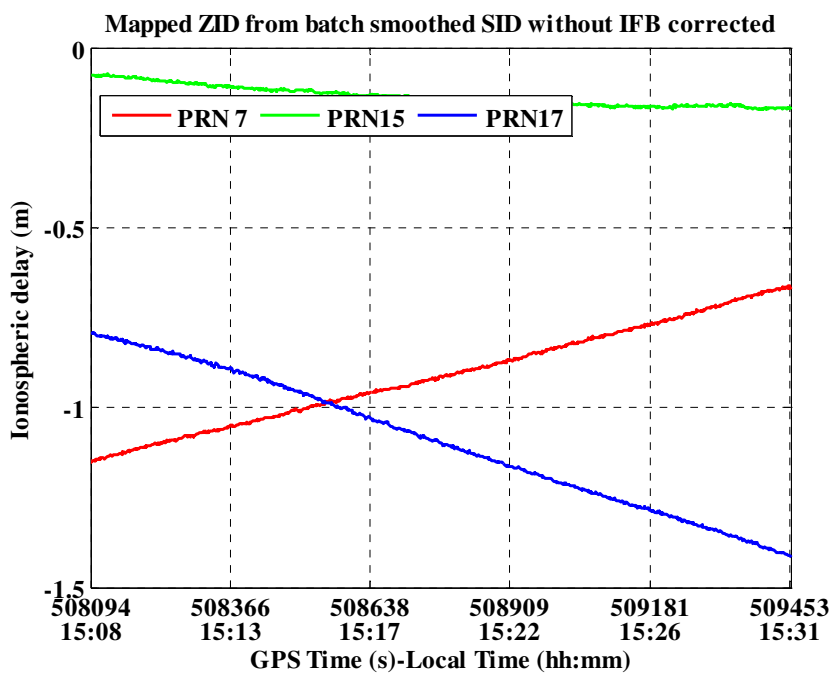


Figure 4.5: Mapped ZID from batch smoothed SID without IFBs corrected

A batch LS approach, described in Section, is used to estimate the IFBs which are then used to correct the SID's shown in Figure 4.4, the corrected SIDs are shown in Figure 4.6. This figure is similar to an approximate mirror image of the elevation angles shown in Figure 4.2, which was to be expected since the ionospheric delay increases as the elevation angle decreases, and the same intersection points are shared by the elevation angle lines and the SID lines. When the corrected slant delays are mapped to zenith, as shown in Figure 4.7, similar zenith delays are obtained for each available L2C satellite, and independent (in terms of noise) time series of zenith ionospheric delay are obtained. Note that the mean value of the three time series is equal to the single zenith delay as estimated by the batch LS approach used to estimate the IFBs. For comparison sense, the

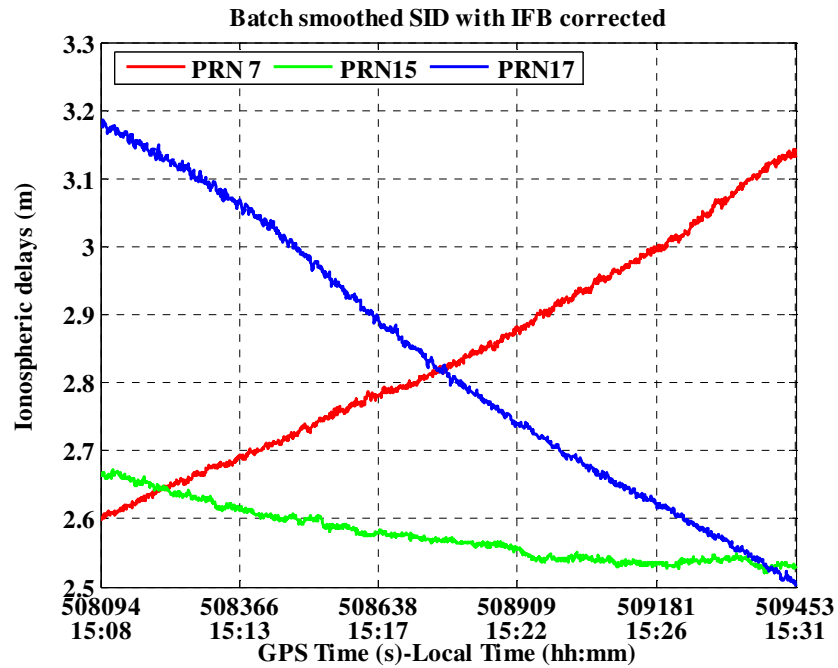


Figure 4.6: Batch smoothed slant ionospheric delays with inter-frequency biases corrected

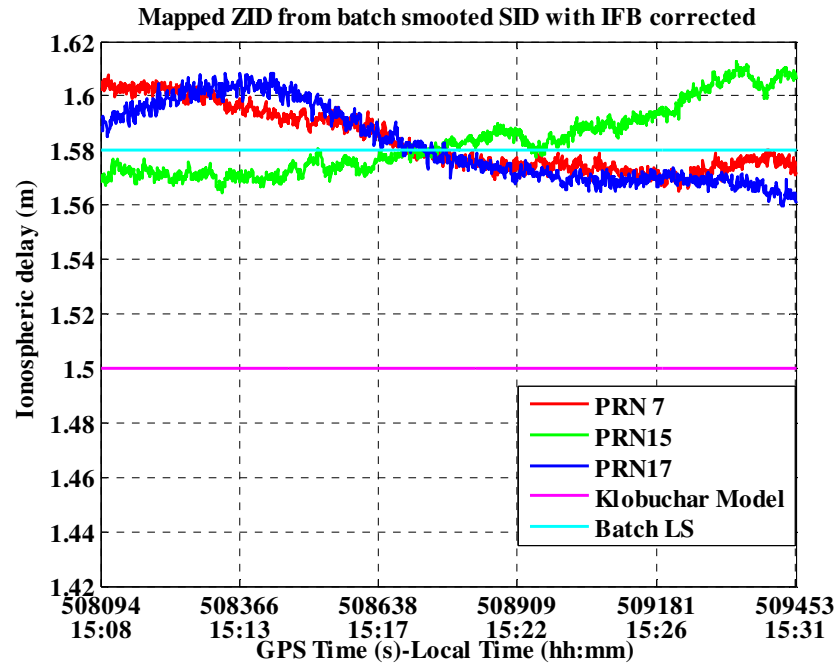


Figure 4.7: Mapped zenith ionospheric delay from inter-frequency biases corrected slant ionospheric delays, with the zenith delays from the batch least-square estimate and the Klobuchar ionosphere model

zenith delay provided by the broadcast Klobuchar ionosphere model is also shown and is close to the estimated zenith delays.

4.3 Single-point L1 C/A code Positioning Results

The ZID estimates shown in Figure 4.7 can now be used to test the proposed algorithm using 1, 2, or all 3 of the ZID estimates and the mapping function described by Equation (2.26) to generate corrections for the other satellites without L2C signal capability. In order to obtain positioning results, an LSQ estimator is used with three position components and a receiver clock offset estimated using only the L1 C/A code pseudoranges. Three scenarios were considered: a) using uncorrected observations (i.e., no ionospheric correction applied), b) using the broadcast Klobuchar ionosphere model, and c) using ionosphere corrections obtained from 1, 2, or 3 of the L1 C/A and L2C measurements derived ZID estimates. A simple averaging is used to combine 2 or 3 ZID estimates to form the single ZID estimate.

Figure 4.8 shows the position errors obtained using L1 C/A pseudoranges without the ionospheric delay being corrected. Even in single-point mode without ionospheric correction, a two metre level horizontal position solution is obtained. The most obvious ionospheric effect is the bias in the vertical component. This is due to the fact that all of the uncorrected measurements are delayed by different amounts. Any common delay is absorbed by the estimated receiver clock offset, the remaining delay differences are then mapped into the position state errors. However, since the satellites are distributed more or less evenly around the receiver, any unaccounted for biases affecting the horizontal

components will tend to average out in the LSQ estimation while in the vertical component this is not possible.

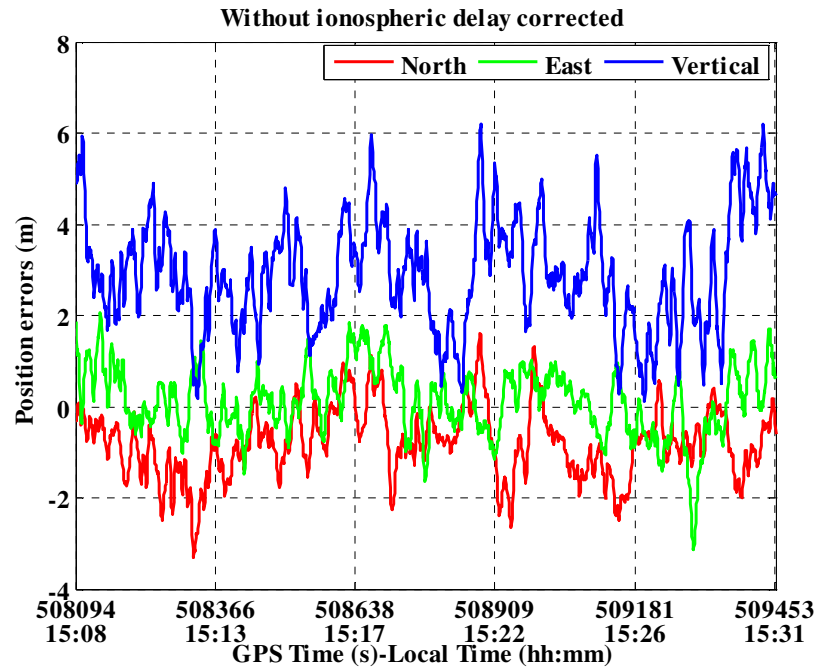


Figure 4.8: Positioning errors using L1 C/A pseudoranges without ionospheric delay being corrected

When the ionospheric corrections calculated from the Klobuchar model are applied to each L1 C/A pseudorange, the vertical position bias disappears though the general shape of the three time series, due mainly to multipath, remains the same. The corresponding position errors are shown in Figure 4.9. Figure 4.10 shows the position errors obtained when the epoch-per-epoch average of the three ZID estimates shown in Figure 4.7 is used to map to SID's. Note that the results are very similar to those obtained from the Klobuchar model. This is not surprising since the ZID estimates obtained from the L2C satellites are all very close to the Klobuchar model ZID and the same mapping function is used, meaning that very similar correction values will be generated using each approach.

The similar results are obtained using two or one of the L2C satellites, which are shown in Figure 4.11 and Figure 4.12 respectively.

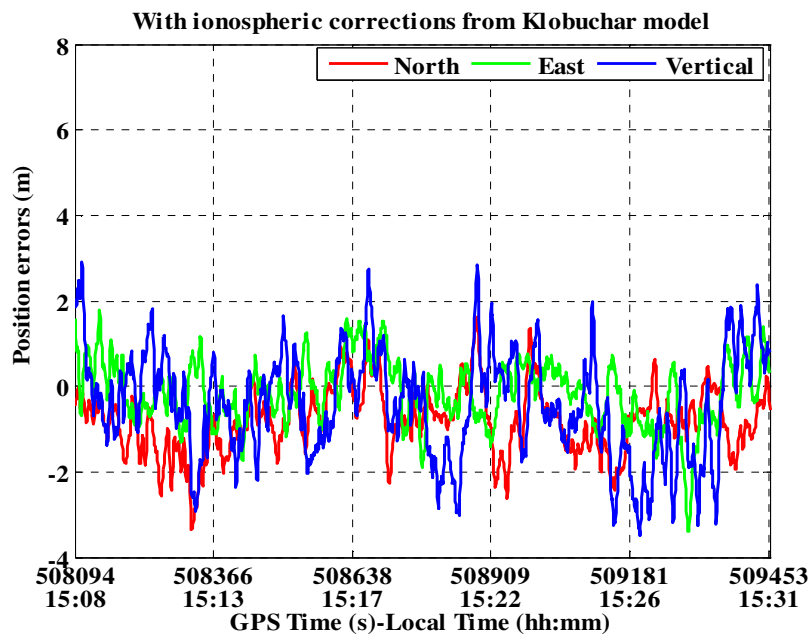


Figure 4.9: Positioning errors using ionospheric corrections from Klobuchar model

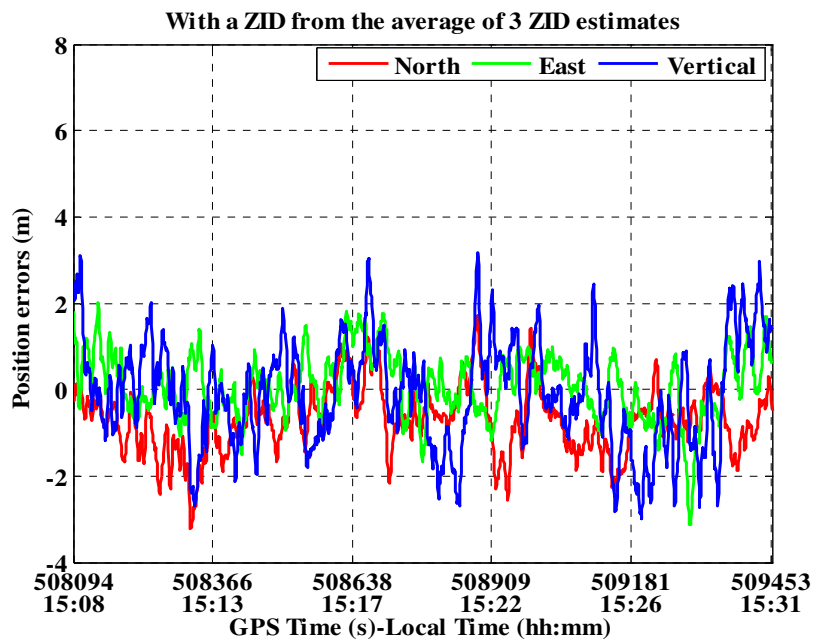


Figure 4.10: Position errors using a zenith value obtained from averaging of the ZID estimates from 3 L2C satellite (PRN 7, 15, and 17)

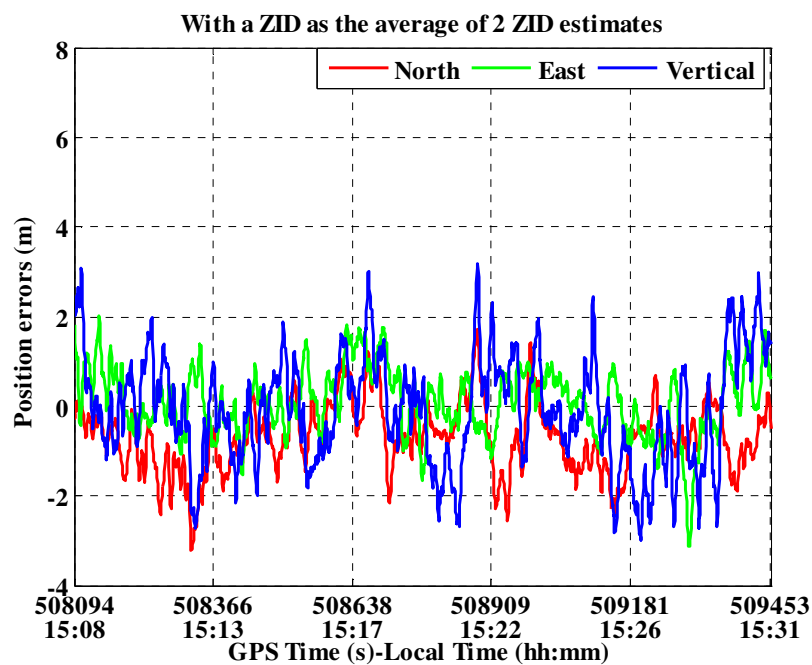


Figure 4.11: Position errors using a zenith value obtained from averaging 2 L2C satellite (PRN 7 and 17) estimated zenith values

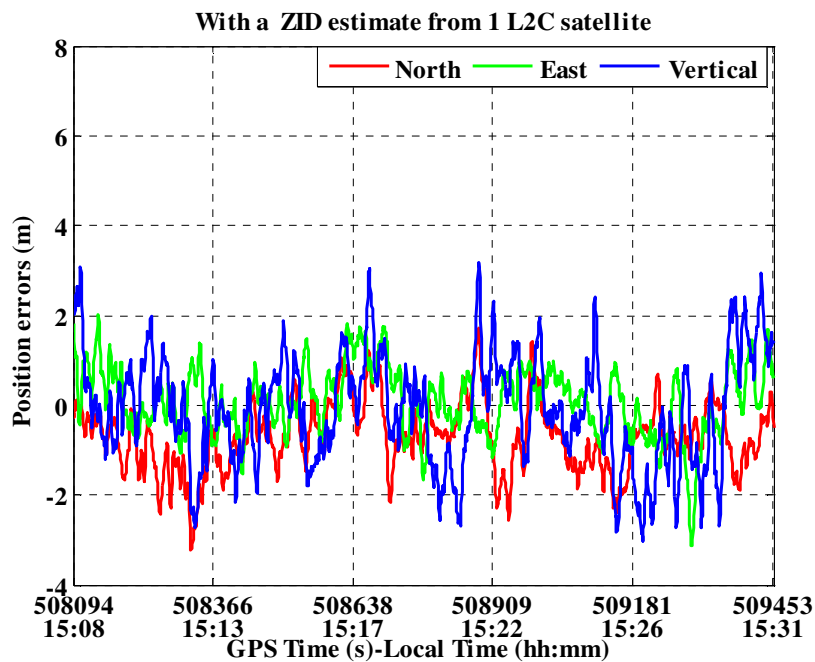


Figure 4.12: Position errors using the estimated zenith delay obtained from 1 L2C satellite (PRN 7)

Table 4.1 summarizes the above position errors in terms of statistics and also shows the results for all other possible combinations of one or two ZID estimates are used to generate the single ZID for the first data set. As stated, since the ZID estimates from 1, 2, or 3 of the L2C satellites or the combination of 1, 2, or 3 of them are quite close to each other, the close position errors are obtained accordingly. All the cases provide the close horizontal accuracy, but the Klobuchar model case and the cases with ZID estimate from the L2C satellites provide 1.9 m vertical accuracy improvement when compared to the case without any ionospheric correction.

Table 4.1: RMS position errors for post-processing of the first data set

Approaches		RMS Position Errors (m)		
		<i>Northing</i>	<i>Easting</i>	<i>Vertical</i>
<i>No correction</i>		1.1	0.8	3.2
<i>Klobuchar model</i>		1.1	0.8	1.3
<i>1 PRN</i>	<i>7</i>	1.1	0.8	1.3
	<i>15</i>	1.1	0.8	1.3
	<i>17</i>	1.1	0.8	1.3
<i>2 PRNs</i>	<i>7 and 15</i>	1.1	0.8	1.3
	<i>7 and 17</i>	1.1	0.8	1.3
	<i>15 and 17</i>	1.1	0.8	1.3
<i>3 PRNs</i>	<i>7, 15, and 17</i>	1.1	0.8	1.3

At this point, two concerns arise regarding the proposed algorithm. The first is that the same data set was used to estimate the IFBs and demonstrate the algorithm. The second is

that the results assumed batch post-processing to determine the biases as well as to estimate the smoothed SIDs. The average of all available pseudoranges and phases was used to estimate the phase ambiguity. In order to overcome both these concerns, two more tests are performed. One is to perform a real-time, recursive epoch-by-epoch processing of the first data set with ionospheric corrections obtained from the recursive smoothing approach. A single arbitrary value of the average of the IFBs obtained from batch processing for PRN 7 and 17 was used to correct the raw code and phase measurements. PRN 15's IFB estimate was excluded from the average due to its large difference with the other two IFB estimates. One hypothesis is that this difference was due to large code multipath on PRN 15 which did not average out over the first 22 minutes data set. The other test is to perform a real-time processing on the collected second data set. In this data set, L2C satellites PRN 12, PRN 15 and PRN 17 were observed. Instead of estimating three IFBs again using the second data itself by a batch processing, the same IFB used for real-time processing of the first data is used herein for the second data set, according to the fact that the receiver IFB is not time correlated and has small variability as long as the same hardware configuration in the same environment.

Figure 4.13 and Figure 4.14 show the estimated SID and ZID, respectively, for the three L2C satellites in the first data set during a real-time processing. The main feature of this figure is the high but decreasing level of noise and multipath evident over the first 300 epochs. This corresponds to the smoothing interval of 300 seconds, where the relative weight applied to the code delay is slowly decreased in favour of the weight applied to

the phase advance. After 300 seconds, only the phase advance derived L1 code delay is used, resulting in a very smooth delay estimate. Note that the estimated slant delays are all positive values, suggesting that the IFB has been effectively removed. Besides, the estimated SIDs generally follows the expectation that becoming smaller as the corresponding elevation increasing and becoming larger as the corresponding elevation decreasing. The estimated ZID differs among the three satellites, with the estimate from RPN 7 being closest to the Klobuchar model value. The effect of the estimated ZIDs on the position accuracy is shown in statistics in Table 4.2. It is observed that the horizontal accuracy are quite close for all the cases and an overall 1.5 – 1.9 m vertical accuracy improvement is achieved while only 0.8 m with the ZID estimate obtained from PRN 15. It may due to higher code multipath or noise of this L2C satellite or its own uncompensated satellite IFB or the combination of both effects.

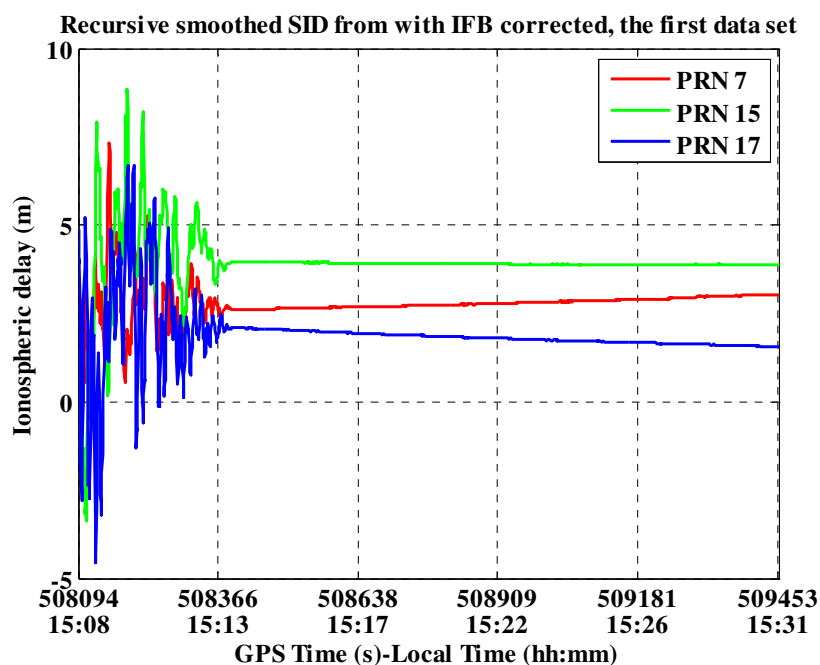


Figure 4.13: Recursive smoothed slant ionospheric delays with the inter-frequency biases corrected for the first data set

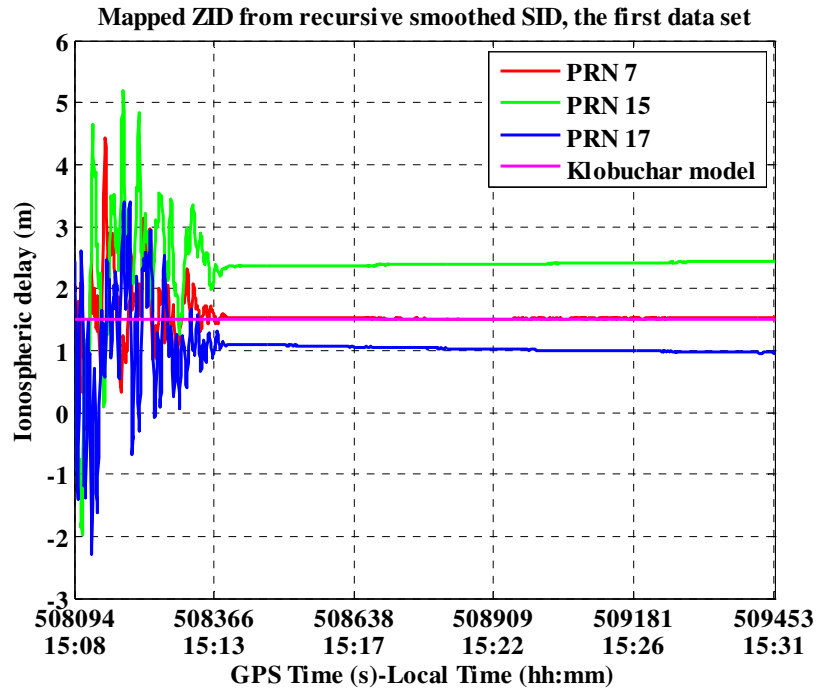


Figure 4.14: Mapped zenith ionospheric delays from the slant ionospheric delays shown in Figure 4.13

Table 4.2: RMS position errors for real-time processing of the first data set

Approaches		RMS Position Errors (m)		
		<i>Northing</i>	<i>Easting</i>	<i>Vertical</i>
<i>1 PRN</i>	<i>7</i>	1.1	0.8	1.2
	<i>15</i>	1.0	0.8	2.4
	<i>17</i>	1.1	0.8	1.7
<i>2 PRNs</i>	<i>7 and 15</i>	1.0	0.8	1.7
	<i>7 and 17</i>	1.1	0.8	1.4
	<i>15 and 17</i>	1.0	0.8	1.5
<i>3 PRNs</i>	<i>7, 15, and 17</i>	1.1	0.8	1.4

To validate the rare invariability of the receiver IFB and test the effectiveness of the proposed ionospheric delay estimation method sufficiently, a real-time processing is performed on the second data set with the elevation angles of the three L2C satellites shown in Figure 4.15. Figure 4.16 shows the recursive smoothed L1 SID estimates for the second data set. The same features as the recursive smoothed L1 SID estimates for the first data set can be observed. It is verified that the IFB has also been effectively removed by the IFB estimate obtained from the batch processing of the first data set. When these SIDs are mapped to zenith, as shown in Figure 4.17, it becomes clear that PRN 15 suffers from an IFB that is not well modeled by the adopted IFB estimate while the other two satellites have the ZID estimates very close to the Klobuchar model value. Again this could be due to either high code multipath during the 300 second smoothing interval or due to the satellite IFB or a combination of both effects.

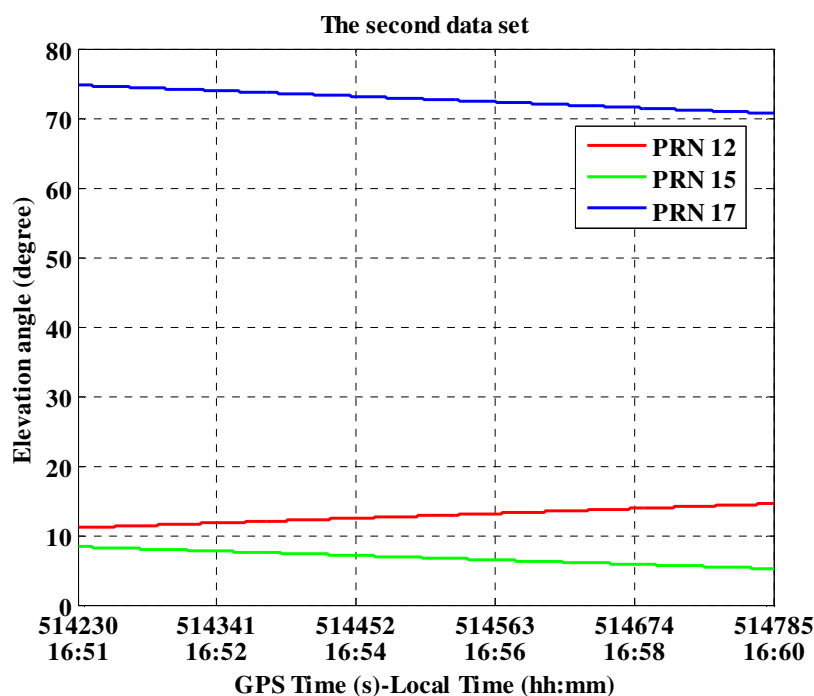


Figure 4.15: The elevation angles of the 3 L2C satellites in the second data set

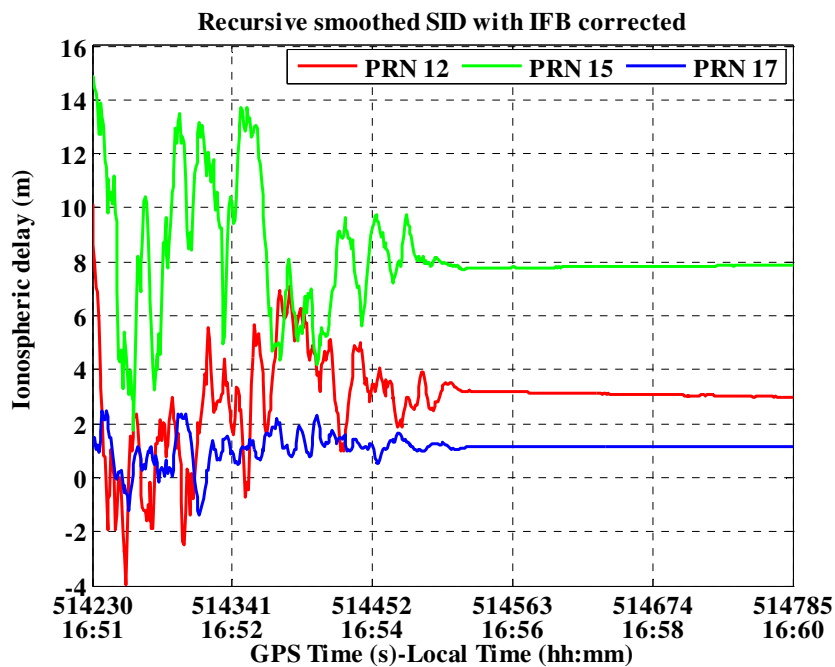


Figure 4.16: Recursive carrier smoothed slant ionospheric delays for the second dataset corrected with the inter-frequency biases obtained from the first dataset

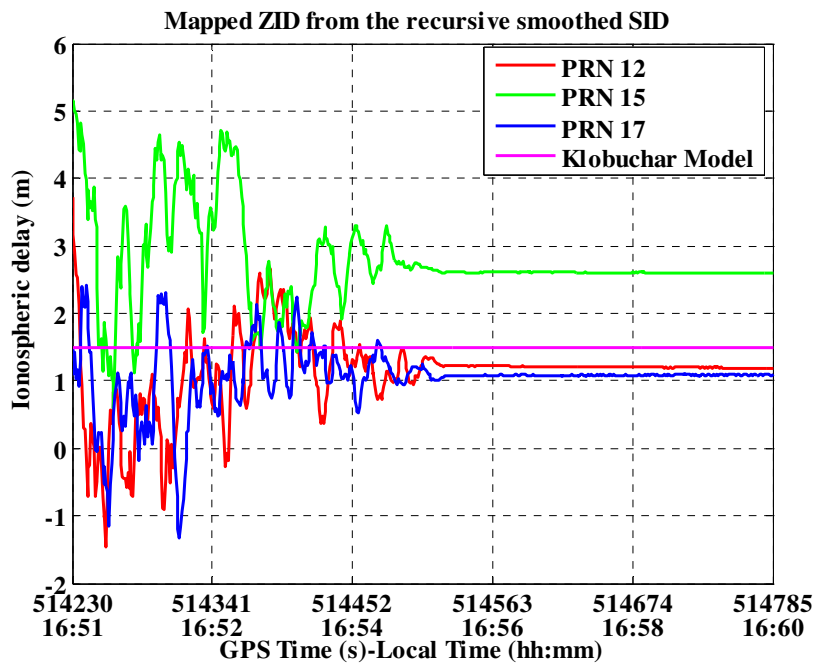


Figure 4.17: Mapped zenith ionospheric delays from the slant ionospheric delays shown in Figure 4.16

Despite the corrupted zenith delay estimate obtained from PRN 15, position solutions were obtained with this data set using all possible combinations of the three zenith delay estimates to generate ionospheric corrections. The results are summarized in Table 4.3. The first thing to note in these results is that all of the methods (with no corrections, Klobuchar model corrections, L1 C/A and L2C dual-frequency measurements derived zenith and slant corrections) resulted in similar levels of horizontal positioning accuracy. The major differences are evident in the vertical, as expected. In particular the uncorrected solution, and solutions obtained with corrections involving PRN 15 are particularly poor. This is not surprising since the zenith delay computed for PRN 15, using a single inter-frequency receiver bias, does not match well the Klobuchar model ionosphere estimate. Otherwise, the use of one or two zenith delays to generate slant ionosphere error corrections appears to provide position solutions with similar slightly improved vertical RMS errors.

Table 4.3: RMS position errors for real-time processing of the second data set

Approaches		RMS Position Errors (m)		
		<i>Northing</i>	<i>Easting</i>	<i>Vertical</i>
<i>No correction</i>		0.9	1.5	3.0
<i>Klobuchar model</i>		0.7	1.8	2.1
<i>1 PRN</i>	<i>7</i>	0.9	1.4	2.2
	<i>15</i>	0.8	1.4	3.9
	<i>17</i>	0.9	1.5	1.9
<i>2 PRNs</i>	<i>7 and 15</i>	0.8	1.4	2.4
	<i>7 and 17</i>	0.9	1.5	1.9
	<i>15 and 17</i>	0.8	1.4	2.2
<i>3 PRNs</i>	<i>7, 15, and 17</i>	0.9	1.4	1.9

4.4 Summary

In this chapter, the possibility of using partial availability of L2C signals to provide an ionospheric correction for the other satellites without L2C signal is investigated and demonstrated. The results presented in this chapter suggest that when limited number, e.g. 1, 2 or 3 L2C satellites, are available, a ZID can be estimated and thus can be used to generate slant ionospheric corrections for the L1 C/A pseudoranges. Use of these corrections provides positioning results with errors of the same order of magnitude as those obtained using the broadcast Klobuchar ionosphere model.

CHAPTER FIVE: TESTING RESULTS AND ANALYSIS OF CARRIER PHASE DGPS PRECISE POSITIONING

The proposed differential ZID method is tested in this chapter using real data. Results are presented comparing several scenarios involving a partial constellation of L2C signals versus a full constellation of L2P signals, contrasting the proposed differential ZID method with the well established SID method, L1/L2 dual-frequency observations processing while ignoring the ionosphere, and finally the L1 only case.

5.1 Data Collection

To test the feasibility of the proposed differential ZID method, data sets from three L2C capable static GPS stations, BAMF, UCLU, and PGC5 were used. All three stations are part of the Western Canada Deformation Array which is a permanent GPS tracker network established by the Geological Survey of Canada as part of the Canadian National Earthquake Hazards Program, and are located on Vancouver Island, in British Columbia, Canada as shown in Figure 5.1. These stations are equipped with dual-frequency, geodetic quality GPS receivers, here the Trimble NetRS receivers are deployed with the capability of outputting GPS L1 C/A, L2C, and L2P measurements simultaneously (Trimble 2005). These measurements are automatically forwarded to the International GNSS Service (IGS) and thus are downloadable from the IGS website. These three stations are selected due to their L2C signal continuously tracking capability as well as the interested baselines formed as indicated in Table 5.1 for single baseline testing. The BAMF-UCLU baseline and BAMF-PGC5 baseline refer to the relatively short and long baseline in this context, respectively.



Figure 5.1: The geography locations of the three selected stations as part of the Western Canada Deformation Array (NRCan 2010)

Table 5.1: Selected baselines

Baseline	Length (km)
BAMF-UCLU	31
BAMF-PGC5	125

Three 45 minutes data sets, sampled at 30 seconds interval, were collected on Jan. 11, 2010 from 09:23am to 10:09am local time from each of the three stations. The duration of the data sets is limited by the simultaneous availability of the L2C signals of interest. During the selected time segment, three L2C satellites, indicated by PRN 05, PRN 12, and PRN 29, are observable and usable simultaneously by all the three GPS stations. It is the time period that maximum number of L2C satellites is available for maximum time duration. The corresponding sky plot for BAMF station is shown in Figure 5.2, and the other two stations have very similar sky plots.

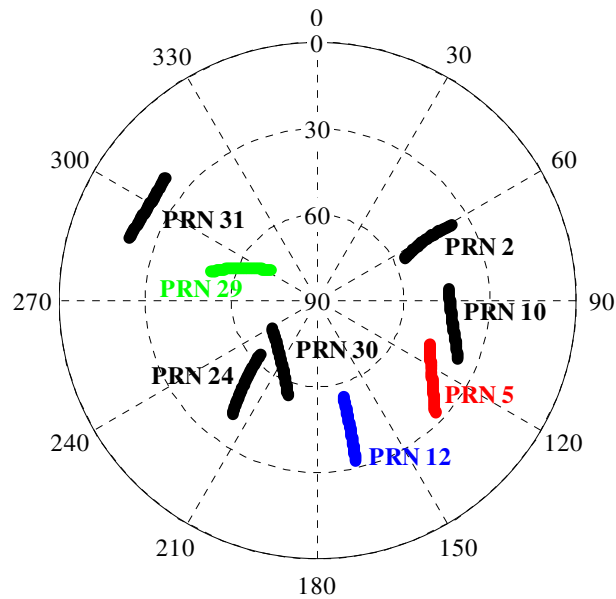


Figure 5.2: Sky plot for BAMF station

5.2 Data Processing and Results Interpretation Strategies

The following seven processing strategies were adopted for the testing and analysis:

- L1 only: single-frequency L1 C/A code and phase measurements are used;
- Strategy A: L1 and L2 (L2P or L2C) code and phase measurements are used, without estimating the ionospheric delay;
- Strategy B: L1 C/A and L2C code and phase measurements are used, with estimating the single differential ZID using the ionosphere-float approach;
- Strategy C: L1 C/A and L2P code and phase measurements are used, with estimating SID for each satellite using the ionosphere-float approach;

The L1 only strategy presented here is for comparison purposes since it does not have a second frequency observation for combination nor the capability of estimating the

ionospheric delay. Strategy A is adopted to show the benefit of the dual-frequency AR comparing to the L1 only strategy. Strategy C is trying to estimate the SID using SD instead of DD observations, where the SD SID states are modeled as a first order of Gauss-Markov process the same as to the differential ZID state in Strategy B. All of these strategies are then compared with Strategy B which targets to evaluate the capability of limited number of L2C measurements.

The cut-off elevation angle is set as 15° , and the C/N_0 threshold to admit usable measurements is 28 dB-Hz. The a-priori standard deviation for both L1 and L2 undifferenced pseudorange observation is chosen as 0.3 m, and 0.02 cycles for the L1 and L2 phases. Since all the data sets processed are static, and the position states are modeled as random walk process directly, a very small spectral density, $10^{-6} \text{ m}^2/\text{s}^2/\text{Hz}$, is assigned to the horizontal position states and an even smaller spectral density, $10^{-9} \text{ m}^2/\text{s}^2/\text{Hz}$, is assigned to the vertical position state. The SD clock bias state is also modeled as a random walk process, but large process noise, $10^4 \text{ m}^2/\text{s}^2/\text{Hz}$, is used to make it fully estimated, which is of significance for the SD functional model to be equivalent with the DD functional model. The ionospheric states, either single differential ZID state or multiple SID states, are modeled as first order of Gauss-Markov process with a correlation time constant, 200 seconds, and a spectral density of the driving white noise, $0.1 \text{ cm}^2/\text{s}$ (Liu et al 2003). The ambiguity validation strategy used is a combination of the ratio test with the threshold empirically chosen as 1.75, and the bootstrapping success rate with the threshold as 0.99995.

Two tests are performed to evaluate the positioning accuracy and AR performance. The entire 45 minutes data set is firstly processed estimating position and ambiguities along with ionospheric delay. The LAMBDA method is executed epoch-by-epoch for the whole data set ambiguity fixing. In this way, the effect of different observations and processing strategies on the float solution can be examined in terms of the ambiguity fixing performance representing by the percentage of correct fixing (PCF) and the percentage of incorrect fixing (PIF). PCF and PIF are defined as the percentage of epochs with correctly and incorrectly fixed integer ambiguity set respectively. Besides, an overall position error can be estimated and compared between different scenarios. Then, for the second test, the whole data set is divided into data batches with duration of five minutes and nine minutes and re-processed. At the beginning of each batch, the KF was re-initialized with the same parameters to avoid taking information from the processing of the previous observation span. Then the empirical PCF and PIF is calculated to evaluate the AR performance, which are defined as the percentage of batches with correct integer ambiguity set and with wrong integer ambiguity set among all the batches respectively. Note that the definitions for the PCF and PIF are different from the first test. Finally, the mean time to first fix (MTFF) is utilized to evaluate the AR speed, which is defined as the mean time to first fix to the correct integer ambiguity set of those correctly fixed batches. The time resolution of MTFF in this analysis, however, is limited to 30 seconds as this is the data rate.

5.3 Results and Analysis

The results are presented in different scenarios with the above listed processing strategies apply on different types of observations. For each scenario, the results of the short baseline are presented firstly and followed by the results of the long baseline.

5.3.1 Scenario with L1 Only

Since there is no dual-frequency measurements can be used to estimate the ionospheric errors, the broadcast Klobuchar ionosphere model is applied to the L1 Only Strategy to compensate the ionospheric errors. As an example, Figure 5.3 shows the estimated L1 float DD ambiguities of PRN 29 – PRN 30 (reference satellite) for the L1 Only Strategy with and without Klobuchar model compensation for the short baseline. The float DD ambiguities converge to their true integer values (all set as zeros during the analysis in this chapter). The convergence speed for the two cases are quite similar to each other, with the case where Klobuchar model applied provides slightly better accuracy of float DD ambiguity estimate. The corresponding ambiguity validation ratio test values and the bootstrapping SR are shown in Figure 5.4. Since the bootstrapping SR is a lower bound and is driven by the observation model only, it is not affected by the real DD ambiguity values. The two cases with and without Klobuchar model compensation share the same observation model, therefore they passed the threshold at the same time point. The ratio test is affected by the accuracy of the float DD ambiguities along the convergence. The ratio test values shown here indicate that the accuracy of the float DD ambiguities are close to each other for the two cases. The reason is that there is little difference between the ionospheric delays for the two stations, provided by the Klobuchar model.

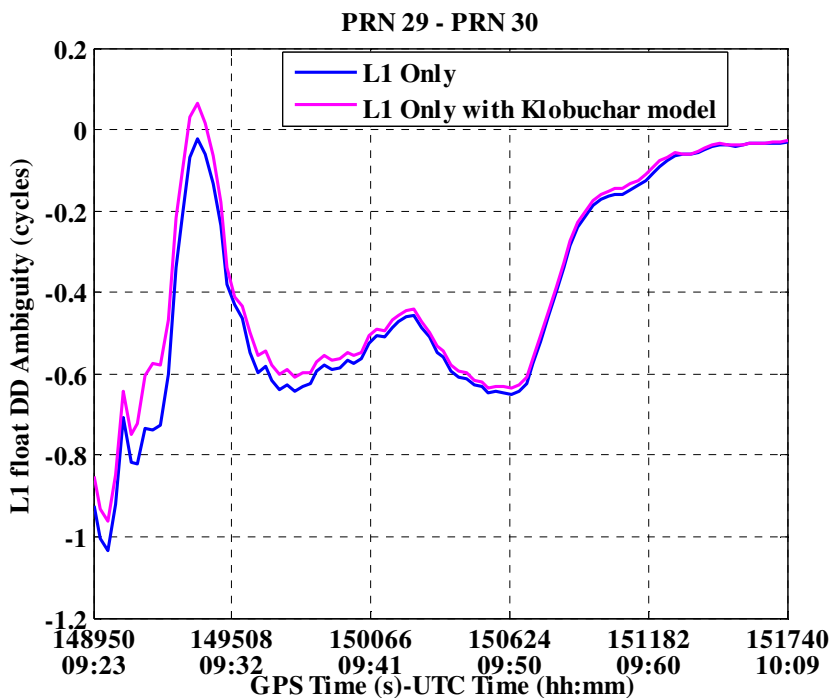


Figure 5.3: Estimated L1 float DD ambiguity of PRN 29 – PRN 30 for L1 Only Strategy, short baseline

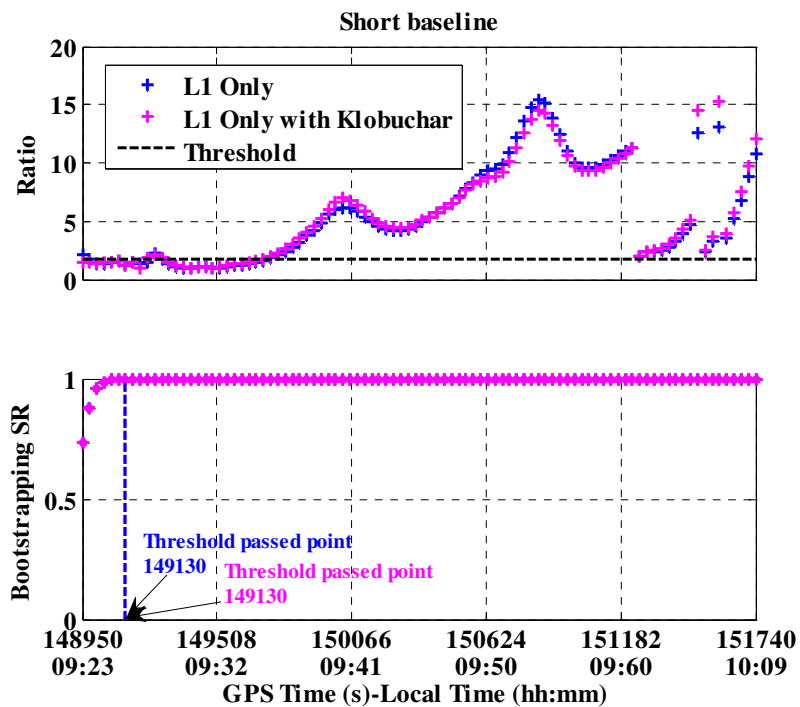


Figure 5.4: Ambiguity validation test values for L1 Only Strategy, short baseline

Figure 5.5 shows the position errors in northing, easting, and vertical components for the two cases with and without Klobuchar model. Note that the position errors obtained from the entire data set epoch-by-epoch processing is presented with a mixed of float solution and fixed solution if available, which is also the case for the remaining of this chapter. During the time period where the ambiguities is fixed, indicated in Figure 5.4, the fixed solution provides improved position accuracy over the float solution, which indicates correct AR. Table 2.1 summarizes the RMS of the position errors and the AR performance in terms of PCF and PIF. The statistics verify the impression that these two cases provide nearly the same position accuracy and AR performance with the stated reason that the differential Klobuchar ionospheric delay is almost negligible.

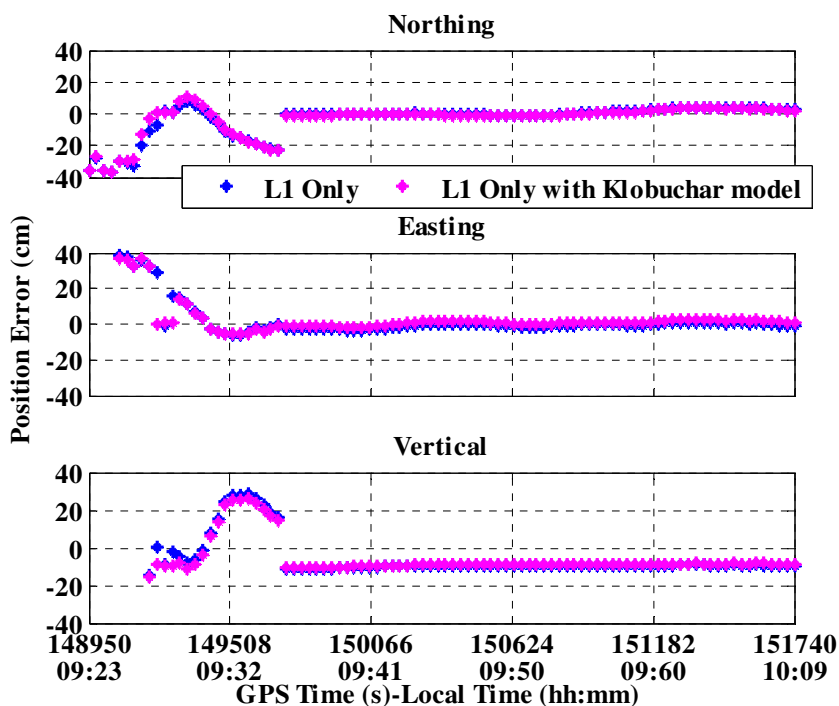


Figure 5.5: Position errors for L1 Only Strategy, short baseline

Table 5.2: The whole dataset position error RMS and AR performance for L1 Only Strategy, short baseline

Strategies	Position Error RMS (cm)			Ambiguity Fixing	
	<i>Northing</i>	<i>Easting</i>	<i>Vertical</i>	<i>PCF</i>	<i>PIF</i>
<i>L1 Only</i>	11	13	20	73.4%	0.0%
<i>L1 Only (Klobuchar)</i>	11	12	20	75.5%	0.0%

Table 5.3 further summarizes the AR performance of the data batches processing for the L1 Only Strategy with and without Klobuchar model compensation. There are 9 data batches or 5 data batches with the entire data set divided into intervals of 5 minutes or 9 minutes. Still, the Klobuchar model helps rarely in the data batches processing for evaluating the AR performance. Generally, with 210 - 300 minutes of time, a 30%-60% of PCF and only 10%-20% of PIF are observed for this data set for the L1 Only Strategy with the short baseline.

Table 5.3: Data batches AR performance, short baseline

Strategies	Span (minutes)	PCF	PIF	MTFF (s)
<i>L1 Only</i>	5	33.3%	0.0%	210
	9	40.0%	20.0%	210
<i>L1 Only (Klobuchar)</i>	5	44.4%	11.1%	210
	9	60.0%	20.0%	300

At this point, it may conclude that the Klobuchar model does not help with the carrier phase DGPS positioning accuracy and the L1 Only AR performance. However, there is another potential reason that the differential ionosphere error is trivial during this time

period with the short baseline. The following presents the same results analysis for the long baseline. Figure 5.6 shows up to 1 cycle of offset to the true value for the estimated L1 float DD ambiguity of PRN 29-PRN 30 at the beginning for the long baseline, which slowed down the convergence than that of the short baseline. This indicates the presence of non-negligible differential ionospheric error. After converging to the true value “0” at the time point between 150066 and 150624, the case with Klobuchar model compensation shows better accuracy than the case without it. This accuracy improvement directly affects the ambiguity validation. The ratio test values shown in Figure 5.7 indicate that the best ambiguity integer set candidate is more discernible to the second best ambiguity integer set candidate with the Klobuchar model applied in this long baseline data set. Moreover, the case with Klobuchar model compensation passes the ratio test threshold earlier than the case without it, which indicates faster float DD ambiguity convergence. The two cases for the L1 Only Strategy passed the bootstrapping SR threshold at the same time point again and also at the same time point as the short baseline, which addresses again that this ambiguity validation is model-driven and not affected by the real different ambiguity values as long as the observation model is the same. Figure 5.8 shows the position errors for the two cases of the L1 Only Strategy with the long baseline. The float solution takes longer time to converge than the short baseline. The integer ambiguities are fixed to the wrong values at the beginning for both cases, which deteriorates the position accuracy. Table 5.4 presents the RMS of the position errors and corresponding AR performance. The case with Klobuchar model applied provides slightly better AR performance in terms of the PCF (about 4% improvement) and the PIF (1%), which is not significant and is expected.

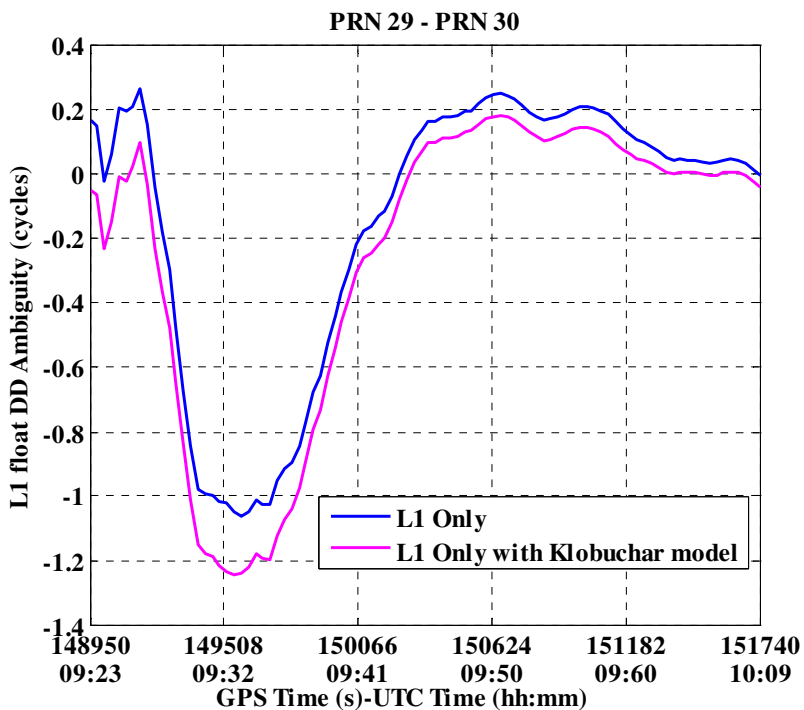


Figure 5.6: Estimated L1 float DD ambiguity of PRN 29 – PRN 30 for L1 Only Strategy, long baseline

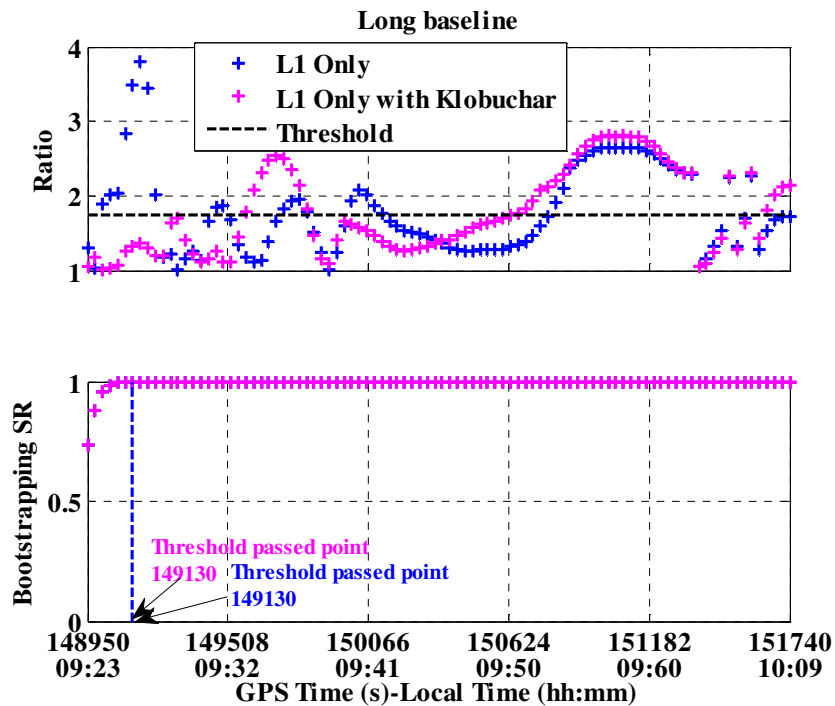


Figure 5.7: Ambiguity validation test values for L1 Only Strategy, long baseline

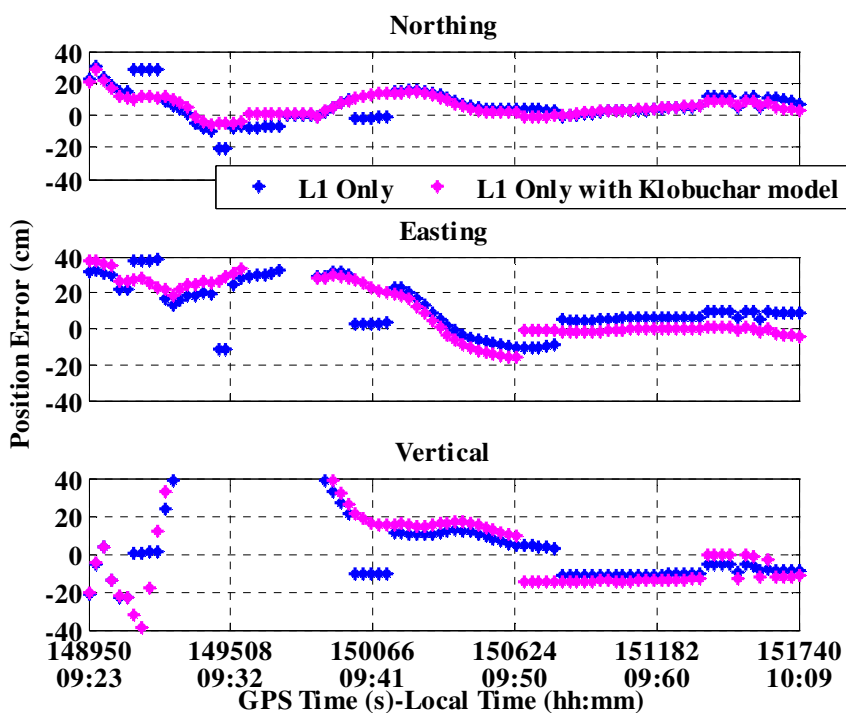


Figure 5.8: Position errors for L1 Only Strategy with and without Klobuchar model, long baseline

Table 5.4: The whole data set position error RMS and AR performance, long baseline

Strategies	Position Error RMS (cm)			Ambiguity Fixing	
	<i>Northing</i>	<i>Easting</i>	<i>Vertical</i>	<i>PCF</i>	<i>PIF</i>
<i>L1 Only</i>	11	26	37	27.7%	10.6%
<i>L1 Only (Klobuchar)</i>	8	31	39	31.9%	9.6%

Table 5.5 further summarizes the AR performance of the data batches processing. With the short period of time of the data batches and the presence of non-negligible differential ionospheric errors, any of the cases can fix the ambiguities correctly. The only finding is

that the case with Klobuchar model applied can lower down the PIF compared to the case without the Klobuchar model applied.

Table 5.5: Data batches AR performance, long baseline

Strategies	Span (minutes)	PCF	PIF	MTFF (s)
<i>L1 Only</i>	5	0.0%	44.4%	N/A
	9	0.0%	60.0%	N/A
<i>L1 Only (Klobuchar)</i>	5	0.0%	11.1%	N/A
	9	0.0%	40.0%	N/A

In summary, the L1 Only Strategy is adopted firstly to do the tests to obtain the performance of the single-frequency scenario for comparison with the other dual-frequency scenarios. In addition, the broadcasted Klobuchar model for single-frequency GPS positioning is utilized to provide ionospheric correction. However, as the results presented above, the Klobuchar model does not help with the positioning accuracy but slightly helps to improve the AR performance in both the short and long baseline scenarios, which is not of interest. In the remaining part of this chapter, the L1 Only Strategy refers to the case without the Klobuchar model ionospheric error compensation.

5.3.2 Scenario with L2P Measurements

To date, although requiring for expensive tracking techniques, the measurements were obtained from the L2P signal in addition to L1 measurements for civil dual-frequency applications. The performance of the L2P signal is limited due to the tracking techniques used in the civil receivers, but there are advantages to employ a second frequency signal

compared to the single-frequency L1 only scenario. In this thesis, the L2P measurements are also used to perform the dual-frequency processing and the corresponding performance is obtained for comparison sense. Figure 5.9 shows the estimated L1 float DD ambiguity of PRN 29-PRN 30 in dual-frequency Strategy A and Strategy C compared to the L1 Only Strategy for the short baseline. Strategy A provided similar estimate to the L1 Only Strategy but slower convergence since more states are estimated. Strategy C provided a very different estimate which is biased from the true value since it parameterized a state to estimate the negligible differential ionospheric errors in the short baseline, and this state is estimated as a bias which is hardly separable with the SD clock offset without sufficient observability. Figure 5.10 shows the ambiguity validation test results for this short baseline with Strategy A and Strategy C. It is found that Strategy C can not pass either the ratio test or the bootstrapping SR test with the L1 C/A and the L2P dual-frequency measurements with the estimation of a SD SID for each satellite. The reason is that the SD ionospheric delay is negligible for this short baseline during this time period, while the filter is trying to estimate it as a bias state along with the SD clock bias and SD ambiguity. The observation model is not valid anymore with the SD ionospheric delay explicitly modeled in this case making the model-driven bootstrapping SR lower than the threshold. As stated, Strategy C works equivalently as the positioning approach using the ionosphere-free phase combination where the inherent integer property of the DD ambiguity may not exist anymore. Besides, the float DD ambiguities are biased to weaken the ambiguity fixing and the ratio test for ambiguity validation before sufficient observability to separate the SD SID state and the SD clock offset state or the SD ambiguity state.

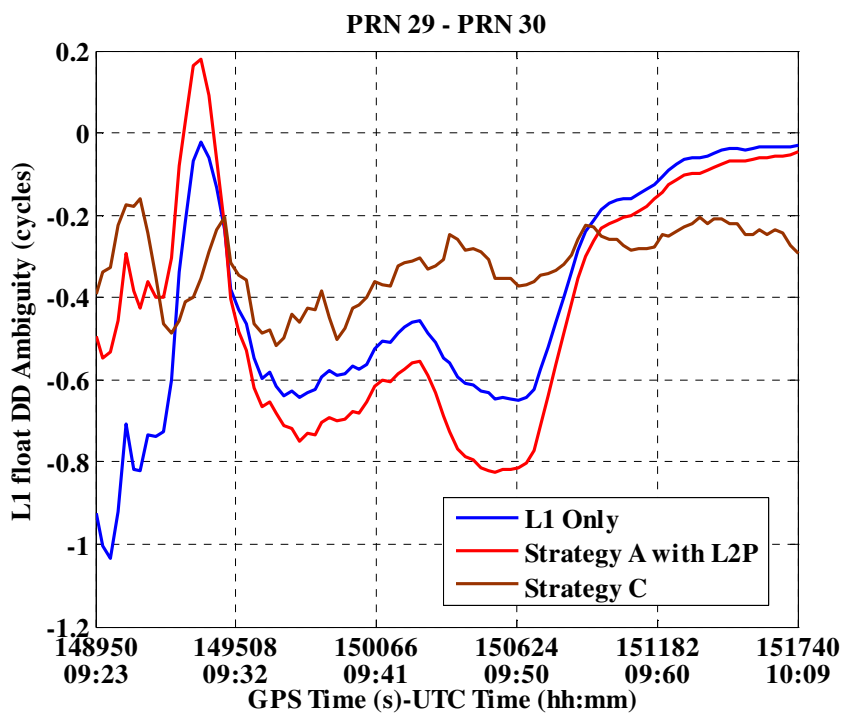


Figure 5.9: Estimated L1 float DD ambiguity of PRN 29 – PRN 30 for Strategy A and Strategy C using L2P measurements, short baseline

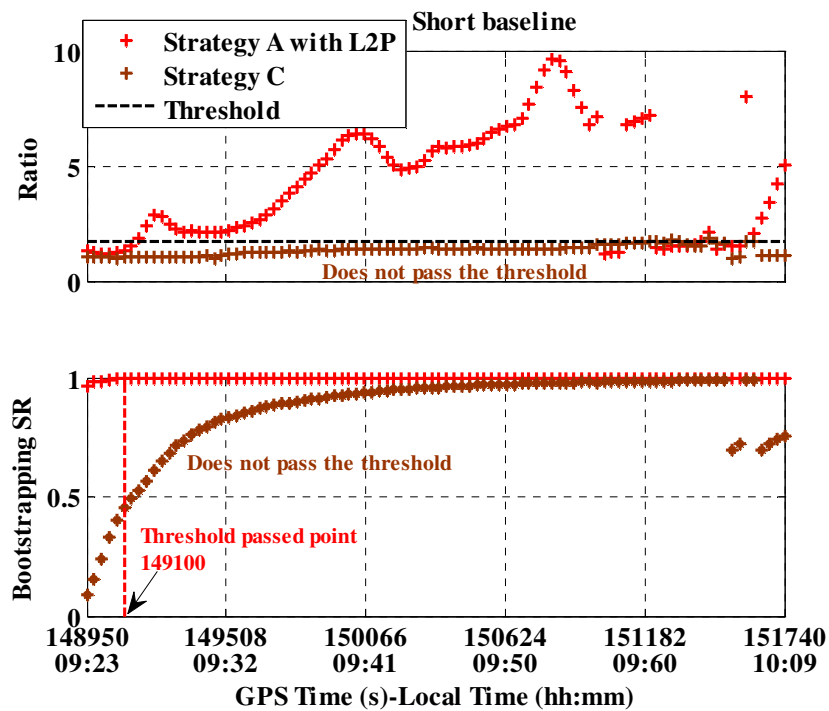


Figure 5.10: Ambiguity validation test values for Strategy A and Strategy C using L2P measurements, short baseline

Figure 5.11 shows the position errors for Strategy A and Strategy C using the L1 C/A and the L2P dual-frequency measurements. Strategy A provided much faster convergence speed of the float solution as compared to the L1 Only Strategy shown in Figure 5.5 without improving the convergence of the L1 float ambiguity individually. As a result, the ambiguities are fixed and the fixed solution is obtained much faster. This is the benefit obtained from the dual-frequency AR using the LAMBDA method which automatically forms widelane ambiguity that decorrelates and has better accuracy than the L1 and L2 ambiguity alone. Table 5.6 summarizes the statistics for the positioning accuracy as well as the AR performance. The PCF is about 4% higher than that of L1 Only Strategy, The horizontal RMS position accuracy is thus improved for several centimetres overall for more epochs of ambiguities are fixed correctly.

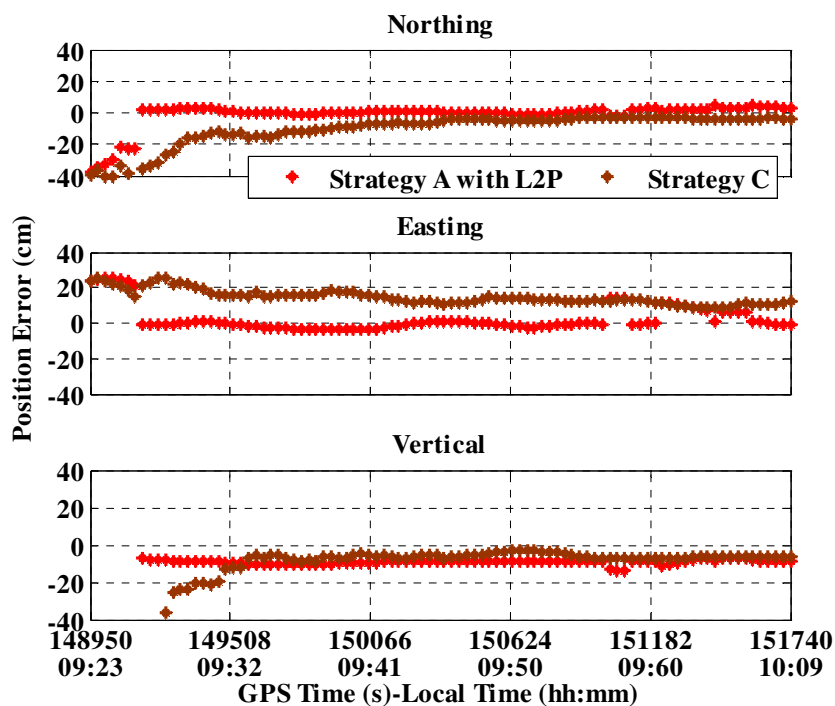


Figure 5.11: Position errors for Strategy A and Strategy C using L2P measurements, short baseline

Table 5.6: The whole data set position error RMS and AR performance for Strategy A and Strategy C using L2P measurements, short baseline

Strategies	Position Error RMS (cm)			Ambiguity Fixing	
	<i>Northing</i>	<i>Easting</i>	<i>Vertical</i>	<i>PCF</i>	<i>PIF</i>
<i>Strategy A (L2P)</i>	8	8	21	77.7%	0.0%
<i>Strategy C</i>	15	15	27	0.0%	0.0%

Table 5.7 presents the AR performance for the divided data batches with Strategy A only, since Strategy C can not fix ambiguity at all. Comparing to the L1 Only Strategy, the most improvement is obtained on the MTFE that reduced from 210-300 seconds to 90-120 seconds, which is the benefit from the dual-frequency AR over the single-frequency AR theoretically developed and now practically proved with real data. The implicitly formed widelane ambiguity at the initial stage followed by the optimal combination of the dual-frequency phase ambiguity during the LAMBDA decorrelation process provides much more accurate ambiguity than the L1 ambiguity alone.

Table 5.7: Data batches AR performance with Strategy A using L2P measurements, short baseline

Strategies	Span (minutes)	PCF	PIF	MTFE (s)
<i>Strategy A (L2P)</i>	5	33.3%	11.1%	120
	9	60.0%	0.0%	90

The following presents the results obtained from Strategy A and Strategy C using the L1 C/A and the L2P dual-frequency measurements for the long baseline. As shown in Figure 5.12, a more than 1.5 cycles offset for the L1 float DD ambiguity estimate from Strategy A and about 1 cycle offset for the L1 Only Strategy are observed until sufficient convergence is obtained at nearly the same time point for the two strategies. This indicates the float solution convergence suffers from the remaining differential ionospheric error for the two strategies and a slower convergence for Strategy A as more states are estimated. Afterwards, the two strategies provided similar L1 float DD ambiguity estimates. Note that Strategy C provided the best L1 float DD ambiguity estimate among these three strategies with faster convergence at the beginning. However, it is also observed that Strategy C needs longer time to obtain float ambiguity estimates with the accuracy achieved by Strategy A and the L1 Only Strategy at the end of the data set. This means that longer convergence time is needed for Strategy C to have the sufficient observability to separate the SD SID state with the SD clock offset and the SD ambiguity states. The observation model for Strategy C can not provide the float ambiguity estimates with the accuracy to be validated by the bootstrapping SR approach during the entire data set, as shown in Figure 5.13. With the presence of the differential ionospheric errors for this long baseline, Strategy C can pass the ratio test for some of the epochs at the end of the data set, which may indicate ambiguity fixing if the bootstrapping SR test is not combined to the ratio test. Note that Strategy A passes the bootstrapping SR threshold at the same time point for both the short and long baseline scenarios. It is addressed again that the bootstrapping SR validation approach is observation model-driven and not affected by the real ambiguity values.

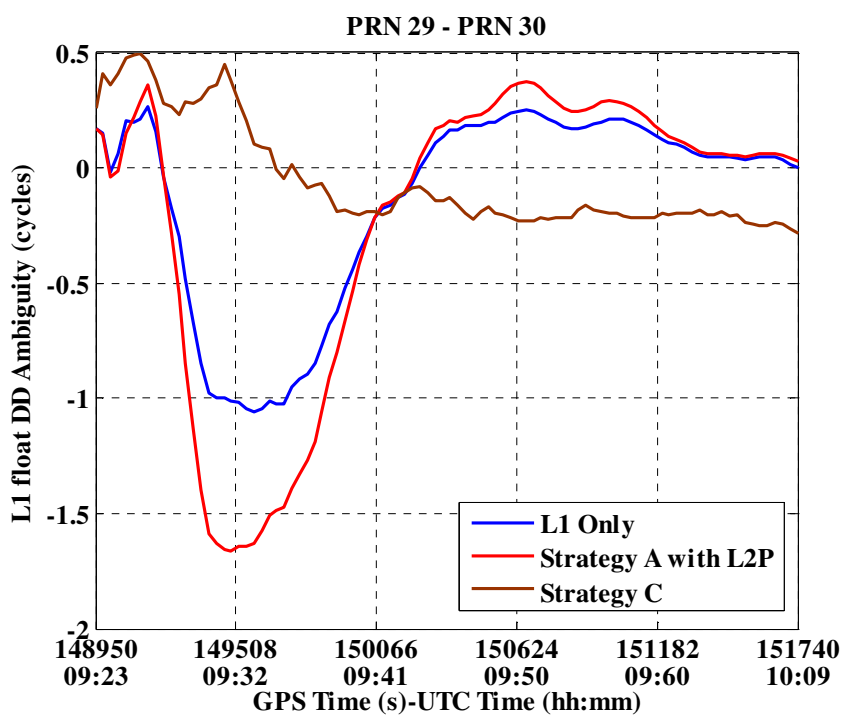


Figure 5.12: Estimated L1 float DD ambiguity of PRN 29 – PRN 30 for Strategy A and Strategy C using L2P measurements, long baseline

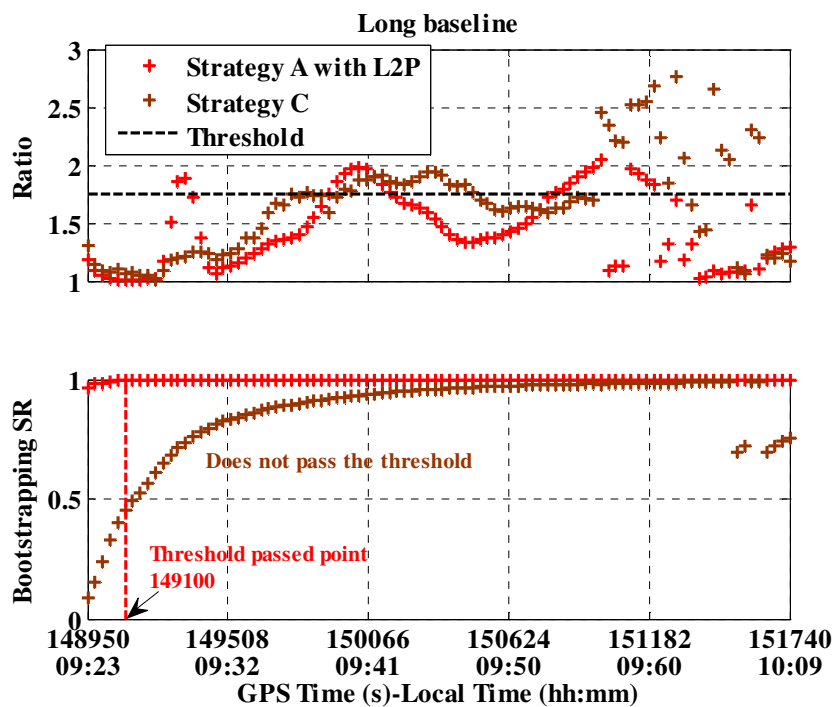


Figure 5.13: Ambiguity validation test values for Strategy A and Strategy C using L2P measurements, long baseline

Figure 5.14 shows the time series of position errors for the long baseline. Strategy A provides relatively larger position errors trying to fix the L1 and L2 phase ambiguities without estimating the ionospheric error, while Strategy C provides relatively small and smoothing position errors along with the time only with the float solution. Table 5.8 summarizes the statistics for the RMS of the position errors as well as the AR performance. Strategy A provides similar RMS of position errors compared to the L1 Only Strategy and about 8% lower PIF but about 7% lower PCF. It is reasonable for these two strategies to have such performance in a 125 km long baseline scenario. Meanwhile, it is found that Strategy C provides improved centimetre level of horizontal accuracy and reduced vertical error in terms of RMS, comparing to all the other cases for this long baseline scenario, though no ambiguity is ever fixed.

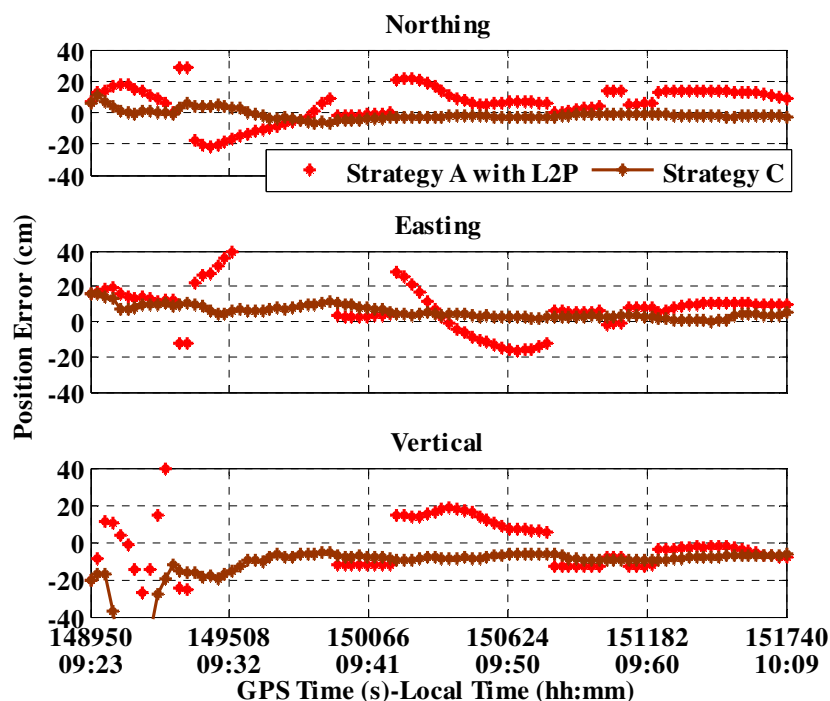


Figure 5.14: Position errors for Strategy A and Strategy C using L2P measurements, long baseline

Table 5.8: The whole data set position error RMS and AR performance for Strategy A and Strategy C using L2P measurements, long baseline

Strategies	Position Error RMS (cm)			Ambiguity Fixing	
	<i>Northing</i>	<i>Easting</i>	<i>Vertical</i>	<i>PCF</i>	<i>PIF</i>
<i>Strategy A (L2P)</i>	12	21	42	20.2%	2.1%
<i>Strategy C</i>	3	6	16	0.0%	0.0%

With the presence of non-negligible ionospheric error in this long baseline scenario, the AR performance of the data batches can not benefit from Strategy A using additional L2P measurements where the ionospheric error is not estimated or compensated, comparing to the L1 Only Strategy. The statistics are listed in Table 5.9.

Table 5.9: Data batches AR performance with Strategy A using L2P measurements, long baseline

Strategies	Span (minutes)	PCF	PIF	MTFF (s)
<i>Strategy A (L2P)</i>	5	0.0%	11.1%	N/A
	9	0.0%	40.0%	N/A

In summary, this section evaluated the performance of dual-frequency AR with the full constellation of L2P signals for comparison purpose. Strategy A can provide horizontal accuracy and also MTFF improvements over the L1 Only Strategy for the short baseline where the differential ionospheric residual is negligible. Strategy C provides the best position accuracy in the float solution without the ability to fix ambiguity in the long

baseline scenario while deteriorates the solution for the short baseline scenario with over-estimated differential ionospheric residual.

5.3.3 Scenarios with partial availability of L2C satellites

This section discusses the benefit of having partial availability of L2C measurements as compared to the previously discussed single-frequency L1 only scenario and the dual-frequency scenario with full constellation of L2P measurement. The discussion starts with the scenario with 1 L2C satellites in addition to full constellation of L1 C/A measurements followed by scenarios with 2 and 3 L2C satellites available.

First of all, as the proposed differential ZID method for the differential ionospheric error estimation with partial availability of the L2C measurements, Strategy B is applied to estimate a single differential ZID state along with the position states, the SD clock bias state, and other SD ambiguity states. For the following scenarios with 1, 2, or 3 L2C satellites, the estimated differential ZIDs of the float solution are shown in Figure 5.15 and Figure 5.16 for the short and long baseline respectively, comparing to the estimates from the GIM. Only one example estimate is selected to shown here for the 1 (e.g. with PRN 29) or 2 L2C (e.g. with PRN 29 & 05) satellites scenario respectively. The differential ZID obtained from the GIM shows negligible ionospheric residual exists for the two stations for the short baseline, while the estimates in this work are in the sub-decimetre level. The differential ZID from the GIM is about 5 – 15 cm, while the estimates in this work are nearly in the same level. The impact of these estimated differential ZID will be discussed in the following.

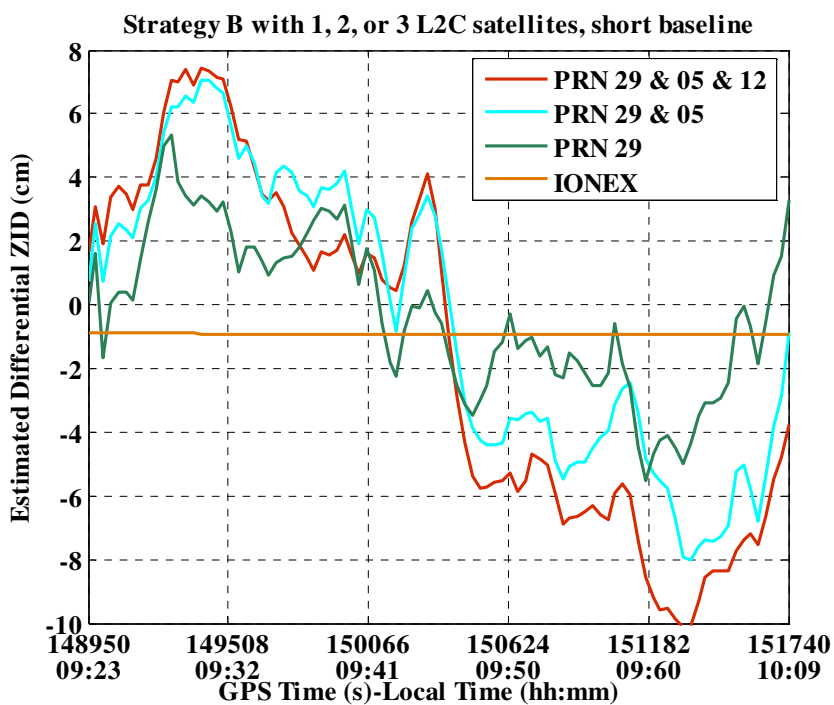


Figure 5.15: Estimated differential ZID from IONEX map and Strategy B with 1, 2, or 3 L2C satellites available, short baseline

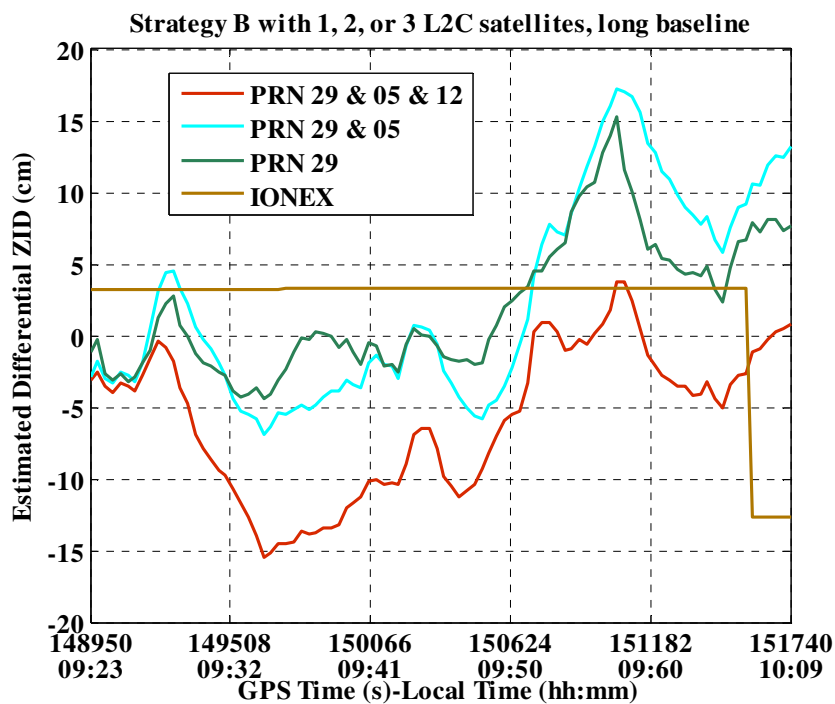


Figure 5.16: Estimated differential ZID from IONEX map and Strategy B with 1, 2, or 3 L2C satellites available, long baseline

Scenario with 1 L2C satellite

As the results shown in the scenario with full availability of L2P measurements, there is no much difference for the float solution whether the remaining differential ionospheric error is estimated or not for the short baseline, although the AR performance is improved to some extent. Accordingly, for the scenario with only 1 L2C satellite, where no L2C DD ambiguity could be formed, Strategy A and Strategy B will not obtain much different position solution and AR performance from the L1 Only Strategy. As shown in Figure 5.17, there is not much difference for the L1 float DD ambiguity estimates except that the estimate from Strategy A with L2P measurements has more cycles offset to the true value during the convergence due to that more states are estimated. In Figure 5.18, the bootstrapping SR values show that slight time delay for Strategy B to pass the threshold than that of Strategy A, with only one additional differential ZID state added in the observation model. Besides, the observability of the differential ZID state is better than the observability of the SD SID state in Strategy C, , when estimating the SD clock error state and SD ambiguity state at the same time, provided by the variability of the elevation angle and the corresponding mapping value. The corresponding bootstrapping SR is shown in Figure 5.10. The ratio test shows that Strategy A with measurements from 1 additional L2C satellite is quite similar to the L1 Only Strategy, which is expected since no L2C DD ambiguity is added. Strategy B provides more conservative ratio test results due to the one more estimated differential ZID state.

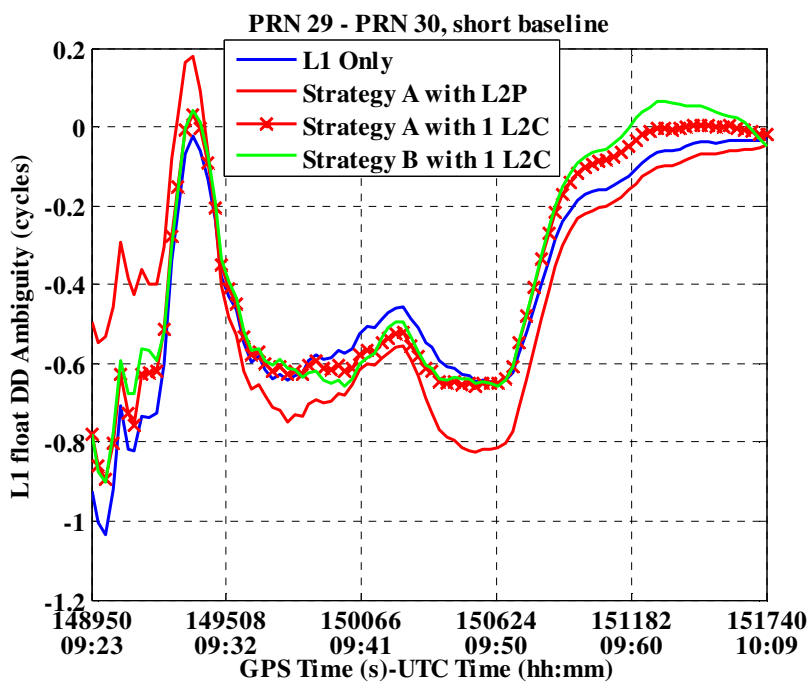


Figure 5.17: Estimated L1 float DD ambiguity of PRN 29 – PRN 30 for Strategy A and B with 1 L2C satellite (PRN 29) available, short baseline

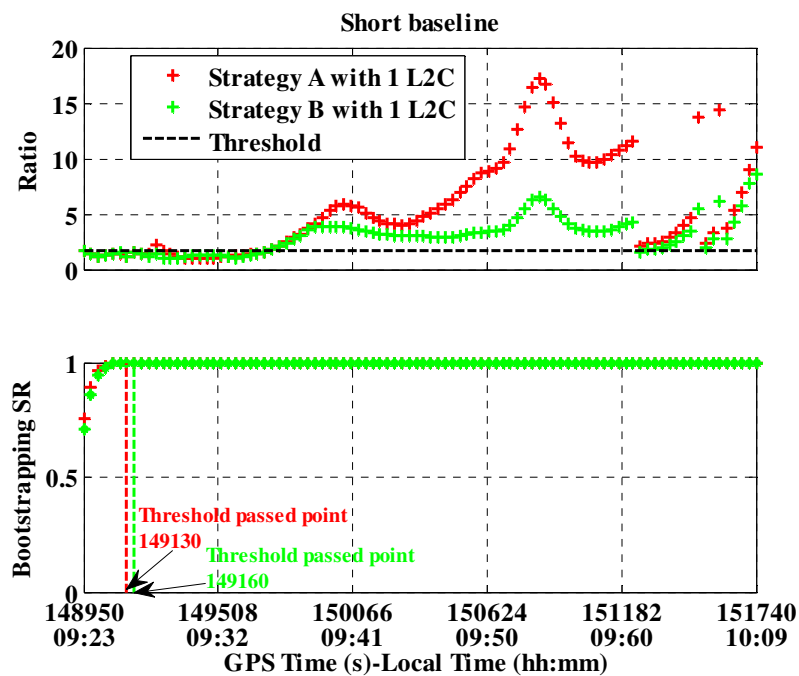


Figure 5.18: Ambiguity validation test values for Strategy A and Strategy B with 1 L2C satellite (PRN 29) available, short baseline

Figure 5.19 shows the position errors for Strategy A and Strategy B with one additional L2C satellite, and still quite close results were obtained due to the nearly negligible differential ionospheric residual for this short baseline. It is found that these results are quite close to the results for the L1 Only Strategy without any benefit obtained from Strategy A by adding one L2C measurement and from Strategy B by adding one L2C measurement as well as estimating the differential ionospheric errors. The statistics shown in Table 5.10 also verified the same conclusion. For the AR performance, Strategy B tended to be conservative in the ratio test and thus provided little lower PCF but reduced PIF at the same time.

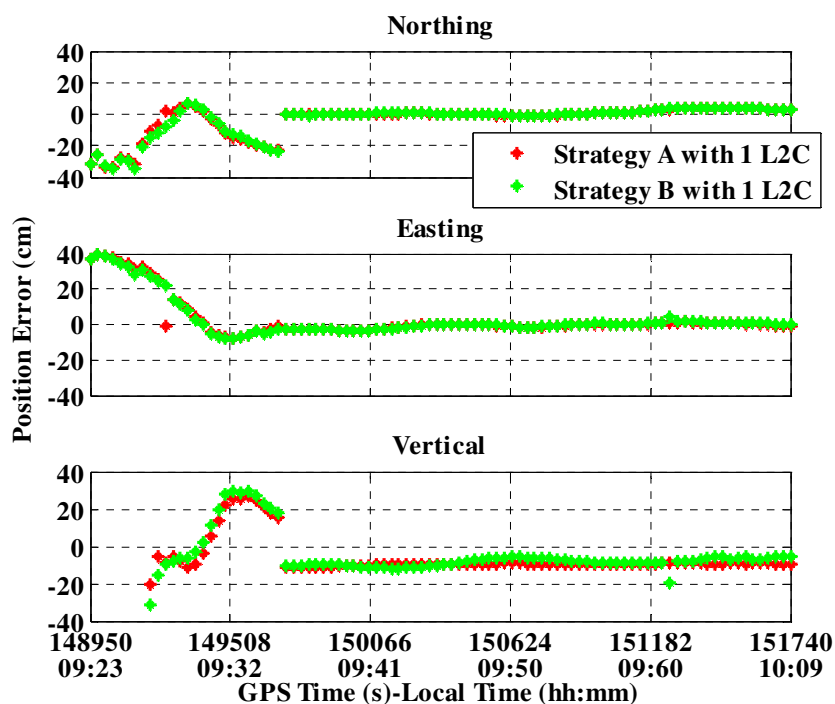


Figure 5.19: Position errors for Strategy A and B with 1 L2C satellite (PRN 29) available, short baseline

Table 5.10: The whole dataset position error RMS and AR performance with 1 L2C satellite available, short baseline

PRN	Strategies	Position Error RMS (cm)			AR	
		<i>Northing</i>	<i>Easting</i>	<i>Vertical</i>	<i>PCF</i>	<i>PIF</i>
12	<i>Strategy A</i>	7	14	27	74.5%	1.1%
	<i>Strategy B</i>	7	13	25	71.3%	0.0%
29	<i>Strategy A</i>	10	12	20	73.4%	0.0%
	<i>Strategy B</i>	11	12	21	70.2%	0.0%
05	<i>Strategy A</i>	10	12	19	73.4%	0.0%
	<i>Strategy B</i>	10	12	20	63.8%	0.0%

The following shows the results and analysis for the scenario with only one L2C satellite available for the long baseline. This time, as shown in Figure 5.20, Strategy B brought the benefit from estimating the differential ionospheric error by a single differential ZID state as compared to the L1 Only Strategy and Strategy A with L2P measurements. As shown in Figure 5.21, the bootstrapping SR test results for the long baseline are the same as the short baseline since the observation model is the same. The ratio test result of Strategy A has rare difference from the L1 Only Strategy for the only addition of one L2C measurements. The ratio test result of Strategy B shows that most of the ambiguities can not be fixed and shows the conservative of this strategy which tends to lower down the PIF of ambiguity fixing.

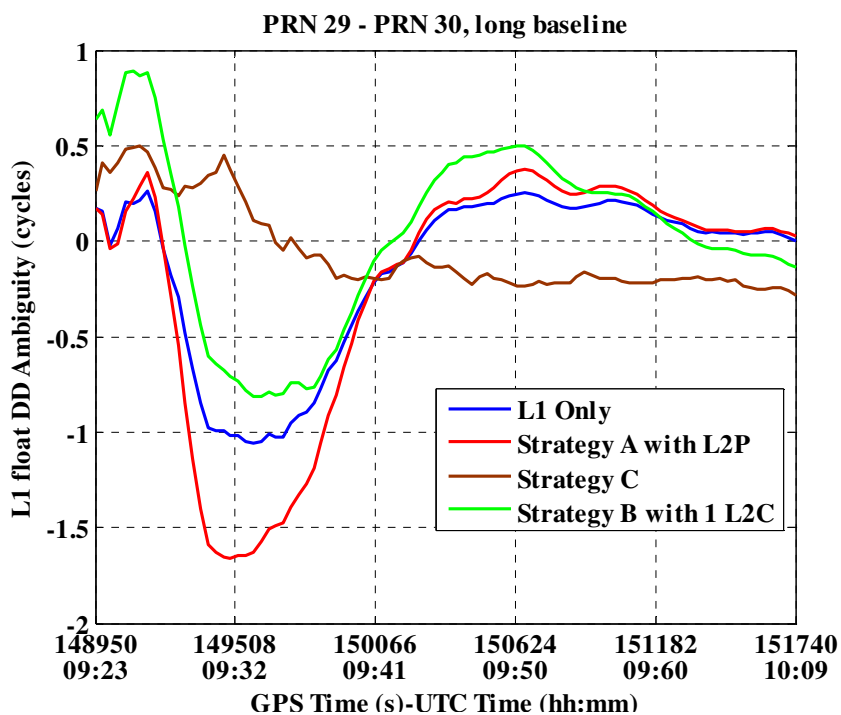


Figure 5.20: Estimated L1 float DD ambiguity of PRN 29 – PRN 30 for Strategy A and B with 1 L2C satellite (PRN 29) available, long baseline

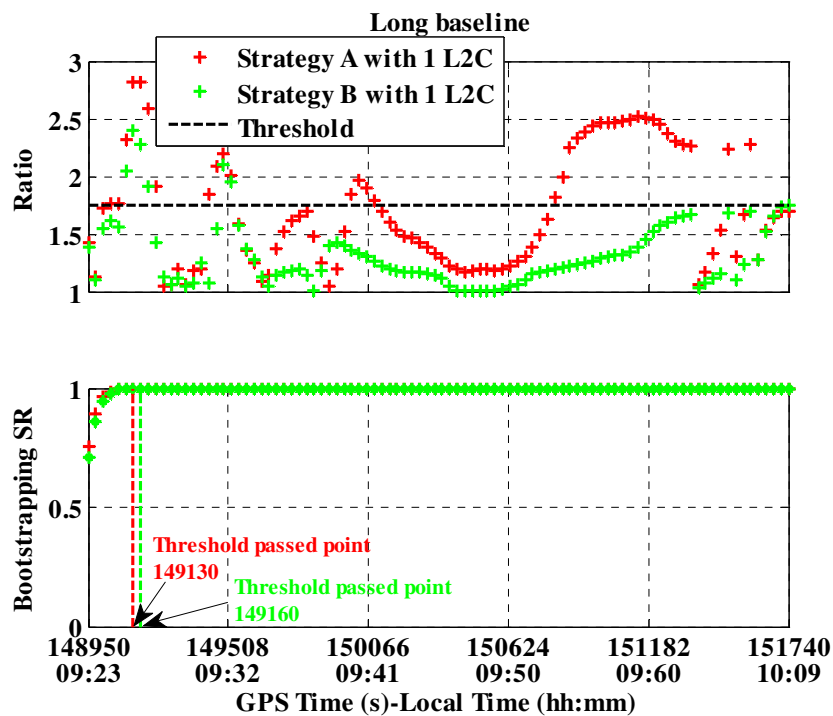


Figure 5.21: Ambiguity validation test values for Strategy A and Strategy B with 1 L2C satellite (PRN 29) available, long baseline

Figure 5.22 shows the position errors along with time for having one additional L2C satellite PRN 29. Started at the time point of 15006, the float solution converges sufficiently for the ambiguities to be fixed correctly, which is also indicated in Figure 5.20. Before this point, all the ambiguities are fixed to the wrong integers. Strategy A and Strategy B presented the similar position solution trend. The statistics in Table 5.11 show that the position accuracy improvement obtained from Strategy B comes out of the lower PIF other than higher PCF as compared to Strategy A. In fact, Strategy B provides lower PCF than Strategy A with any one of the three available L2C satellite. Comparing to the L1 Only Strategy, Strategy A has no obvious advantage since the only difference is the added one L2C measurement. The advantage of Strategy B over Strategy A also holds for over the L1 Only Strategy.

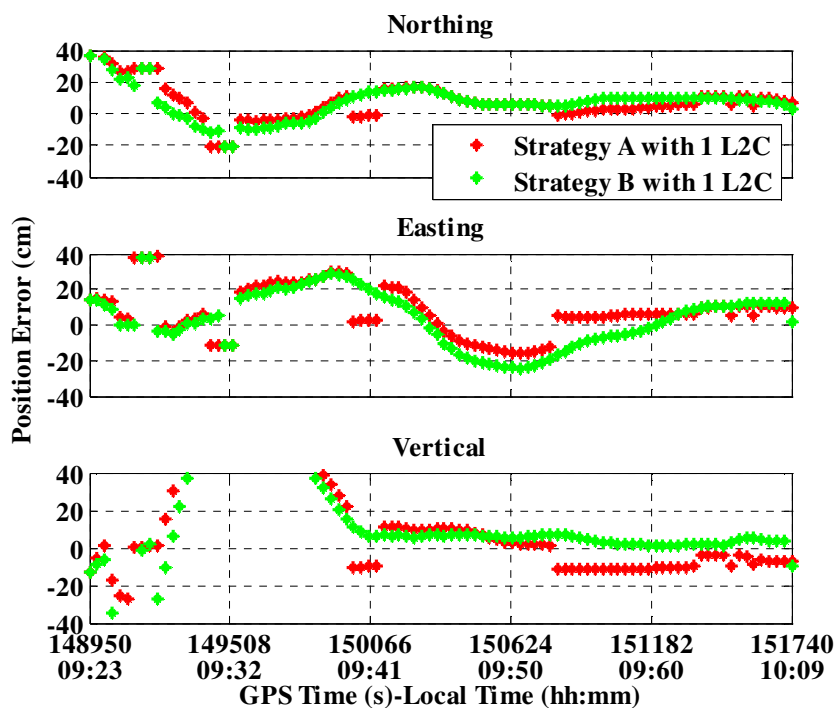


Figure 5.22: Position errors and number of fixed ambiguities, Strategy A and B with 1 L2C satellite (PRN 29) available, long baseline

Table 5.11: The whole dataset position error RMS and AR performance with 1 L2C satellite available, long baseline

PRN	Strategies	Position Error RMS (cm)			AR	
		<i>Northing</i>	<i>Easting</i>	<i>Vertical</i>	<i>PCF</i>	<i>PIF</i>
12	<i>Strategy A</i>	10	28	39	21.3%	11.7%
	<i>Strategy B</i>	11	27	37	14.9%	11.7%
29	<i>Strategy A</i>	14	16	36	26.6%	8.5%
	<i>Strategy B</i>	13	16	29	1.1%	4.3%
05	<i>Strategy A</i>	11	31	52	28.7%	16.0%
	<i>Strategy B</i>	15	28	25	2.1%	1.1%

In summary, with only one additional L2C satellite, a single differential ZID state can be estimated along with the position states, the SD clock bias state, and the other SD L1 ambiguity states, and no L2C DD ambiguity can be formed. The benefit of estimating this single differential ZID state tends to reduce the PIF, but at the same time to lower the PCF on the other hand for both the short and long baselines as compared to the case without estimating any remaining ionospheric residual. The benefit for the position accuracy derives from the lower PIF other than higher PCF.

Scenario with two L2C Satellites

For a data set with three L2C satellites available, there are three cases for any two of them to form one scenario. Table 5.12 summarizes the statistics of the position errors and AR performance of using additional measurements from 2 L2C satellites. As stated for the scenario with only 1 L2C satellite available, Strategy B tends to reduce PIF but also

slight lower PCF, which also can be observed from those statistics for the short baseline scenario. Comparing to the L1 Only Strategy, no improvement on the position accuracy and the AR performance has been observed for the entire data processing in the short baseline scenario.

Table 5.12: The whole dataset position error RMS and AR performance with 2 L2C satellites available, short baseline

PRN	Strategies	Position Error RMS (cm)			Ambiguity Fixing	
		<i>Northing</i>	<i>Easting</i>	<i>Vertical</i>	<i>PCF</i>	<i>PIF</i>
12&29	<i>Strategy A</i>	6	11	25	77.7%	0.0%
	<i>Strategy B</i>	6	11	26	71.3%	0.0%
12&05	<i>Strategy A</i>	7	12	24	71.3%	0.0%
	<i>Strategy B</i>	7	12	25	62.8%	0.0%
05&29	<i>Strategy A</i>	11	12	22	70.2%	1.1%
	<i>Strategy B</i>	10	11	21	70.2%	0.0%

Table 5.13 shows the AR performance statistics for data batches with 2 L2C satellites available, where one additional L2C DD ambiguity could be formed to join in the ambiguity fixing process with other L1 DD ambiguities. No benefit has been obtained using Strategy B over Strategy A, although the PIF is reduced from 22.2% to 11.1% for 9 data batches processing. Comparing to the L1 Only Strategy, Strategy A provides similar PCF and PIF but shows its advantage on the MTFE. As described theoretically for the LAMBDA method, dual-frequency AR outperforms L1 only AR with the ability to form widelane ambiguity which could be more easily and faster resolved than the L1 or L2 ambiguity individually.

Table 5.13: Data batches AR performance with 2 L2C satellites (PRN 29 & 05) available, short baseline

PRN	Strategies	Span (minutes)	PCF	PIF	MTFF (s)
29 & 05	Strategy A	5	33.3%	22.2%	180
		9	40.0%	20.0%	180
	Strategy B	5	33.3%	11.1%	180
		9	20.0%	20.0%	120

Comparing to the ratio test value shown in Figure 5.21, Strategy A, shown in Figure 5.23, becomes more conservative in fixing the ambiguities with two L2C satellites involved than with only one, which can be explained by the more accurate WL ambiguities formed during the decorrelation of the LAMBDA method with one L2C DD ambiguity added.

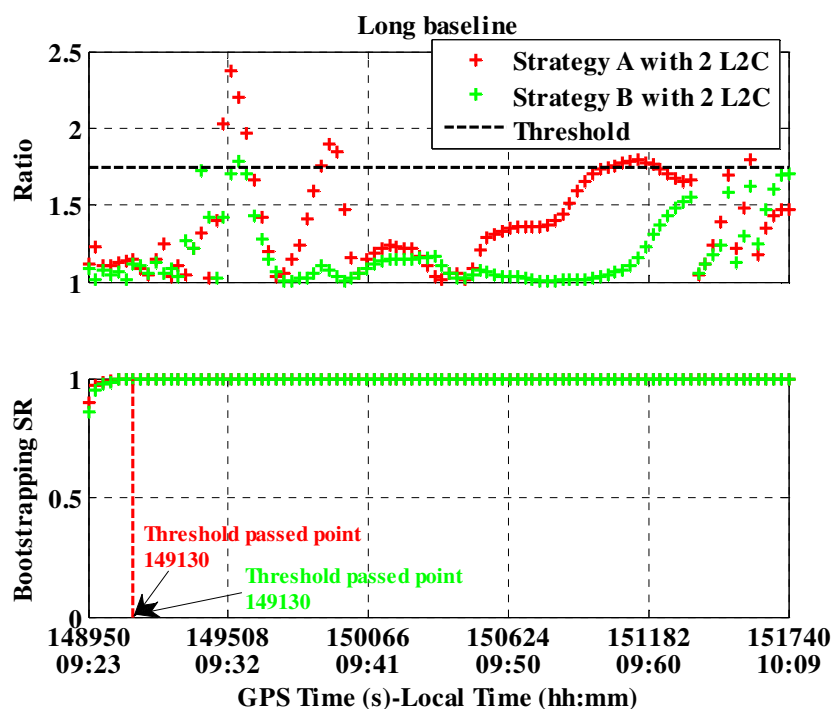


Figure 5.23: Ambiguity validation test values for Strategy A and Strategy B with 2 L2C satellite (PRN 29 & 5) available, long baseline

As shown in Figure 5.24, the ambiguities of some of the epochs were fixed before the time point of 150066 when the float solution is not sufficiently converged. Thus, there is large possibility to fix the ambiguities wrong. The fact that the vertical component of the position errors is very large during that period of time identified the possibility. Around the time point of 151182, Strategy A provided a better position solution than Strategy B with those ambiguities correctly fixed.

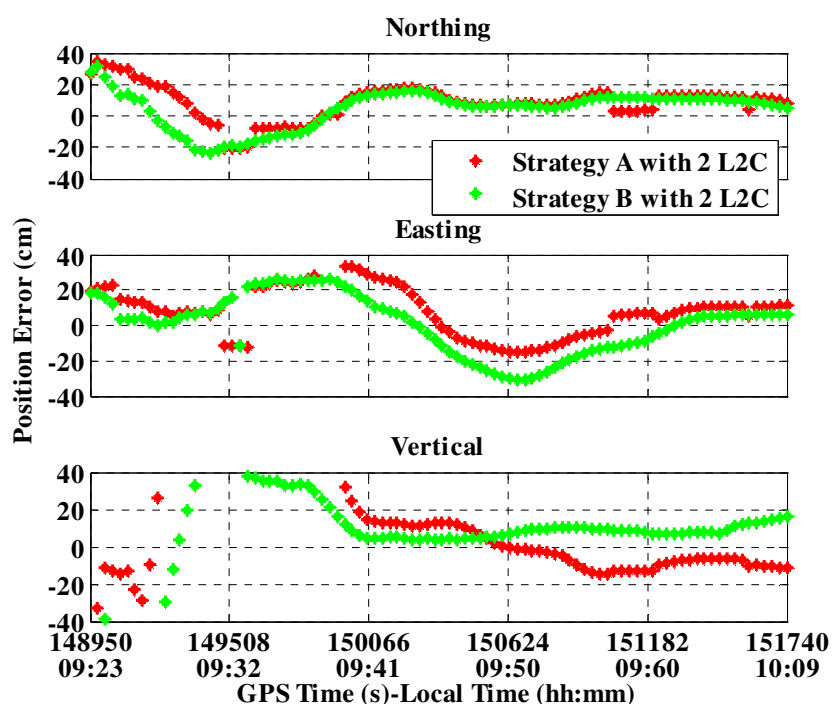


Figure 5.24: Position errors and number of fixed ambiguities, Strategy A and B with 2 L2C satellites (PRN 29 & 5) available, long baseline

Table 5.14 shows the corresponding statistics for the position errors and the AR performance. Comparing to the L1 Only Strategy, Strategy A provided lower PIF. In addition, the statistics also shows that Strategy A with 2 L2C satellites also tended to provide lower PIF than Strategy A itself with only 1 L2C satellite. The advantage of reducing PIF still holds for Strategy B. Note that for the case with PRN 12 and PRN 29

or PRN 12 and PRN 5, Strategy B still provided better vertical accuracy than Strategy A while the PIF for these two strategies are the same and the PCF of Strategy B is equal or lower than Strategy A. This observation indicates that the remaining ionospheric residual is effectively estimated by the single differential ZID state with certain accuracy.

Table 5.14: The whole dataset position error RMS and AR performance with 2 L2C satellites available, long baseline

PRN	Strategies	Position Error RMS (cm)			Ambiguity Fixing	
		<i>Northing</i>	<i>Easting</i>	<i>Vertical</i>	<i>PCF</i>	<i>PIF</i>
12&29	<i>Strategy A</i>	11	16	35	24.5%	2.1%
	<i>Strategy B</i>	11	15	31	16.0%	2.1%
12&05	<i>Strategy A</i>	11	25	49	21.3%	9.6%
	<i>Strategy B</i>	12	27	33	21.3%	9.6%
05&29	<i>Strategy A</i>	14	22	50	7.5%	7.5%
	<i>Strategy B</i>	13	16	29	0.0%	1.1%

As shown in Table 5.15, no ambiguity can be fixed during those short data batches for the long baseline. As a result, the MTFP performance can not be determined. For the relative longer data batches of 9 minutes processing, Strategy B still tended to reduce the PIF as compared to Strategy A, but it provided a higher PIF A for the 5 minutes data batches.

Table 5.15: Data batches AR performance with 2 L2C satellites (PRN 29 & 05) available, long baseline

PRN	Strategies	Span (minutes)	PCF	PIF	MTFF (s)
29 & 05	<i>Strategy A</i>	5	0.0%	11.1%	N/A
		9	0.0%	40.0%	N/A
	<i>Strategy B</i>	5	0.0%	22.2%	N/A
		9	0.0%	20.0%	N/A

In summary, with 2 available L2C satellites, Strategy A provided a lower PIF than itself with only 1 L2C satellite, and Strategy B still tended to provide lower PIF than Strategy A as the same conclusion obtained from the comparison between Strategy B and Strategy A with only 1 available L2C satellite. Besides, the MTFE improvement for AR is proved in this scenario with one L2C DD ambiguity added from 2 available L2C satellites as compared to the scenario with only 1.

Scenario with three L2C Satellites

In this scenario, the single differential ZID state is estimated by the dual-frequency measurements from three L2C satellites using Strategy B. Table 5.16 shows the position errors and AR performance for Strategy A and Strategy B for the short baseline. Again, Strategy B works similarly as Strategy A since the remaining ionospheric residual is negligible. Besides, the scenario with 3 L2C satellites does not bring improvement over the L1 Only scenario and the scenarios with one or two L2C satellites, quite similar performance has been observed among all these scenarios for the short baseline.

Table 5.16: The whole dataset position error RMS and AR performance with 3 L2C satellites available, short baseline

Strategies	Position Error RMS (cm)			Ambiguity Fixing	
	<i>Northing</i>	<i>Easting</i>	<i>Vertical</i>	<i>PCF</i>	<i>PIF</i>
<i>Strategy A</i>	7	11	24	72.3%	0.0%
<i>Strategy B</i>	6	10	25	72.3%	0.0%

Table 5.17 summarizes the AR performance for the data batches processing. Clearly, Strategy B is not necessary to obtain better performance for the short baseline and Strategy A presents satisfactory results especially with the MTFF improvement over the L1 Only Strategy and itself with one or two L2C satellites, though the time resolution is limited by the 30 seconds observation interval. Strategy A with three L2C satellites provides lower PIF and equal or higher PCF than the other strategies with one or two L2C satellites or the L1 Only Strategy. At this point, generally, AR performance improvement can be achieved by introducing additional one-by-one L2C satellite in each scenario as compared to the performance obtained from the L1 Only Strategy. The more the L2C satellite added in, the better AR performance is expected.

Table 5.17: Data batches AR performance with 3 L2C satellites available, short baseline

Strategies	Span (minutes)	PCF	PIF	MTFF (s)
<i>Strategy A</i>	5	33.3%	11.1%	150
	9	60.0%	0.0%	150
<i>Strategy B</i>	5	33.3%	11.1%	150
	9	40.0%	20.0%	180

Figure 5.25 shows the ambiguity validation test results for the long baseline case. The bootstrapping SR test shows that Strategy A with three available L2C satellites passes the threshold at the time point of 149100 that is the same as Strategy A with full availability of L2P measurements, while Strategy A with one or two L2C satellites could only pass the threshold at the time point of one epoch later. It may come to the observation that the

decorrelated widelane ambiguity formed by the L1 C/A DD ambiguities and the two additional L2C DD ambiguities achieves the accuracy of that formed by the L1 C/A DD ambiguities and the full availability of the L2P DD ambiguities. However, one additional L2C DD ambiguity formed from two available L2C satellites can not make equivalent decorrelated widelane ambiguity accuracy. For the ratio test, there is only one epoch for Strategy A to pass the threshold before the sufficiently converged float solution, much less than the L1 Only Strategy and Strategy A with one or two available L2C satellites. As such, there is large possibility to reduce the PIF for the entire data processing. Note that Strategy B passes the threshold at a later time point than Strategy A for the first time. It is due to the position float solution converges a little slowly for Strategy B to estimate one more state compared to Strategy A. This slower float solution convergence can be observed from the easting component shown in Figure 5.26. However, the vertical component of Strategy B converges faster and has better accuracy than Strategy A, since the ionospheric residual is effectively estimated by Strategy B, which has the most impact on the vertical accuracy estimation for removing a residual bias in the observation model. With a better float solution, Strategy B provides a 20 cm vertical accuracy improvement over Strategy A during the entire data processing other than relying on providing lower PIF, as shown in Table 5.18. Another important observation is that Strategy A and B with three available L2C satellites tend to provide the lowest PIF among all the strategies with L2C satellite and the L1 Only Strategy, however the PCF is not improved indicated by the statistics.

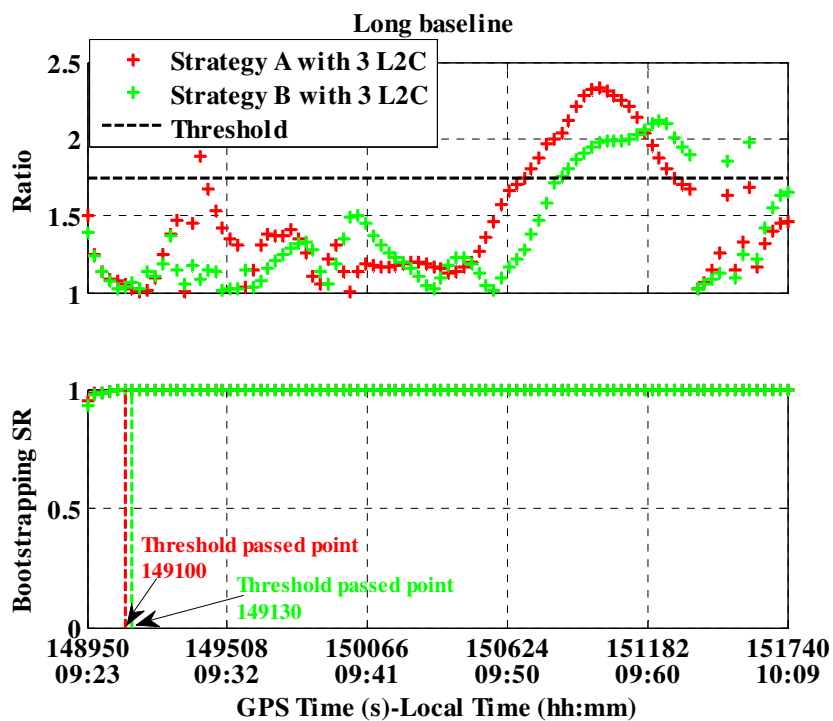


Figure 5.25: Ambiguity validation test values for Strategy A and Strategy B with 3 L2C satellites available, long baseline

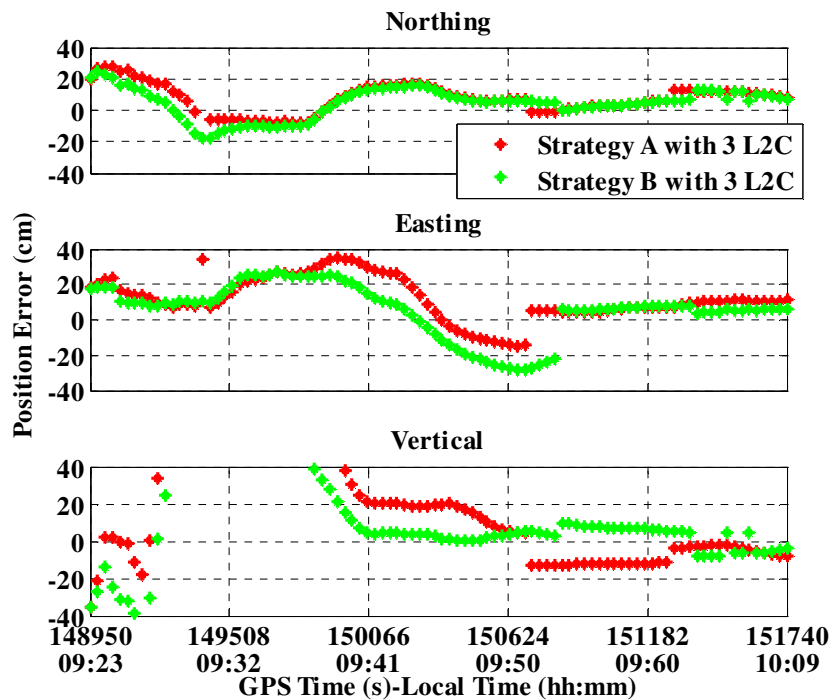


Figure 5.26: Position errors, Strategy A and B with 3 L2C satellites available, long baseline

Table 5.18: The whole dataset position error RMS and AR performance with three L2C satellites available, long baseline

Strategies	Position Error RMS (cm)			Ambiguity Fixing	
	<i>Northing</i>	<i>Easting</i>	<i>Vertical</i>	<i>PCF</i>	<i>PIF</i>
<i>Strategy A</i>	13	17	50	20.2%	1.1%
<i>Strategy B</i>	11	16	30	21.3%	0.0%

Finally, Table 5.19 shows the statistics for the AR performance of the data batches processing. Unfortunately, still no ambiguity can be fixed during all the short time period data batches. Both strategies with two or three L2C satellites have similar AR performance in terms of PIF, and provide better PIF than the L1 Only Strategy.

Table 5.19: Data batches AR performance with three L2C satellites available, long baseline

Strategies	Span (minutes)	PCF	PIF	MTFF (s)
<i>Strategy A</i>	5	0.0%	22.2%	N/A
	9	0.0%	40.0%	N/A
<i>Strategy B</i>	5	0.0%	22.2%	N/A
	9	0.0%	20.0%	N/A

In summary, having investigated the scenario with three available L2C satellites and previous scenarios with one or two L2C satellites, it is observed that Strategy A with three L2C satellites lowers the PIF compared to itself with one or two L2C satellites for the entire data processing, and improves the MTFF for the data batches processing in the short baseline case without the need to estimate the remaining ionospheric residuals.

Moreover, Strategy B improves the position solution and lowers the PIF than Strategy A in the long baseline case by estimating the remaining ionospheric residual through a single differential ZID state.

5.4 Summary

The work in this chapter evaluated the L1 and L2 dual-frequency relative precise positioning performance using the partial availability of L2C signals for a short baseline (31 km) and a long baseline (125 km) case. During the limited time period of 45 minutes data sets, there are 3 L2C satellites available and usable. Scenarios are divided by adding one, two, or three L2C measurements to do dual-frequency AR, positioning, and ionospheric residual estimation, comparing to the scenario with L1 measurements only or L1 and L2P measurements. A general conclusion is drawn that the more L2C measurements, the better performance of position accuracy and AR. For the short baseline, Strategy A lowers the PIF for the entire data processing and improves the MTFE for the data batches processing as one and one L2C satellite added in without the need to estimate the ionospheric residual, while Strategy B improves the position accuracy by providing better float solution and lowering down the PIF through estimating the ionospheric residual in the proposed single differential ZID method for the entire data set processing in the long baseline case.

CHAPTER 6: CONCLUSIONS AND RECOMMENDATIONS

The low-cost civil receivers will benefit from the modern L2C signals. It is interesting to find what performance can be achieved during the phase in of the L2C signals. The research of this thesis targets to investigate the feasibility of introducing the partial constellation of L2C signals as the second frequency signals for dual-frequency applications and to evaluate the corresponding positioning and AR performance as compared to the L1 single-frequency case and dual-frequency case with the full constellation of the L2P signals. The utilization of the partial constellation of the L2C signals is divided into a L1 C/A single-point positioning scenario and a DGPS L1 and L2 dual-frequency precise positioning scenario.

For the single-point scenario, an ionospheric error estimation approach is proposed to estimate a ZID using the L1 C/A and L2C dual-frequency code and phase measurements obtained from the modernized partial constellation of L2C satellites. Then the ZID is mapped down to obtain SID to provide ionospheric corrections for those satellites with only L1 C/A signal accessible by the low-cost civil receivers. In order to overcome the inherent limitations of the ionospheric group delay and phase advance, a batch and a sequential smoothing approach is adopted to improve the ionospheric error estimate for the post-processing mission and the real-time application respectively. Besides, a receiver IFB estimate can be obtained from the post-processing mission for the first data set, which is then used to correct the dual-frequency measurements for real-time application.

Finally, the derived ionospheric correction estimate is applied to the L1 C/A code measurements to evaluate the single-point positioning performance.

For the DGPS L1 and L2 dual-frequency precise positioning scenario, a 31 km short baseline and a 125 km long baseline are used. The dual-frequency AR performance and the corresponding positioning accuracy are evaluated for the two baselines with or without estimating the differenced ionospheric residuals. With the partial constellation of the L2C signals, limited number of one, two, or three L2C measurements is incorporated with the full constellation of the L1 C/A measurements for dual-frequency AR and positioning. Comparison has been made among the capability of with one, two, or three available L2C measurements.

To sum up, the following conclusions can be drawn based on the work described above:

- a) For the single-point positioning scenario, an IFB estimate is obtained for each of the three L2C satellites in estimating the ZID through batch processing, which is used to correct the SID of each L2C satellite. The resulted SID is then mapped to obtain the ZID for this satellite. The estimated ZID of each L2C satellite is found to be quite close to the values obtained from the broadcast Klobuchar model and the IONEX map.
- b) The measurements quality differs among different L2C satellites. The receiver IFB calculated by the measurements from PRN 15 differs relative large from the other two L2C satellites. The single-point position accuracy is poorer if the ionospheric correction is obtained by involving the PRN 15 measurements only

than the other cases, better position solution is achievable if the ionospheric corrections are obtained by involving another L2C satellite and PRN 15. It is suggested to estimate the receiver IFB and the ionospheric correction using at least two L2C satellites.

- c) Generally, a ZID can be estimated using dual-frequency measurements from one, two, or three L2C satellites and this delay can be used to generate SID to correct the L1 C/A pseudoranges for a better single-point position solution that has the same level of accuracy as obtained by using the broadcast Klobuchar ionosphere model.
- d) For the DGPS dual-frequency precise positioning scenario, a general conclusion is drawn that the more L2C measurements, the better performance of position accuracy and AR.
- e) For the short baseline, Strategy A lowers the PIF for the entire data processing and improves the MTFF for the data batches processing as one and one L2C satellite added in without the need to estimate the ionospheric residual. Strategy B improves the position accuracy by providing better float solution and lowering down the PIF through estimating the ionospheric residual to some extent using the proposed single differential ZID method for the long baseline for the entire data set processing.
- f) Although the data sets used in this research are not subjected to severe ionospheric error, the proposed ionospheric error estimation methods, both the single-point ZID and the differential ZID methods, are experimentally proved to be feasible and effective.

Having obtained the above conclusions and with the limitations of this research in mind, the following recommendations are made:

- a) Due to the fact that the L2C measurement is available in geodetic grade receivers in most cases, the results obtained may be optimistic for the targeted low-cost civil receivers. The work in Chapter 5 subjects to this limitation as the measurements from the expensive Trimble NetRS receiver are used for performance evaluation. Future work is needed to assess the performance using the L2C measurements from “real” low-cost receivers.
- b) The time resolution is limited by the observation interval of 30 seconds for time sensitive performance evaluation as the case the MTFF evaluation for data batches processing in Chapter 5. Other data sets with different observation rate are also of interest for performance evaluation.
- c) In order to have up to three L2C satellites available and useable for performance evaluation and comparison among cases with different number of L2C satellite involved, the time duration of the data sets used in Chapter 4 and Chapter 5 are limited by the short availability of the simultaneously three L2C satellites. As the gradual deployment of the L2C satellites, there will be longer time period of data sets for processing and the benefit of the longer data set is also of interest in the future work.
- d) An isotropic assumption is used here for the ionosphere shell, more complex algorithm is of interest to be developed without the limitation by this assumption.

- e) The civilian users can benefit from the partial availability of the L2C signals and are recommended to utilize these limited number of L2C measurements during its deployment phase.

REFERENCES

- al-Fanek, O., S. Skone, and G. Lachapelle (2007) "Evaluation of L2C Observations and Limitations," presented at the *ION GNSS 2007*, Session F5, Fort Worth, Texas, September 25-28
- Blewitt, G. (1989) "Carrier phase ambiguity resolution for the GPS applied to geodetic baselines up to 2000 km," *Journal of Geophysical Research*, Vol.94, No.B8, pp.10187-10203
- Department of Defense (2008) *Global Positioning System Standard Positioning Service Performance Standard*, Fourth Edition, September, U.S.
- Fontana, R.D., W. Cheung, and T. Stansell (2001) "The Modernized L2 Civil Signal: Leaping Forward in the 21st Century," *GPS World*, September
- Gao, Y., P. Heroux, and J. Kouba (1994) "Estimation of GPS receiver and satellite L1/L2 signal delay biases using data from CACS, " in *Proceedings of International Symposium on Kinematic Systems in Geodesy, Geomatics and Navigation*, Banff, Alberta, Canada, 20 August – 2 September, pp. 109-116
- Gelb, A. (1974) *Applied Optimal Estimation*, The M.I.T. Press.
- Grewal, M.S. and A.P. Andrews (2001) *Kalman Filtering: Theory and Practice Using MATLAB*, Second Edition, John Wiley & Sons, Inc.
- Hatch, R. (1982) "The Synergism of GPS Code and Carrier Measurements," *Proceedings of the Third Geodetic Symposium on Satellite Doppler Positioning*, DMA, Las Cruces, New Mexico, pp. 1213-1232

Hong, C.K. (2007) *Efficient Differential Code Bias and Ionosphere Modelling and their Impact on the Network-based GPS Positioning*, Ph.D. dissertation, Geodetic Science and Surveying, The Ohio State University, Columbus, OH

Hopfield, H.S. (1970) Tropospheric Effect on Electromagnetically Measured Range: Prediction from Surface Weather Data, Applied Physics Laboratory, John Hopkins University, Baltimore, MD, USA

IS-GPS-200D (2006) Navstar Global Positioning System: Interface Specification IS-GPS-200 Revision D, Interface Revision Notice (IRN)-200D-001, 7 March, Navstar GPS Space Segment/Navigation User Interfaces

Kay, S.M. (1993) *Fundamentals of Statistical Signal Processing, Volume I: Estimation Theory*, Prentice Hall

Klobuchar, J.A. (1987) Ionospheric Time-Delay Algorithm for Single-frequency GPS Users, *IEEE Transactions on Aerospace and Electronics Systems*, Vol. AES-23, No. 3, 325-331

Klobuchar, John A. (1996) Ionospheric Effects on GPS, in *Global Positioning System: Theory and Applications, Vol. II*, B. Parkinson, J. Spilker, P. Axelrad, and P. Enge (Eds.), American Institute of Aeronautics and Astronautics, pp. 485-515

Krakiwsky, E.J. (1990) *The Method of Least Squares: A Synthesis of Advances*, Department of Surveying Engineering, The University of Calgary, Calgary, AB, Canada, T2N 1N4

- Lachapelle, G. (2008) *Advanced GNSS Theory and Applications*, ENGO625 Lecture Notes, Department of Geomatics Engineering, University of Calgary, Canada
- Lachapelle, G., J. Hagglund, W. Falkenberg, P. Bellemare, M. Casey, and M. Eaton (1986) "GPS land kinematic positioning experiments," Proceedings of the 4th International Geodetic Symposium on Satellite Positioning, 2, 1327-1344, Austin, TX, USA, Apr. 28 – May 2
- Leandro, R., M. Santos, and R.B. Langley (2006) "UNB Neutral Atmosphere Models: Development and Performance," in Proceedings of Institute of Navigation National Technical Meeting (ION NTM 2006), Monterey, CA, 12-20 January, pp. 564-573
- Liu, J., M.E. Cannon, P. Alves, M. Petovello, G. Lachapelle, G. MacGougan, and L. de Groot (2003) "A Performance Comparison of Single and Dual Frequency GPS Ambiguity Resolution Strategies," *GPS Solutions*, 7: 87-100
- Liu, J. (2002) Implementation and Analysis of GPS Ambiguity Resolution Strategies in Single and Multiple Reference Station Scenarios, UCGE Reports No. 20168, Department of Geomatics Engineering, The University of Calgary, Calgary, AB
- Liu, X.L., C. Tiberius, and K. de Jong (2004) "Modelling of differential single difference receiver clock bias for precise positioning," *GPS Solutions*, vol. 7, January, pp. 209-211
- Liu, Z.Z., Y. Gao, and S. Skone (2005) "A study of smoothed TEC precision inferred from GPS measurements," *Earth Planets Space*, 57, 999-1007

- Macgougan, G. (2009) *Real-Time Kinematic Surveying using Tightly-Coupled GPS and Ultra-Wideband Ranging*, Ph.D. Thesis, UCGE Reports 20293, Department of Geomatics Engineering, The University of Calgary, Calgary, AB, Canada
- Misra, P. and P. Enge (2001) *Global Positioning System: Signals, Measurements, Performance*, Ganga-Jamuna Press, Lincoln, Massachusetts, USA
- NRCan (2010) *Western Canada Deformation Array station map*, <http://gsc.nrcan.gc.ca/geodyn/wcda/images/wcdastationmap.jpg>, last accessed in August 25, 2010
- Odijk, D. (2002) *Fast Precise GPS Positioning in the Presence of Ionospheric Delays*, Ph.D. dissertation, Mathematical Geodesy and Positioning, Faculty of Civil Engineering and Geosciences, Delft University of Technology, Thijsseweg 11, 2629 JA Delft, The Netherlands
- Odijk, D. (2000) "Weighting Ionospheric Corrections to Improve Fast GPS Positioning Over Medium Distances," in *Proceedings of ION GPS 2000*, Salt Lake City, UT
- Petovello, M., C. O'Driscoll, G. Lachapelle, D. Borio, and H. Murtaza (2008) "Architecture and Benefits of an Advanced GNSS Software Receiver," *Journal of Global Positioning System* 7(2): 156-168.
- Schaer, S. (1999) *Mapping and Predicting the Earth's Ionosphere Using the Global Positioning System*, PhD dissertation, Astronomy Institute of University Bern, Bern, Germany
- Simsky, A., J.-M. Sleewaegen, and P. Nemry (2006) "Early Performance results for new Galileo and GPS signals-in-space," *ENC GNSS 2006*, Manchester, UK, 7-10 May

- Skone, S. (1998) *Wide Area Ionosphere Grid Modelling in the Auroral Region*, Ph.D. thesis, Department of Geomatics Engineering, The University of Calgary, Calgary, AB, Canada
- Sukeova, L., M. C. Santos, R. B. Langley, R. F. Leandro, O. Nnani, and F. Nievinski (2007) "GPS L2C Signal Quality Analysis," *ION 63rd Annual Meeting*, April 23-25, Cambridge, MA, USA
- Teunissen, P.J.G, P. Joosten, and C.C.J.M. Tiberius (2002) "A Comparison of TCAR, CIR and LAMBDA GNSS Ambiguity Resolution", in *Proceedings of ION GPS 2002*, 24-27 September, Portland, OR, pp. 2799-2808
- Teunissen, P.J.G. and S. Verhagen (2008) "GNSS ambiguity resolution:when and how to fix or not to fix?" in *Proceedings of the International Association of Geodesy Symposia*, vol. 132, pp. 143-148
- Teunissen, P.J.G. (2003a) "Integer aperture GNSS ambiguity resolution," *Artificial Satellites*, Vol. 38, No. 3, pp. 79-88
- Teunissen, P.J.G. (2003b) "Towards a unified theory of GNSS ambiguity resolution," *Journal of Global Positioning Systems*, Vol. 2, No. 1, pp. 1-12
- Teunissen, P.J.G. (1999) "An optimality property of the integer least-squares estimator," *Journal of Geodesy*, 73: 587-593
- Teunissen, P.J.G. (1997) "The geometry-free GPS ambiguity search space with a weighted ionosphere," *Journal of Geodesy*, vol. 71, No. 6, pp. 370-383

- Teunissen, P.J.G. (1994) "A new method for fast carrier phase ambiguity estimation," *Proceedings of IEEE Position, Location and Navigation Symposium PLANS'94*, Las Vegas, NV, April 11-15, pp. 562-573
- Teunissen, P.J.G. (1995) "The least-square ambiguity Decorrelation adjustment: a method for fast GPS integer ambiguity estimation", *Journal of Geodesy*, Vol. 70, No. 1-2, November, pp. 65-82
- Trimble (2005) *Trimble NetRS GPS Reference Station*, http://www.trimble.com/infrastructure/pdf/NetRS_datasheet.pdf, last accessed 11 August, 2010
- Verhagen, S. (2006) "Improved Performance of Multi-carrier Ambiguity Resolution Based on The LAMBDA Method," in *Proceedings of the 3rd ESA Workshop on Satellite Navigation User Equipment Technologies*, Noordwijk, The Netherlands, 11-13 December, 8 pages
- Verhagen, S. (2004a) *The GNSS integer ambiguities: estimation and validation*, Ph.D. Dissertation, Delft Institute of Earth Observations and Space Systems, Delft University of Technology
- Verhagen, S. (2004b) "Integer ambiguity validation: an open problem," *GPS Solutions*, vol. 8, No. 1, pp. 36-43
- Woo, K.T. (1999) "Optimum Semicodeless Carrier Phase Tracking of L2," presented at the *12th International Technical Meeting of the Satellite Division of the Institute of Navigation*, Nashville, Tennessee, September 14-17

Zhang, J. (1999) *Investigations into the Estimation of Residual Tropospheric Delays in a GPS Network*, MSc Thesis, Geomatics Engineering, The University of Calgary, Canada